An Experimental Study of Multiple Continua in Small Molecules

An Experimental Study of Multiple Continua in Small Molecules

Een wetenschappelijke proeve op het gebied van
de natuurwetenschappen, wiskunde en informatica

ACADEMISCH PROEFSCHRIFT

ter verkrijging van de graad van doctor
aan de Katholieke Universiteit Nijmegen
op gezag van de Rector Magnificus Prof. dr. C.W.P.M. Blom,
volgens besluit van het College van Decanen
in het openbaar te verdedigen maandag 15 december 2003
des namiddags om 13:30 uur

door

LAURA CIUBOTARIU-DINU

geboren op 25 februari 1974
te Suceava, Roemenië

Promotor: Prof. Dr. W.J. van der Zande

The experiments described in this thesis were performed at:

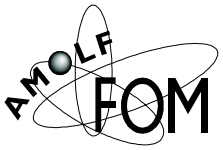

FOM Institute for Atomic and Molecular Physics
Kruislaan 407
1098 SJ, Amsterdam, The Netherlands

This work is part of the research program of the Stichting voor Fundamenteel Onderzoek der Materie (Foundation for Fundamental Research on Matter) and was made possible by financial support from the Nederlandse Organisatie voor Wetenschappelijk Onderzoek (Netherlands Organization for the Advancement of Research). This research is part of the FOM-Programme Molecular Atmospheric Processes (MAP).

Mariei si parintilor mei
für Andreas

This thesis is based on the following publications:

Chapter 1 — *Fast beam and ion imaging techniques for molecular dynamics*
L. Dinu and W. J. van der Zande
(in preparation as review for J. Phys. Chem. A)

Chapter 2 — *Application of a novel time-resolved event counting technique in velocity map imaging*
L. Dinu, A. T. J. B. Eppink, F. Rosca-Pruna, H. L. Offerhaus, W. J. van der Zande and M. J. J. Vrakking
Rev. Sci. Instr. 73 (12): 4206-4213 December 2002

Chapter 3 — *Photodestruction of NO_2^- using time resolved multicoincidence detection photofragment spectroscopy*
L. Dinu and W. J. van der Zande
(submitted to Chem. Phys.)

Chapter 4 — *Predissociation versus autoionization for high Rydberg states of H_2*
L. Dinu, Y.J. Picard and W.J. van der Zande,
in *Dissociative Recombination of Molecular Ions with Electrons*, ed. S. L. Guberman (Kluwer Academic/Plenum Publishers, New York), 2003, pp. 301-308

Competition between predissociation and autoionization in high Rydberg states on H_2
L. Dinu, Y. J. Picard and W.J. van der Zande
(submitted to J. Chem. Phys.)

Chapter 5 — *Competition between photodetachment and photodissociation in O_2^-*
L. Dinu, G. C. Groenenboom and W. J. van der Zande
J. Chem. Phys. 08 November 2003

Contents

Preface

The beauty of gas-phase molecular research lies in the ability to provide direct insight into the material world, providing knowledge on the fundamental aspects of matter. Experiments on isolated molecules are powerful tools for investigating the processes that govern the kinematics of simple molecular systems. The simpler the system is, the greater is the insight into its nature that can be achieved. Apart from the intrinsic fundamental importance, gas-phase molecular studies are relevant to atmospheric science. The knowledge obtained in laboratories, i.e., cross sections of reactions, rates of different processes, transition spectra of different species, presents input parameters for modeling of atmospheric processes.

At the border between chemistry and physics, atomic and molecular science received a lot of attention since the beginning of the last century. In 1926, based on the original Bohr theory, Erwin Schrödinger completed a comprehensive theoretical description of the electronic structures of atoms. Schrödinger's ideas are covered in the *Modern Theory of Atomic Structure*. Shortly after, Max Born and Robert Oppenheimer developed a model for the diatomic molecule, based on the almost stationary motion of the nuclei with respect to the fast motion of the surrounding electrons. The breakdown of the Born-Oppenheimer approximation, seen as perturbations, has been extensively studied and more complex models of diatomic interactions have been developed. In parallel with the theoretical development, experimentalists have been also studying molecular spectra. In 1939 Gerhard Herzberg gathered in his book *Molecular Spectra and Molecular Structure I. Spectra of Diatomic Molecules* all of the theoretical and experimental work from the first three decades of molecular structure studies. This book laid the foundations for all work that has since been done in the study of diatomic molecules. The Schrödinger equation and quantum mechanics impose a special non-classical structure of quantized energy levels, beautifully displayed in highly structured lines in emission and absorption. These lines, their position as well as their intensity, have been the most important means to determine the molecular structure. When exciting molecules to energies where dissociation and/or ionization occur, the final continuum states loose their quantization and we speak about multiple continua. Here different observables are needed to unravel these dynamic processes, whose nature is so different.

The complexity of molecular systems is nicely illustrated by the fact that even after many decades of work, many new questions have been raised and many old questions have still to be answered, including those referring to the simplest molecular system, the hydrogen molecule. With the work presented here we contribute a small step towards the goal of a complete and detailed understanding of the structure and dynamics of molecular hydrogen. We have studied the behavior of high lying Rydberg states of molecular hydrogen, providing branching ratios for different decay limits, as well as new spectroscopic information on the $v = 0$, $n = 12 - 18$ states. We have also observed unusual behavior of the dissociation strengths for the different Rydberg states, the nature and cause of which still remains unknown.

Unlike neutral molecules which have been studied in great detail, both theoretically and experimentally, negative molecular ions haven't received as much attention. Photodetachment is the most studied reaction, but there are very few studies on the photodissociation of molecular ions such as O_2^- or NO_2^-. In the experiments presented here, the O_2^- molecules are subject to UV photon excitation. Photodetachment and photodissociation are the decay channels for the excited O_2^- molecules. Our measurements provide branching ratios between these two decay limits and details of the transition from the molecular state to two separate atoms during the dissociation process are obtained by identifying the intermediate state involved in the dissociation process and by resolving the atomic fine structure of the dissociation limit. The study of NO_2^- is a challenge, also from an experimental point of view since this molecule is a more complex system. The analysis of the photodissociation of triatomic molecules requires a different approach than for the homonuclear diatomic molecules. The detection of charged fragments in a fast beam apparatus requires special attention. The kinetic energy release spectrum is less relevant mainly due to the fact that the molecular NO fragment stores part of the kinetic energy release from the dissociation internally, as rotational and vibrational energy. The decay study of the excited NO_2^- states provides the branching ratio for competition between the photodissociation and photodetachment processes.

In parallel with the work presented here, we have improved the experimental techniques necessary to obtain more insight into these processes, achieved by selectively choosing the initial states, and by the detection of the complete set of reaction products. The main part of the experiment comprises a fast beam apparatus, adapted for pulsed laser excitation, in combination with a three-dimensional multi-particle detector. The aim was to develop a time- and position-sensitive detector that allows coincidence detection of multiple fragments with no dead time and good time- and position resolution. To achieve this, two systems have been developed. The first system uses combination of a fast and sensitive CCD camera for position measurement and a 16-strip photomultiplier tube for the time measurement. The second detection system is a double exposure CCD camera, representing an elegant detection solution that combines in one device the time and position detection. This detector also provides an increased detection efficiency and multiparticle abilities.

Chapter 1

Instrumental Overview

This chapter provides an overview of experimental techniques which were developed to obtain direct insight into dynamical processes in atoms and molecules. Some of these methods are known under the collective name of 'IMAGING' techniques. We describe the different apparatus- and detector-technologies that are related to the different IMAGING techniques. Both so-called "fast beam" and "ion imaging" techniques are described and compared. The detector technologies vary from position and time decoding systems to advanced uses of multi-particle detection. The two detection systems used in the experiments presented in this thesis are discussed.

1.1 Introduction

The study of the reaction dynamics involving atoms and molecules in the gas-phase has witnessed great progress over the last few decades. The driving forces behind this progress has been the development of new techniques, powerful lasers, and fast time- and position-sensitive particle detectors. The central idea in many of these experiments is to retrieve as much information as possible on the reaction, starting with a full characterization of the initial state (for example, by selectively preparing the initial internal state), the measurement of the total cross section of the reaction, and finishing with a complete description of the asymptotic properties of the reaction by characterizing the branching ratios between different decay limits and the product fragments, for example, with their velocity distribution and angular distribution. The amount of information that can be retrieved depends on the type of the reaction and the technique used to investigate it. At the present time, there is no universal technique suitable for all two- or three-body reaction studies. Depending on the process, as well as on the nature of reaction products (e.g., electrons, neutrals or ions) different techniques and detection schemes are used.

In the case of an n-body reaction, the system has $6n$ degrees of freedom. Taking into account the conservation laws of momentum and energy, the degrees of freedom are decreased to $6n-4$. Often the measurement of the position coordinates of the particles on the detector (x, y) cover $2n$ degrees of freedom, while other n degrees of freedom are obtained by the measurement of the arrival time of the particles at the detector. In many cases, the experiment itself and the symmetry of the molecular system reduce the number of variables necessary to be measured for a complete kinematic description. A very favorable case is, for example, the photodissociation of a homonuclear diatomic molecule. By fixing in space the reaction point (at the crossing of a narrow molecular beam with a focused laser beam) and by defining the moment when the reaction takes place (in experiments involving short pulsed lasers) the (x, y, t) detection of only one of the two identical fragments is sufficient to reconstruct the full kinematics of the dissociation and to retrieve the kinetic energy release (KER). From this, the bonding energy of the excited state and the angular orientation of the molecule during the reaction can be calculated. In principle, by only counting the fragments, one can measure the absolute cross section of a reaction [1,2]. By only detecting the time-of-flight TOF of one fragment (so-called one-dimensional detection), by means of momentum and energy conservation, the kinetic energy release can be determined. If the symmetry of the reaction permits, one can measure only the coordinates of the fragments on the detector (x, y) (two-dimensional detection) and by means of mathematical inversion procedures the three dimensional image of the reaction can be reconstructed.

For more complicated processes, for example in the case of a three-body breakup reaction, it is necessary to detect in coincidence the position coordinates and the arrival time on the detector of all fragments (three-dimensional detection).

In general, a 1D detection scheme usually refers to a time-of-flight (TOF) measurement, a 2D detection scheme to (x, y) position measurements, and a 3D detection scheme to (x, y, t) position and arrival time measurements. The detectors used for 2D and 3D are generically called *imaging* detectors. The 3D detectors are usually more complex than the 2D detectors, since they provide the extra information that makes possible a full kinematic description of a reaction.

During the last few decades, two techniques have been developed for the study of molecular processes: fast beam techniques and ion imaging techniques. The fast beam technique was introduced in 1982 by Los and coworkers [3, 4]. The molecular ions are produced in an ion source and extracted at a few keV. A continuous beam is formed and directed towards a detector. A mass filter selects the ions of interest which, in the first experiment, were H_2^+. The beam shape and trajectory are controlled by Einzel lenses and deflection plates. The ion beam is directed through a 1-mm length collision chamber in which charge exchange of H_2^+ under a collision with earth-alkali vapor takes place $H_2^+ + A \rightarrow H_2^* + A^+ \rightarrow H + H + (A^+) + KER$. A time and position-sensitive detector consisting of microchannelplates and two sets of semi-circular shaped anodes measures, in coincidence, the distances R_1 and R_2 between the position of the two H atoms and the center of the detector as well as the arrival time difference τ. This information is sufficient to completely determine the kinematics of the dissociation in the molecular centre-of-mass frame. High resolution in both position and timing is achieved i.e. a FWHM of 100 μm and 0.5 ns, respectively. Later, versatile and powerful pulsed lasers have been used to selectively prepare the internal state. The detection system has been developed further, such as to ultimately allow multiparticle $3D$ coincident detection with both good position- and time-resolution and no dead time.

The ion imaging technique was introduced by Chandler and Houston [5]. A molecular pulsed and skimmed beam is directed towards the imaging ion detector through a hole in the repeller plate. At 90°, a pulsed unfocused laser dissociates the molecule. Shortly thereafter (10 ns), the fragments are ionized via $2 + 1$ multiphoton ionization by a counter propagating focused laser beam. The state-selected ions are created in the electric field between the repeller plate and the ground grid, which is placed in front of the imaging detector. The positive ions are selectively detected according to their mass over charge ratio by using the TOF of these ions to the detector. The 2D detector consists of a combination of microchannel plates and a phosphor screen. The impact of each ion, transformed by the phosphor screen into a luminous flash, is recorded on Polaroid film.

1.2 Fast beam techniques

The fast beam techniques have been extensively applied in the study of many different reaction mechanisms, for example, dissociative charge exchange [3, 4], photodissocia-

tion [6–13], collision induced dissociation [14–16], dissociative photodetachment [17], photoionization [18], photodetachment [19–22], Coulomb explosion [23] and many others. The molecular ions are produced in a variety of different ion sources (e.g., electron-impact ion source, hollow cathode discharge ion source), and extracted at $1 - 10$ keV. The ion beam is either continuous or pulsed, depending on the specific experiment. After the mass selection of the ions, the beam is directed towards the detector. Different reactions can be induced by interaction with photons, electrons, ions or collision gases. The interaction region is often well defined in space, for example at the crossing between the molecular beam and the pulsed laser beam. The fragments resulting from the reaction are detected on a detector, which often is a time- and position-sensitive detector consisting of microchannel plates (MCPs) in combination with either phosphor screen or multi-anodes (e.g., resistive anodes, wedge-and-strip anodes, and delay-line anodes). Charge Coupled Devices (CCD) cameras are used to record the light coming from the phosphor screen and to retrieve the (x, y) coordinates of each particle, while the timing t is recorded with photomultiplier tubes. Recently, a double exposure camera has been developed which records not only the position but also the arrival time of the fragments. If multianode detectors are used, the (x, y, t) information is decoded by analyzing the charge distribution over the anodes.

Many of these experiments are performed in coincidence, i.e., all fragments from the reaction being detected. In Fig. 1.1 we present a schematic of a general fast beam experiment. Let us consider the photodissociation of a homonuclear diatomic molecule. The reaction originates at 'O'. Assuming an isotropic orientation of the molecules when breaking, the fragments move in all spatial directions with kinetic energies that depend on the energy of the initial internal state, the dissociation limit and the input energy (e.g., the photon energy). Although the KER values can reach a few eV, they are still small compared with the initial kinetic energy of the beam (few keV). Consequently, all the fragments reach the detector, including those ejected backwards with respect to the detector. We assume that dissociation is well characterized by only one KER value. During the time-of-flight the additional velocity of the fragments $\overrightarrow{v}_{diss.}$ distributes the particles on an expanding spherical surface. In Fig. 1.1 we represent two equivalent dissociation events, one corresponding to a molecule dissociating along the z axis (fragments a and b) and the other one corresponding to a molecule dissociating perpendicular to the z axis (fragments c and d). The fragments arrive on the detector in different places and at different times. Particles a and b arrive close together on the detector, but with a large time difference, such that the KER information is encoded mainly in the timing measurement. Particles c and d arrive with a large distance separation, but with a shorter time difference, such that the KER information is mainly encoded in their (x, y) positions. In a typical coincidence experiment, when the detector is suitable for two-particle detection, the events are recorded successively and no more than one per detection cycle [3, 4, 6, 7, 9, 10, 24]. More advanced detectors allow the detection of more events in the same frame [12, 17]. For a coincidence experiment, the maximum number of particles detected is limited

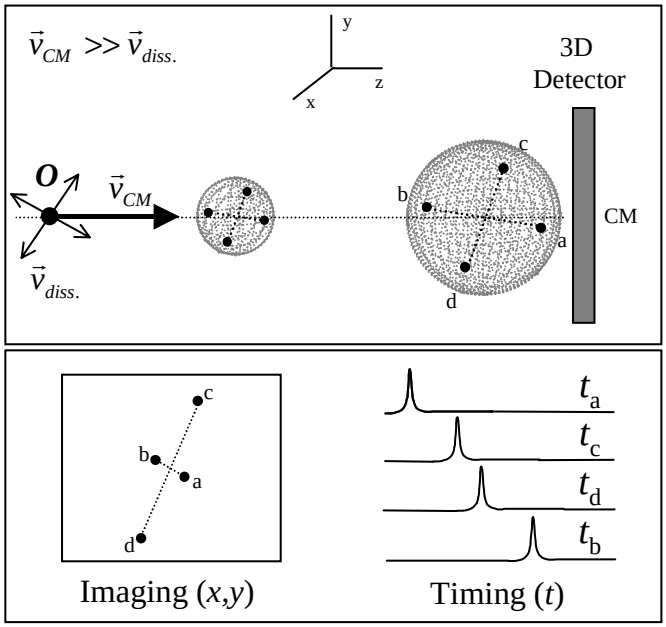

Figure 1.1: *A schematic for a fast beam experiment. The fragments resulting from a dissociation event travel towards the detector with the beam velocity* v_{CM}. *In addition, they receive a velocity component specific to the kinetic energy of the dissociation* v_{diss}. *As a result, the spatial distribution of the fragments while travelling is an expending spherical shell. Two dissociation events corresponding to the same kinetic energy release are depicted. Fragments* ***a*** *and* ***b*** *resulting from the dissociation of a molecule oriented almost perpendicular to the detector, arrive with a large time difference but a small position difference. The other pair of fragments (****c*** *and* ***d****) represent the dissociation of a molecule oriented parallel to the detector. The fragments arrive with a small time difference but with a large position difference.*

such that, for example, by centre-of-mass selection, they can be still correlated. A pair of particles are considered fragments of the same molecule if their centre-of-mass lie in the middle of the detector, in a region defined by the transversal size of the parent beam.

The kinetic energy release and the dissociation angle θ fully describe the kinematics of the dissociation of diatomics:

$$KER = \frac{E_0}{L^2}\frac{m_1 m_2}{(m_1+m_2)^2}(D^2 + v_0^2\Delta t^2)(1 + 2\frac{m_1 - m_2}{m_1 + m_2}\frac{v_0\Delta t}{L}), \tag{1.1}$$

$$\theta = arctg(\frac{D}{v_0\Delta t}), \tag{1.2}$$

$$\varphi = arctg(\frac{y_1 - y_2}{x_1 - x_2}). \tag{1.3}$$

where E_0 is the translational kinetic energy of the parent beam, v_0 is the translational velocity of the parent beam, $m_1$and m_2 are the two masses of the fragments, D is the distance between the fragments on the detector, $\Delta t = t_1 - t_2$ is the arrival time difference (has a sign) and L is the distance between the origin of the dissociation 'O' and the detector. For a homonuclear diatomic molecule, Eq. (1.1) reduces to:

$$KER = \frac{E_0}{4L^2}(D^2 + v_0^2\Delta t^2), \tag{1.4}$$

In these equations the coordinates of the fragments (x, y, t) do not appear explicitly. Once the fragments are detected in coincidence, it is sufficient to determine the distance between them, D, and the arrival time difference Δt. We would like to stress here that, in case of a coincidence experiment, it is not required to have a very small and well defined interaction region since the uncertainty in the (x, y) position of the molecule at the moment of dissociation is eliminated by measuring the distance between the fragments on the detector.

Of course, experiments have been performed on more complex molecules, with more complex multiparticle fragmentation pathways. An example is the study of triatomics. The earliest photodissociation studies of the H_3^+ molecule [8, 10] only investigated the two-body fragmentation. Although the three-body fragmentation was observed it was not fully characterized, mainly due to the fact that only two out of three fragments were detected. In their study, Müller et al. [10] measured the branching ratio between the two- and three-body fragmentation channels. After the development of time-and position-sensitive detectors which combine multihit

detection with a large detection area and a good position- and time-resolution, complete three-body breakup studies [12, 17] were possible. Gardner, Graff and Kohl discuss fast beam three-body dissociation experiments, and present the equations for determining the photofragment mass from the 2D projection of the fragment velocity vectors on the detector [25]. Continetti et al. have developed a photoelectron-multiple-photofragment coincident spectrometer, using a detection system based on the delay-lines approach [17]. This new multiparticle time- and position-sensitive detector has been used in a study of the laser-induced three-body fragmentation of O_6^-. Müller et al. have investigated the photodissociation of H_3^+ into three $H(1s)$ atoms by using a time- and position-sensitive detector which consists of two identical sets of microchannel plates and delay line anodes [12]. From the measurement of position and arrival time differences between the three fragments detected in coincidence, the three momentum vectors $(\mathbf{u}_1, \mathbf{u}_2, \mathbf{u}_3)$ in the centre-of-mass frame have been determined. The kinetic energy release of the dissociation has been calculated as sum of the three $m_i \mathbf{u}_i^2/2$ components. By plotting the correlation among the fragment momenta in a Dalitz representation [26], a non-homogeneous distribution of fragment momenta has been observed, showing preferred fragmentation geometries.

A more complex fast beam setup has been used for the study of collision induced dissociations on Na_n^+ clusters [14–16]. In this setup an electrostatic analyzer separates the neutral fragments from the ionic ones. Position-sensitive detectors based on three MCPs and delay line anodes record the position of the fragments, the TOF being measured by a multihit time digitizer.

A distinct class of fast beam experiments have been performed in heavy-ion storage rings (CRYRING - Sweden , TSR - Germany and ASTRID - Denmark). These facilities show, in many respects, similarities with fast beam setups described above (for example, the use of the same ion sources, the presence of a molecular ion beam, the reaction being induced in a field free region, similar detection systems, etc.). Contrary to standard fast beam machines, these large facilities (see Fig. 1.2) are built such that bunches of molecular ions, after injection, are circulated many times in the ring and accelerated until the ions reach MeV kinetic energies. After acceleration, the beam can be stored in the ring for many seconds. Molecules that have an intrinsic dipole moment can vibrationally relax during this storage time. The beam is phase space cooled by a merged electron beam in the electron cooler. In 1992 Datz and Larsson [27] suggested for the first time the use of storage rings for the study of molecular ions. Since then, the most extensively studied molecular reaction in storage rings has been dissociative recombination ($AB^+ + e^- \rightarrow A + B$) [28, 30–40]. For this particular process, the cooler also provides the electrons for the reaction. Due to the very high energies of the molecular beam, the relative kinetic energy of the electrons with respect to the ion beam is very well defined, allowing measurements of rate coefficients at precisely defined electron collision energies. As a drawback, the KER is measured with much lower resolution than in the keV fast beam experiments, mainly due to the fact that the interaction region with the electrons is rather long (85 cm

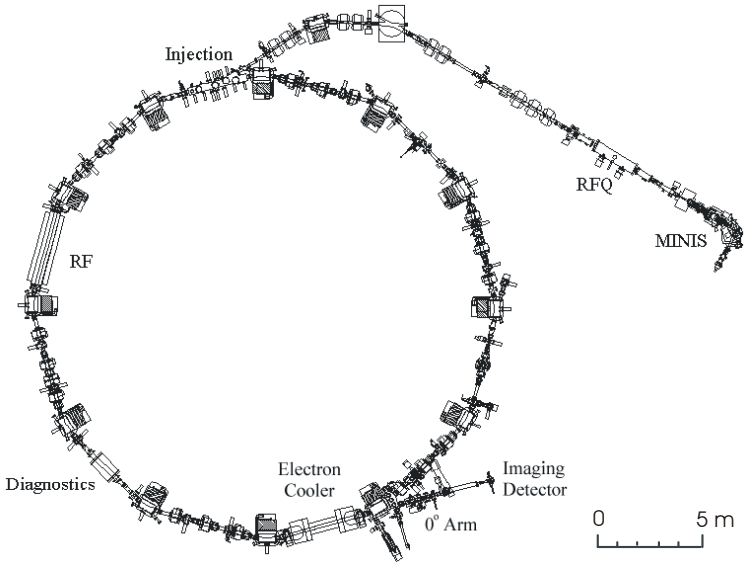

Figure 1.2: *Layout of the storage ring facility* CRYRING [37]

at CRYRING) compared with the distance to the detector L (5-6 m). Eq. (1.1) shows another consequence of the very fast beams. Since v_0 is large (up to $c/10$), the maximum time difference Δt becomes very small (~ 1 ns). The neutral fragments resulting from the DR reaction, escape the ring and reach an imaging detector placed 5-6 meters away in a continuation of the interaction region. Usually, a combination of microchannel plates with a phosphor screen is used for detecting all the fragments in coincidence. A CCD camera records the image of the phosphor. In addition, in some experiments, the arrival time difference of the fragments is also recorded (by multi-anode or multichannel photomultiplier tubes). This time information is often used only as a selection method together with centre-of-mass selection, to correlate fragments belonging to the same dissociation event. The position information is used to estimate the projected distance D between the fragments. From the D distribution, branching ratios between the different dissociation limits are determined [28, 32, 33]. From the shape of the distance distributions, angular information referring to the anisotropy of the dissociation process can be extracted [28].

Recently, more complex DR reactions leading to three-body breakup have been investigated in storage rings. Strasser et al. [39] studied the reaction $H_3^+ + e^- \rightarrow H(1s) + H(1s) + H(1s)$. Since the detector used was a 2D imaging detector, they observe only the projection of the fragment momentum triangle on the detector. A

Monte Carlo restoration technique [41] has been applied to reconstruct the Dalitz plot of the momentum geometries after DR. Datz et al. studied the dynamics of three-body breakup of H_2O^+ [36, 37]. Their imaging detector is based on microchannel plates and a phosphor screen. A CCD camera and a 16-channel photomultiplier tube (PMT) recorded the position of the fragments and the arrival time difference. In order to determine the nature of the fragments (H atom or O atom) at the centre of the beam axis and in front of the MCP, a thin foil has been placed. The thickness of the foil has been chosen such that 250 keV H atoms are stopped and only the 4 MeV O atoms pass. The branching ratio between two different dissociation limits has been measured. Once the nature of the fragments is known, the angular distribution between the hydrogen and oxygen atoms can be determined as well as the distribution of kinetic energy over the hydrogen atoms. This allows qualitative descriptions to be made on the reaction mechanism [38], i.e., synchronous, simultaneous etc. The possibility of identifying particles using the foil thickness is, of course, unique for very fast beams (MeV) ion beams.

At TSR, one uses the foil technique for Coulomb explosion experiments [40]. Their detection system is somewhat similar to the one in Ref. [14–16], by mass- and charge-selection of the fragments prior to the detection on three multiparticle imaging detectors.

1.3 Ion and electron imaging techniques

The ion imaging technique has been applied to the study of photodissociation [5, 42–52], multiphoton ionization [53–55], photodetachment [56], inelastic scattering [57,58], photofragment alignment [67, 68], etc. In a typical ion imaging apparatus, the gas of interest, often seeded in a carrier gas, is supersonically expanded through a pulsed valve, collimated using a skimmer, and introduced through a hole in the repeller plate into the apparatus. Between the repeller plate and the extractor plate, one or more pulsed linearly-polarized laser beams cross the molecular beam at 90 degrees. The photons are absorbed by the molecules and the reaction is induced. The fragments resulting from the reaction receive a velocity component corresponding to the kinetic energy released during the fragmentation process. Shortly after production, the fragments are ionized by a ionization laser beam and extracted by the static electric field present between the repeller and the extractor plate. The photofragments are accelerated towards the detector. In the field region this KER velocity component changes the spatial distribution of fragments from one point to a growing sphere. In Fig. 1.3 we show the spatial particle distribution development from the reaction origin to the detector. Consider a dissociation process in which all fragments move isotropically with one well defined velocity. Immediately after dissociation the fragments are ionized and extracted. We concentrate our attention on two fragments that fly in opposite directions along the setup axis, z. The particle moving towards the detector

is accelerated and leaves the field region first. The velocity upon leaving the field (G) is $v_f = \sqrt{v_o^2 + 2a_1d_1 + 2a_2d_2}$. The fragment moving backwards is first decelerated by the electric field until the turning point, and then accelerated back, towards the detector. This fragment is the last one to leave the interaction region. At the moment when it passes the reaction origin (O), it has regained its original velocity only that the vectorial orientation is changed by 180°. From that point, the kinematic of this fragment is identical to that of the other, forward moving fragment. When leaving the field region, the backward flying fragment has a velocity $\overrightarrow{v}_b$ equal to $\overrightarrow{v}_f$. Since in the field free region the velocity is conserved, the relative velocity between the backward and forward fragments is zero and, therefore, the distance between them, d, is preserved. Both fragments arrive at the detector on the same central spot. Consider now another molecule that dissociates along the y axis. The fragments, before being ionized move away from this axis with a velocity $\overrightarrow{v}_y$, corresponding to the kinetic energy released in the process. After ionization, the fragments are accelerated in the electric field and move towards the detector. The extraction field intensity is in the order of 1 kV/cm, while the kinetic energy release is around 1 eV, three orders of magnitude lower than the energy gained in the extraction field. At the exit (G) the fragments are separated in space due to the KER component $\overrightarrow{v}_y$ and the distance between them is d, but their velocity is dominated by the z component $\overrightarrow{v}_z \gg \overrightarrow{v}_y$. Compared with the first pair of fragments, flying along the setup axis, $\overrightarrow{v}_z$ is slightly smaller than $\overrightarrow{v}_f$ or $\overrightarrow{v}_b$. Along the z axis, the relative velocity is zero, while along the y axis the relative velocity is $2 * v_y$. Before entering the field free region, the spatial distribution of particles is still a sphere with a radius of $d/2$. In the field free region, the *pancaking* effect takes place. During the time-of-flight, the fragments have a constant separation along the z axis, while along the y axis the separation increases with $\Delta d = 2v_y t_{TOF}$, where t_{TOF} is the time-of-flight in the field free region. The distribution of particles is stretched in the (x, y) plane and the sphere shape transforms into a pancake, whose thickness $d = v_f * t_{turn}$ depends on the extraction field strength and whose radial length in the detector plan $R = v_y * (T_{field} + TOF)$, is proportional to the KER and the total time-of-flight from the origin to the detector. The three dimensional *pancake* is then projected onto the detector.

A position sensitive detector, often a combination of MCPs, phosphor screen and a CCD camera records the (x, y) coordinates of each fragment that reaches the detector. Images are obtained by integrating on the CCD chip over many laser shots, facilitating this way the data acquisition. The three dimensional distribution can be recovered from the two dimensional projection provided that the initial distribution has a cylindrical symmetry along an axis parallel to the detector. In this case, mathematical transformations (e.g., the inverse Abel transform) can be used to reconstruct the original 3D distribution.

The images contain information about the kinetic energy released in the dissociation process, the radial size of the rings being directly proportional to the initial velocity received in the reaction. They also contain information about the nature of

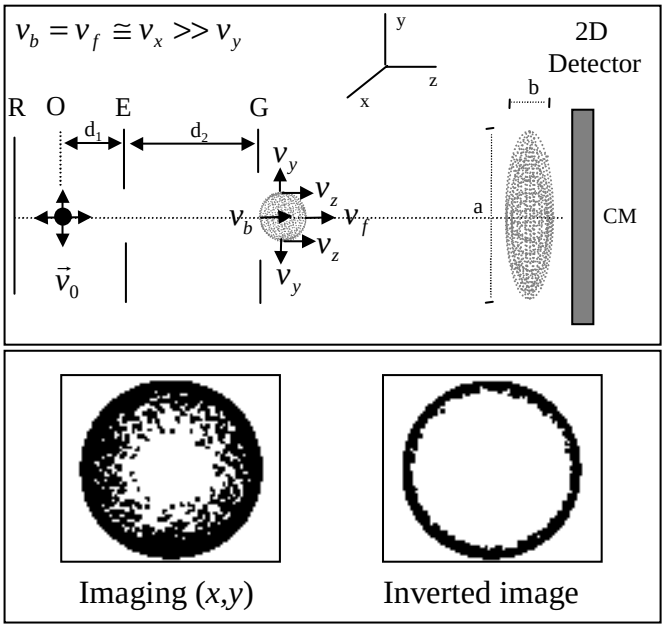

Figure 1.3: *Ion Imaging schematics. The repeller plate (R), the origin of the reaction (O), the extractor plate (E) and the ground plate (G) are indicated. a)Pancaking effect: The particles leave the electric field region with approximately the same extraction velocities (along the* ***z*** *axis) such that along this axis the radius of the sphere is conserved* $(b = cst.)$*. Along the* ***y*** *axis, the fragments move with a non-zero relative velocity* $(2v_{diss})$ *and the distance between them increases in time* $(a > b)$*. b) The detector records the 2D image of the projected pancake distribution. Mathematical procedures reconstruct the 3D distribution.*

the transition and the time scale for the dissociation process. It has been predicted and also observed that correlation among the laser polarization vector, the transition dipole moment vector, the recoil velocity of the photofragments and the rotational angular momentum vector lead to an anisotropic distribution of the fragments [59,60]. In the case of a one photon transition, the angular intensity distribution in the image can be linked to the symmetry of the electronic states involved in the transition. The intensity of a point on the ring corresponding to an angle θ (defined by the recoil velocity with respect to the laser polarization), can be expressed as:

$$I(\theta) \sim [1 + \beta(\tau)(\frac{3}{2}\cos^2(\theta) - \frac{1}{2})], \tag{1.5}$$

where $\beta(\tau)$ is the anisotropy parameter. For a parallel transition ($\Delta\Omega = 0$) followed by a fast dissociation process, the anisotropy parameter $\beta = 2$ and $I(\theta) \sim \cos^2(\theta)$ while for a fast perpendicular transition ($\Delta\Omega = \pm 1$) $\beta = -1$ and $I(\theta) \sim \sin^2(\theta)$. Theory shows that for long-lived predissociation states, the values of β becomes $\beta = 0.5$ for parallel transitions and $\beta = -0.25$ for perpendicular transitions. This reduction is due to the rotational motion between the excitation and dissociation steps.

Similar to the ion imaging technique, the photoelectron imaging technique has been developed by Helm [53, 54, 61] to study the multiphoton ionization of atoms. The photoelectrons are generated with kinetic energies related to the initial state. The experimental setup is similar to the one used for ion imaging, only being adapted to electron detection. The photoelectron angular distribution in the detector plane is a direct projection of the squared angular wave function.

The ionization mechanism of atoms in an electric field, close to the saddle point has been studied in detail with slow photoelectron imaging [62], in this case investigating the photoionization of Xe atoms in a *dc* electric field.

A great improvement to the photoelectron and photofragment imaging technique was achieved in 1997 by Eppink and Parker [52,63] with the so-called "velocity map imaging" technique. Previously, it has been believed that a uniform electric field between electrodes projects without distortions the distribution of fragments on the detector. Therefore, fine wire grids had been used as electrodes. By removing the grids the detection efficiency is increased and, by setting the correct voltages on the opened electrodes, the system acts as ion optics, focusing all of the fragments with the same velocity onto the same spot on the detector, irrespective of the exact place of the fragment in the (x, y) plane of the ionization. The images are, therefore, much less blurred and the relative energy resolution is increased from $15 - 20$ % to $2 - 5$ %. With this improvement, the photofragment imaging technique became a powerful tool for the investigation of photodissociation processes. The increase in resolution made this technique able to compete with the KER resolving power of coincidence techniques.

Since the development of ultrafast and powerful lasers, studies of the spatial-

alignment of molecules in the presence of intense laser fields became possible. The anisotropy of the fragment angular distribution has been observed and investigated in multi-electron dissociative ionization (MEDI) experiments. Initially the experiments were performed using time-of-flight techniques. The anisotropy in the fragment distribution has been interpreted as 'geometric alignment', i.e., a dependence of the ionization rate on the angle between the internuclear molecular axis and the laser polarization [64]. Later work showed that, at very strong laser field, the linearly polarized laser induces a torque on the molecules, orienting them along the laser polarization prior to dissociative ionization [65]. This process is known as 'dynamic alignment'. More recent work has also shown that both processes are responsible for the angular anisotropy [66]. Since the nature of the process appears in the angular distribution of the fragments, the velocity map imaging technique is more suitable than TOF technique for investigating of spatial alignments [67, 68]. Using velocity map imaging technique, the influence of the pulse duration and the energy of short infrared laser pulses on the angular distributions of fragments resulting from MEDI of I_2 and Br_2 has been investigated. The angular distributions are obtained directly from the images and repeated measurements with the laser polarization rotated as is required in the case of TOF technique, are not necessary.

In all of these experiments, the detection system is a position-sensitive detector providing the 2D image of the projected particle distribution. These images can be analyzed only if the initial distribution of fragments has a cylindrical symmetry around an axis parallel to the detector plane. For the analysis of the images and the reconstruction of the initial 3D distribution, mathematical procedures have been developed, for examples, the Abel- inversion method, 'onion peeling' numerical algoritm [69, 70], regularization method [61], iterative inversion algoritm [71]. The idea behind all these methods is to reconstruct the velocity vector of the photofragments from the pixel intensity.

An alternative to reconstructive procedures are the slicing techniques. The idea is to selectively detect slices of the spherical distribution of the particles, i.e., slices that are parallel to the detector. All the particles belonging to one slice arrive roughly in the same time at the detector and, therefore, no information is lost. One method to selectively ionize and detect only fragments with velocity oriented perpendicular to the setup axis is by setting the ionization laser wavelength on the center of the Doppler profile [72]. Another method is to delay the ionizing laser until the distribution of fragments expanded into a sphere. In this case, the ionizing laser has the profile of a laser sheet [73]. Recently, a new slicing method has been developed by Kitoupolus based on the delayed pulsed extraction of the ions [74]. They combine the delayed pulsed extraction with a narrow detection time gating, such that they can selectively image the central slice of the distribution.

In this thesis, the use of a double exposure CCD camera in a velocity map imaging experiment has been presented [75]. The camera measures not only the (x,y) positions but also the arrival time (t) of the fragments. No reconstruction procedures are

required.

1.4 Comparison between techniques

Having been developed in parallel, fast beam techniques and ion imaging techniques show different features which makes one technique preferable to the other for the study of a specific reaction. The most common processes that have been studied are presented in Table I. The fast beam techniques have the advantage of imposing less experimental restrictions and having larger applicability.

Table I. Comparison between techniques. We present the characteristic aspects of the techniques as they appear in most of the experiments.

Characteristics	*Fast Beam/Storage Ring*	*Ion Imaging*
Type of reaction	photodissociation [6–13]	photodissociation [5, 42–52]
	photodetachment [19–22]	multiphoton ionisation [53–55]
	CID [14–16]	inelastic scatering [57, 58]
	DR* [28, 30–39]	Photofragment alignament [67, 68]
	Coulomb explosion[a] [40]	
Reaction region	flexible	small
Laser	not required	required[b]
Symmetry	not required	required[c]
Detected products	neutrals and ions	only ions
	only neutrals*	
Detectors	3D, 2D*	2D
Particles per frame	few[d]	unlimited
Detection rate	low	high
Resolution	high	high

*applies only for DR studies in storage rings.

[a] The Coulomb explosion is foil driven.

[b] most ion imaging experiments require a well defined reaction region and a well defined moment of the reaction for a gated detection. A pulsed laser provides both.

[c] a symmetry axis is required for reconstructing the 3D information from the 2D image.

[d] coincidence experiments restrict the maximum number of particles detected per laser shot.

The reaction can be induced by interaction with photons, electrons, ions or collision gases. A well defined interaction region is convenient for an increased resolution but not required (the length of the interaction region along the z axis can easily be 1-2 cm). In case of ion imaging techniques, the size of the reaction region plays a much stronger role on the resolution of the system. For a sharp image, a very small reaction region, especially on z direction towards the detector, is required (size < 0.5 mm). This is usually achieved by using a focused laser to induce the reaction. The reaction products that are detected in a fast beam experiment are usually neutrals. In principle, ions can also be detected if special care is paid to the stray fields. Ion imaging techniques are based on the field extraction of the fragments and, therefore, only deal with charged particles. An additional laser is often required to ionize the neutral fragments resulting from a reaction prior to detection. The use of ionizing laser in the ion imaging techniques opens up few possibilities. The selectivity of the ionization step makes it possible to select specific fragments. The vectorial properties of the laser ionization process imply that the images may reveal alignment or orientation of the photofragments. A disadvantage is the fact that the ionizing laser may interfere with the dissociation process.

Since the fast beam detection is three-dimensional, the kinematics of the reaction are encoded in the measured coordinates and in the timing and no further mathematical procedures are required. The correlated position and timing information often helps in identifying if the fragment is a result of a induced reaction or from a background process. Fast beam techniques can better handle the presence of background signals and, therefore, they can be used in very low signal-to-noise experiments. The standard ion imaging detection consists of recording two-dimensional images of the projected 3D distribution of particles on the detector surface. Symmetry requirements on the reaction must be carried out before applying reconstruction methods.

The major advantage of ion imaging techniques is in dealing with a large number of fragments per laser shot. The maximum number of particles is in principle only limited by the number of pixels in the CCD chip. In the case of fast beam techniques, the more complex detection system, i.e., also recording the arrival time of the particles, drastically reduces the maximum number of particles that can be detected per laser shot. Often, only two particles can be detected. Recently, 3D detection systems have been developed for measuring more than two particles. However, coincidence experiments which are based on the recognition of the fragments coming from one reaction can only deal with a limited number of fragments per laser shot. In conclusion, the complexity of a 3D detection system often has the disadvantage of a decreased detection count rate.

1.5 Detection systems

In the case of ion imaging techniques, the most common detection system is a 2D detector consisting out of a CCD camera that records the (x, y) position of the particles. Fast beam techniques paid more attention to the detection systems. The detector used in the first fast beam experiment by Los and coworkers was a 3D detector, i.e., a combination of an MCP and multianodes [3, 4]. This detector was used for detecting two fragments in coincidence. The (x, y, t) information is decoded by analyzing the charge distribution over the anodes. The multianodes provide the time when the particles hit the detector (with ~ 500 ps resolution) and the distance between them (~ 70 μm resolution).

Different types of time- and position-sensitive detectors based on charge division have been developed (e.g., resistive anodes, wedge-and-strip anodes and delay-line anodes), providing good position resolution, but relatively long recovery times on the time scales of molecular dynamics (< 50 ns). These detectors were used for two-particle detection. Segmented anodes with individual readouts are able to detect more particles in coincidence but, as a drawback, their position resolution is rather low. All of these detectors with an electronic readout have the advantage of working at kHz repetition rates.

Other type of detectors are those combining microchannel plates (MCPs) with phosphor screens. CCD cameras are used to record the light coming from the phosphor screen and to retrieve the (x, y) coordinates of each particle, while the timing t is recorded with other devices like multichannel photomultiplier tubes. These detectors handle multiparticle detection, but acquisition rate is limited by the readout of the CCD camera.

At the end of this instrumental overview we would like to presents two detection schemes suitable for low signal experiments that have been used in our fast beam apparatus. One is a combination of a 16-strip PMT and a CCD camera, based on a scheme developed by Amitay and Zajfman [30]; the second one is a double exposure CCD camera.

1.5.1 16-strip PMT and CCD camera

Inside the apparatus, a double MCP stack and a phosphor screen are used to detect the fragments. Outside the vacuum, a CCD camera and a 16-strip PMT detect the flashes from the back of the phosphor screen providing the (x, y) position and the arrival time t of the particles. We present the use of this detector in a fast beam experiment. The process chosen for testing this new detection scheme is the predissociation of triplet Rydberg states of molecular hydrogen. In our apparatus we produce a molecular beam of H_2, from which the $c^3\Pi_u^-$ state is metastable and survives during the time-of-flight. A tunable pulsed UV laser excites selectively different ro-vibrational Rydberg states ($n > 11$). Once these states are populated, the decay processes that take place are

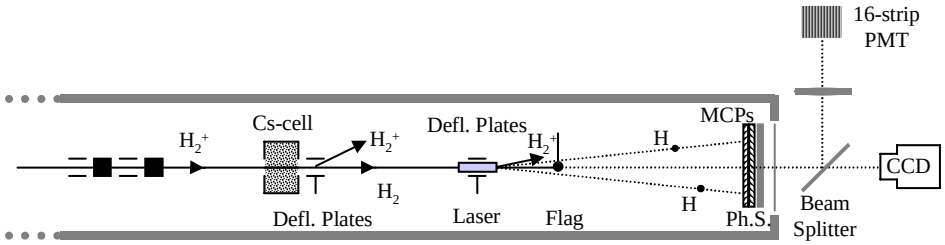

Figure 1.4: *Schematic of experimental setup. A continuous molecular beam of H_2^+ is extracted at 5 keV from the ion source. The molecular beam is crossed by a 50 Hz UV laser beam ($\lambda \sim 350$ nm). The fragments resulting from predissociation and having enough KER escape the beam dump and arrive on a time- and position-sensitive detector consisting out of two MCPs and a P 46 phosphor screen. A transparent window allows the light from the back of the phosphor screen to reach, via a beam splitter, the CCD camera and a 16-strip PMT.*

mainly autoionisation and predissociation. In the case of a dissociation event, the aim is to detect both particles and to measure their position and arrival time difference and to calculate the kinetic energy released in the dissociation process.

Experimental setup

A hollow cathode discharge ion source produces H_2^+ ions mainly in $X\ ^2\Sigma_g^+$ ground state. The plasma discharge is stabilized at 600 V and 20 mA. The filling gas is a combination of molecular hydrogen and molecular nitrogen. The nitrogen is used to initiate the discharge and to stabilize it. The pressure inside the vacuum chamber is around 10^{-5} mBar. The ions are extracted and accelerated up to 10 keV. A Wien filter selects the ions of interest, in this case the H_2^+ ions. Four pairs of deflection plates (two horizontal and two vertical) guide the beam towards the detector. A set of Einzel lenses are used to focus the beam in the interaction region with the laser. The result is a collimated, fast and continuous ion beam.

Next, the ion beam must be neutralized in order to prepare triplet excited states of H_2. The neutralization can be done via inelastic, charge-transfer collisions with a target gas. Cesium is a very good choice due to the fact that the energy exchange in the reaction (3.98 eV) matches the energy difference between the $X^2\Sigma_g^+$ and $c^3\Pi_u$ states. An oven filled with liquid Cs is heated up to 100 °C. The Cs vapor diffuses into the upper part of the oven where a 3 mm long reaction cell is located. The beam passes through this cell and the charge transfer process takes place. It is estimated that approximately 10% of the ion beam is neutralized. The size of the neutral beam at the exit of the collision cell is approximately 1 mm in diameter. The rest of the parent ion beam is deflected away at the exit of the cell. The interaction region with the laser is situated 50 cm away from the collision cell (see Fig. 1.4). The laser beam crosses the molecular beam at 90 degrees. The laser beam is line focused by a cylindrical lens in order to increase the overlap of the neutral beam and the laser. The length of the focus line is adjustable. An increase in the length leads to a decrease in the energy resolution and, therefore, a compromise has to be made. A length of 1.5 cm has been found to be optimal.

The laser system used for this experiment consists of a Spectra Physics Nd-YAG laser, which has a repetition rate of 50 Hz, pumping a Lambda Physik ScanMate dye laser (LDS 698). The energy of the Nd-YAG laser is 400 mJ per pulse. The output of the dye laser is frequency doubled in a doubling unit consisting of a KDP-C nonlinear crystal and an angle-correction alignment block. A Pellin-Broca prism separates the second harmonic ultraviolet beam (UV) from the dye laser fundamental beam. The UV light can be tuned around 350 nm to excite the molecules from the $c^3\Pi_u^-$ state to a high-lying Rydberg state ($n > 11$). The acquisition program controls both the ScanMate and the position of the doubling crystal and also ensures that the dc motor, which turns the doubling crystal, is adjusted simultaneously to track the dye laser wavelength such that the UV output remains constant during the entire scan.

Due to the short lifetimes of the Rydberg states, the laser interaction region also represents the reaction region where photodissociation and photoionisation take place. Further downstream towards the detector, a small flag (ϕ = 1.2 mm) captures the undissociated neutral beam. Most of the fragments resulting from the dissociation process have enough extra kinetic energy to fly apart, escape the beam dump and reach the detector.

PMT and CCD detection system

For a complete description of the predissociation process, a 3D detector is necessary. As mentioned before, inside the vacuum system there is a set of two MCPs and a phosphor screen (P46). The two neutrals resulting from a dissociation event, each of them carrying 2.5 keV kinetic energy, will hit the front side of the MCP stack. The voltage applied on the front of the MCPs is -2 kV while the voltage applied on the phosphor screen is +3 kV with respect to the backside of the MCPs. A transparent

window allows the flashes from the phosphor screen to be transmitted outside of the vacuum system.

A beam splitter (70% transmission, 30% reflection) is located in front of the window, such that the light from the phosphor screen can be focused onto both a CCD camera and a 16-strip photomultiplier tube PMT (see Fig. 1.4). The light is focused on the camera sensor (256x256 pixels) by a lens ($f = 50$ mm). The CCD camera is used to record the (x, y) position of the particles. The camera frame is read out and analyzed by a frame grabber installed in the PC. For each frame, the high intensity spots corresponding to the detected particle are located and only their centre-of-mass coordinates are stored. This procedure saves time in the read-out of the frames and allows operation of the camera at 50 Hz

The reflected 30% of the light is focused onto a fast multi-line photomultiplier tube (consisting of 16 parallel strips, 0.8 mm wide, separated by 0.2 mm). The data flow is presented in Fig. 1.5. The signal from the PMT goes directly to a Constant Fraction Discriminator (CFD module 3420 from LeCroy) which has 16 input channels to match the output of the PMT. The logical OR output from the CFD unit represents the detector trigger pulse. This pulse has several purposes. It provides the common veto for the CFD unit, limiting the length of the timing gate and it also triggers the measuring gate for the ADC (see Fig. 1.6). Each CFD channel has a programmable threshold level (typically 200 mV) and the output from each CFD channel is a constant current pulse that is initiated at the arrival of signal from a PMT channel and is stopped by the common veto. The length of the CFD output is recorded by a 16-channel charge sensitive analogue to digital converter (ADC LeCroy model 4300 B). The gate pulse must be provided to the ADC at least 20 ns before the arrival of the CFD output signal, to allow a proper and accurate conversion. Therefore, the CFD output is delayed by about 50 ns such that the ADC gate can be begun in time. Both the CFD and ADC operate in a CAMAC environment, controlled via GPIB by the PC.

The complexity of a detector which allows not only position measurements but also time measurements has the counter effect of a low count rate. Both particles resulting from the dissociation have to be detected by three independent detectors, i.e., MCPs, PMT and CCD. The probability that one particle is detected by the MCPs is $P_{MCP} \sim 0.6$. The detection probability of the PMT is $P_{PMT} \sim 0.8$ while the detection probability of the CCD is $P_{CCD} = 0.8$. The probability to detect both particles resulting from a dissociation event is $P_{diss} = P_{MCP}^2 * P_{PMT}^2 * P_{CCD}^2 = 0.15$. In conclusion, only 15% of dissociation events are completely detected. This is still a simple estimation of the efficiency of the detector, neglecting situations in which both particles are detected but the dissociation event must be still rejected from other reasons, for example when both particles hit the same PMT strip. Another unwanted aspect of using such a PMT is the fact that very often one particle hits two adjacent strips. To be absolutely certain about the unique correspondence between a particle and a strip, it is necessary to require that at least one un-triggered strip lies in between

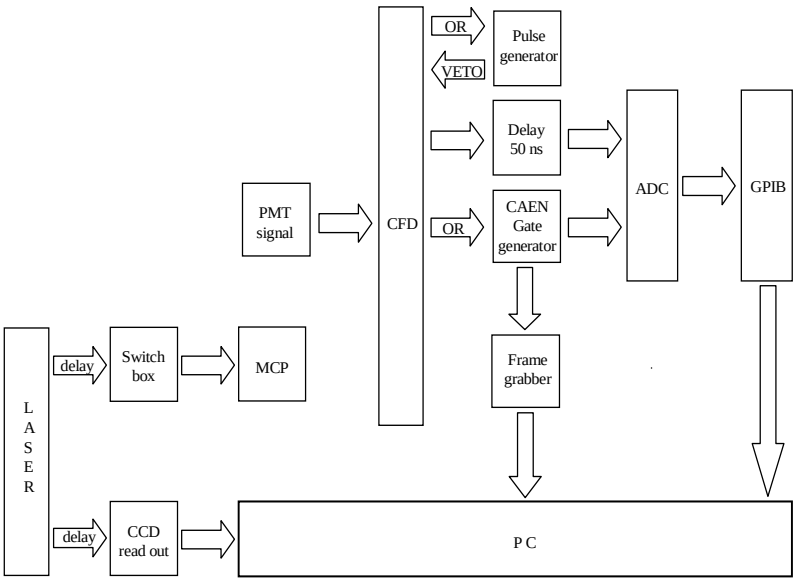

Figure 1.5: *Electronics and data flow. Laser is the master clock of the experiment. It triggers the switch box of the MCP, allowing particles to be detected. It also triggers the read out of the CCD camera. When the first flash arrives on one of the PMT strips the signal triggers the CFD unit. The logical OR output from this CFD unit represents the detector trigger pulse. This pulse has several purposes. It provides the common VETO for the CFD unit, limiting the length of the timing and it triggers the measuring gate for the ADC Each CFD channel has a programmable threshold level (typically 200 mV). The output from a single CFD channel is a constant current pulse that is started at the arrival of signal from a PMT channel and it is stopped by the common VETO. The length of the CFD output is reported by a 16-channel charge sensitive analogue to digital converter (ADC LeCroy model 4300 B). Both the CFD and ADC operate in the CAMAC environment.*

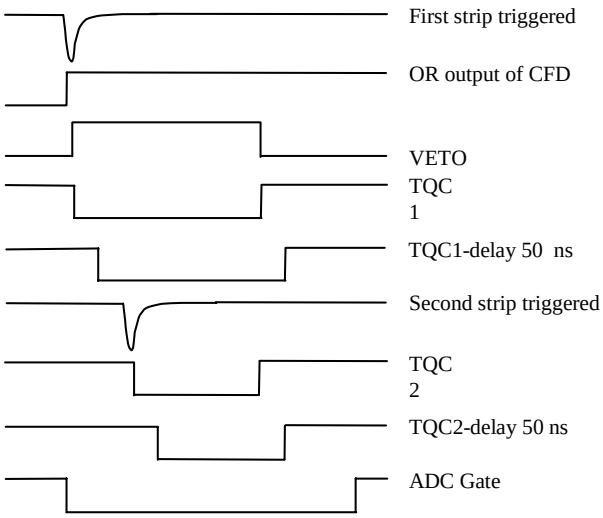

Figure 1.6: *When the light from the phosphor screen arrives on one of the PMT strips a signal reaches the CFD unit. The logical OR output of the CFD unit provides the common VETO for the CFD unit, limiting the length of the timing and it triggers the measuring gate for the ADC unit.*

two triggered ones. This requirement reduces the number of active strips to 8 and with this also the maximum number of particles detected in coincidence. Still, the possibility of detecting more than two particles is very useful by allowing more than one dissociation event during one laser shot. It also allows the detection of background particles together with those from dissociation events since a centre-of-mass selection discriminates away the background particles.

A major problem faced with during this experiment was dealing with very low signals in the presence of a large background. As was described earlier, the H_2 molecular beam is continuous while the laser is pulsed. The detection scheme has to take into account this aspect in order to avoid a huge background-to-signal ratio. The background signals consist of parent molecules that escape the flag or spontaneous dissociation events which are not related to the interaction with laser. The "real" signal is due to ions resulting from autoionisation reactions and neutral fragments resulting from predissociation reactions which are produced in the presence of the laser. Since the duration of the laser pulse is only 5 ns, it is to be expected that the signal is completely covered by the continuous background.

One way to avoid this is to chop the ion beam. It turns out that the temporal and spatial overlap of the pulsed laser with the chopped beam is not trivial. After optimization, the signal is lower than that obtained with the continuous beam. A more efficient method to dramatically decrease the background is to keep the neutral beam unchopped but to gate the detection system, achieved by varying the voltage on the front side of the MCPs. Between laser shots a low voltage on the MCPs strongly decreases the detector efficiency such that background particles are not detected while, after the laser is fired, an increased voltage on the MCPs allows detection of the laser induced fragments. The idealized sequence of events is presented in Fig. 1.5. The laser is the master clock of the system. When the Q-switch of the laser is fired, an output signal is sent to a SRS Pulse Generator to create a delayed pulse. This pulse has a delay of ∼1.5 microseconds, corresponding to the time-of-flight of the particles from the laser interaction region to the detector and a duration of ∼200 ns. The signal is then sent to the switch box which controls the voltage on the front side of the MCPs. Between laser shots the voltage is set at -1200 V. This signal raises the voltage to -2000 V and the MCPs are then operational mode for only 200 ns. During this time the particles resulting from a laser induced process arrive at the detector.

Assume that a pair of particles strike the detector producing two flashes on the phosphor screen. The flashes are sequentially imaged onto two different strips of the PMT. Two CFD channels are activated and the CFD logical OR output generates two signals: a signal sent to the VETO input of the CFD unit as a common stop for all the output signals from CFD and a gate signal for the ADC (see Fig. 1.6). The information from the ADC is transferred to the PC via a GPIB interface. The acquisition program combines the time information from the GPIB with the position information from the frame grabber. In addition, when the acquisition is performed in a scanning mode, the wavelength corresponding to each laser shot is also recorded.

The detection system was tested by studying the predissociation of high Rydberg states in molecular hydrogen. If sufficient energy is given to the molecule it can either predissociate or autoionize. In a dissociation process the two neutral fragments must be detected by both the CCD camera and PMT. The information consisting of the (x, y) position of the particles on the detector and the arrival time difference is necessary for estimating the kinetic energy released in the process (see Eq. (1.4)).

Although the detection is gated, the background signal is still high with respect to the signal of interest. Therefore, it is necessary to verify that the two particles detected are indeed products from a dissociation process. This is obtained by centre-of-mass restriction. For a real event, the centre-of-mass is found in the middle of the detector in a region defined by the initial parent ion beam.

The kinetic energy release is the "fingerprint" of the Rydberg state we investigate and adding the KER to the energy of the dissociation limit, the energy of the excited Rydberg state can be obtained. A KER histogram is presented in Fig.1.7. The UV wavelength is fixed at 349.445 nm. The KER spectrum reveals two peaks, which are associated with two transitions from different vibrational levels. The first peak

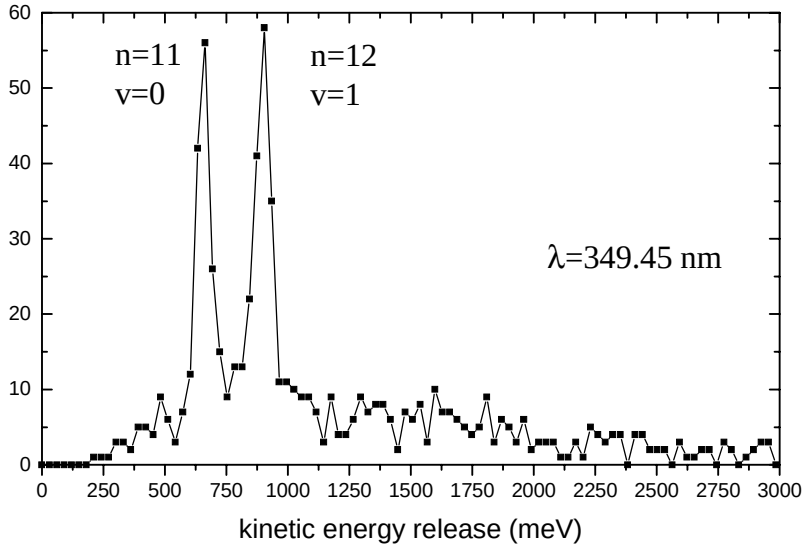

Figure 1.7: *Kinetic energy release distribution at an excitation wavelength of 349.445 nm. Two vibrational peaks corresponding to the excitation of two different Rydberg states are clearly distinguished.*

corresponds to the excitation of $n = 11$, $v = 0$, $R = 4$ Rydberg states. The second peak, appearing at higher KER, is related to the excitation of $n = 12$, $v = 1$, $R = 3$ Rydberg states. The measured FWHM of the peaks is $\sim$ 60 meV. The position resolution of the detector is determined by the accuracy in the focus of the phosphor screen area onto the CCD chip (1 pixel $\sim$ 150 μm). The time resolution is determined by the CFD ($\sim$210 ps). The main contribution to the rather large width of the KER peaks is the uncertainty of the reaction origin on the z axis, i.e., along the laser line focus. The 2 cm length of the laser focus translates into a 1.6% uncertainty in the measured distance between reaction place and detector surface L (see Eq. (1.4)). In terms of KER the relative error is $\sim 3.5\%$ corresponding to a width of the KER peak centered at 700 meV of 55 meV. Assuming that laser focus is reduced to a point, the KER relative error is reduced to $\sim 1.5\%$. This corresponds to a 20 meV width of the same KER peak.

In conclusion, the combination of a 16-strip PMT and a CCD camera is a suitable 3D multiparticle detection system, providing both good position and time resolution. This detector has been tested in a coincidence experiment of the predissociation high Rydberg states of H_2. The number of particles detected in coincidence is limited by

the number of PMT strips. The complexity of the detector due to 3D capabilities has the disadvantage of a rather low detection efficiency.

1.5.2 3D double exposure CCD

The second detection scheme used in our fast beam apparatus was a novel 3D double exposure CCD camera able to record the (x, y, t) coordinates of an "unlimited" number of particles. With respect to the PMT and CCD detector, this new system has the advantage of a higher efficiency detection, due to the fact that the light from the phosphor screen must be recorded by one device only. In addition, the number of particles detected is, in principle, only limited by the resolution of the CCD chip. These aspects make the double exposure CCD camera suitable for both fast beam and ion imaging techniques.

The time measurement is based on the decay characteristics of the phosphor screen which is recorded in two successive images by a double exposure CCD camera (LaVision, modified Imager3 VGA). The camera is placed behind the phosphor screen to record the intensities of the spots corresponding to the individual ions. Due to the fast interline transfer of the CCD chip, the camera is capable of taking two successive images of the same phosphor decay for each event that originates from a single laser pulse. Subsequently, the arrival time can be found for each event from the ratio of intensities measured in both images [76]. This principle is visualized in Fig. 1.8 and is very similar to the approach of Strasser et al. [77], who used two CCD cameras, one of which was gated. On the left hand side of Fig. 1.8 two particles, a and b, are detected by the MCP and phosphor screen imaging detector emitting localized phosphorescence which is recorded by the camera. The right hand side of the figure shows the temporal picture. Both events emit similarly decaying phosphorescence which, for a P46 phosphor, has a decay time of 300 ns (decay of light intensity from 90% to 10%). The curves are shifted in time according to their arrival times, t_a and t_b. The CCD camera takes two successive images in the time intervals $G_1 = [-t_1, 0]$ and $G_2 = [0, t_2]$. These define the exposure times and the integrals of the two parts of the emitted phosphorescence that yield intensities I_1 and I_2. It is easy to see that early events (i.e., a) appear more intense in the first image and late events (i.e., b) more intense in the second. By taking the ratio of intensities $R = I_1/I_2$ a direct measure for the arrival time $R(t)$ is found. Around $t = 0$ the camera makes a fast interline transfer of the charge accumulated on the light sensitive pixels to their neighboring storage pixels. Since this process is not instantaneous ($40 - 60$ ns per pixel) or synchronous across the chip (up to 100 ns shift), the characteristics of the CCD camera-phosphor combination has to be calibrated to obtain the $R(t)$ curves for each (x, y) position on the chip.

The calibration procedure used an image intensifier with the same phosphor (P46) which was then evenly illuminated with light from a pulsed doubled Nd:YAG laser at 532 nm. Double exposure images were taken at different time delays between the

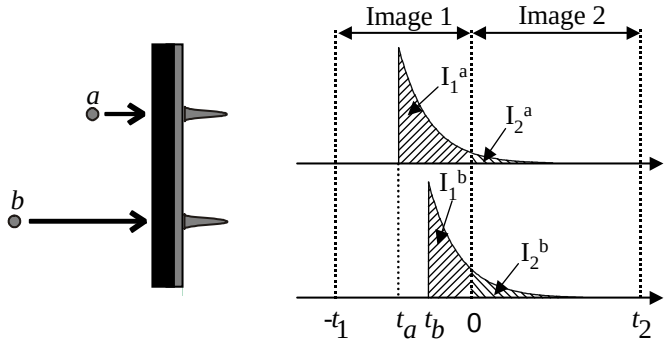

Figure 1.8: *The principle of the arrival time determination using a double exposure CCD camera. The arrival of the particles* **a** *(at time* t_a*) and* **b** *(*t_b*) generates phosphorescence with a characteristic decay constant, measured in Image 1. After* $t = 0$ *the phosphorescence is integrated in Image 2. The intensity ratio of each spot between both images reveals the relative arrival time.*

laser and the switching moment of the camera. This calibration procedure yields a lookup table connecting (x, y, R) with the appropriate value of t. In the experiment the original images of 640x480 pixels are 2x2 hardware binned to 320x240 pixels, after which each event typically covers 3x3 pixels. The binning allows a 25 Hz repetition rate for data acquisition. The centroid position on this grid is then determined at subpixel resolution.

The intensities I_1 and I_2 of a single event in both images can be found from a summation over the contributing pixels belonging to that event. However, for an accurate determination, a weighted summation over the participating pixels is used. The intensity ratio is found as follows:

$$R = \frac{\sum g_i I_1^i}{\sum g_i I_2^i}, \; g_i = \sqrt{I_1^i + I_2^i} \tag{1.6}$$

where the weighting factor g_i is calculated from $g_i = 1/S_i$ where $S_i = 1/\sqrt{I_1^i + I_2^i}$ is the relative error in the sum intensities assuming Poisson statistics and I_1^i and I_2^i are the intensities of pixel i in the image 1 and 2, respectively. In this way the more intense pixels contribute more to the ratio than the less intense ones suppressing the consequences of camera noise. The most accurate time determinations are found for high signal intensities for both images. In an experiment performed in the group of

Andresen in Bielefeld [76] an image intensifier was illuminated with a picosecond diode laser to measure the resolving power in time. Applying 2x2 pixels binning, a relative time accuracy of 1-1.5 ns was found (standard deviation of the times determined for all pixels).

For the following experiments presented in this thesis, the double exposure CCD camera was chosen as detection system mostly due to the increased efficiency detection and the higher number of particles that can be detected per laser shot.

Bibliography

[1] G.H. Dunn, and B. van Zyl, Phys. Rev. **154**, 40 (1967)

[2] P.B. Armentrout, S.M. Tarr, A. Dori, and R.S. Freud, J. Chem. Phys. **75**, 2786 (1981)

[3] D. P. de Bruijn, and J. Los, Rev. Sci. Instrum. **53**, 1020 (1982)

[4] H. Helm, D. P. de Bruijn, and J. Los, Phys. Rev. Lett. **53**, 1642 (1984)

[5] D.W. Chandler and P.L. Houston, J. Chem. Phys. **87**, 1445 (1987)

[6] D. P. de Bruijn, and H. Helm, Phys. Rev. A **34**, 3855 (1986)

[7] H. Helm and P.C. Cosby, J. Chem. Phys. **86**, 6813 (1987)

[8] P.C. Cosby and H. Helm, Phys. Rev. Lett. **61**, 298 (1988)

[9] R.E. Continetti, D.R. Cyr, D.L. Osborn, D.J. Leahy, and D.M. Neumark, J. Chem. Phys. **99**, 2616 (1993)

[10] U. Müller and P.C. Cosby, Phys. Rev. A **59**, 3632 (1999)

[11] D. Strasser, X. Urbain, H.B. Pedersen, N. Altstein, O. Heber, R. Wester, K.G. Bhushan, and D. Zajfman, Rev. Sci. Instrum. **71**, 3092 (2000)

[12] M. Braun, M. Beckert, and U. Müller, Rev. Sci. Instrum. **71**, 4535 (2000)

[13] I. Mistrík, R. Reichle, H. Helm, and U. Müller, Phys. Rev. A **63**, 042711 (2001)

[14] J.A. Fayeton, M. Barat, J.C. Brenot, H. Dunet, Y.J. Picard, U. Saalmann, R. Schmidt, Phys. Rev. A. **57**, 1058 (1998)

[15] M. Barat, J.C. Brenot, H. Dunet, J.A. Fayeton, and Y.J. Picard, J. Chem. Phys. **110**, 10758 (1999)

[16] M. Barat, J.C. Brenot, H. Dunet, J.A. Fayeton, Y.J. Picard, D. Babikov, and M. Sizun, Chem. Phys. Lett. **306**, 233 (1999)

[17] K.A. Hanold, A.K. Luong, T.G. Clements, and R.E. Continetti, Rev. Sci. Instrum. **70**, 2268 (1999)

[18] R. Kachru and H. Helm, Phys. Rev. Lett. **55**, 1517 (1985)

[19] T.N. Kitsopoulos, I.M. Waller, J.G. Loeser, and D.M. Neumark, Chem. Phys. Lett. **159**, 300 (1989)

[20] C.C. Arnold, Y. Zhao, T.N. Kitsopoulos, and D.M. Neumark, J. Chem. Phys. **97**, 6121 (1992)

[21] K.A. Hanold, C.R. Sherwood, M.C. Garner, and R.E. Continetti, Rev. Sci. Instrum. **66**, 5507 (1995)

[22] B.J. Greenblatt, M.T. Zanni, D.M. Neumark, Chem. Phys. Lett. **258**, 523 (1996)

[23] D. Kella, M. Algranati, H. Feldman, O. Heber, H. Kovner, E. Malkin, E. Miklazky, R. Naaman, D. Zajfman, J. Zajfman, and Z. Vager, Nucl. Instrum. and Meth. A **329**, 440 (1993)

[24] D. P. de Bruijn, J. Neuteboom, V. Sidis and J. Los, Chem. Phys. **85**, 215 (1984)

[25] L.D. Gardner, M.M. Graff, and J.L. Kohl, Rev. Sci. Instrum. **57**, 177 (1985)

[26] R.H. Dalitz, Philos. Mag. **44**, 1068 (1953); Annu. Rev. Nucl. Sci. **13**, 339 (1963)

[27] S. Datz and M. Larsson, Physica Scripta **46**, 343 (1992)

[28] D. Zajfman, Z. Amitay, C. Broude, P. Forck, B. Seidel, M. Grieser, D. Habs,D. Schwalm, and A. Wolf, Phys. Rev. Lett. **75**, 814 (1995)

[30] Z. Amitay and D. Zajfman, Rev. Sci. Instrum. **68**, 1387 (1997)

[31] Z. Amitay, D. Zajfman, P. Forck, U. Hechtfischer, B. Seidel, M. Grieser, D. Habs, R. Repnow, D. Schwalm, and A. Wolf, Phys. Rev. A **54**, 4032 (1996)

[32] D. Kella, P.J. Johnson, H.B. Pedersen, L. Vejby-Christensen, and L.H. Andersen, Phys. Rev. Lett. **77**, 2432 (1996)

[33] D. Kella, L. Vejby-Christensen, P.J. Johnson, H.B. Pedersen, and L.H. Andersen, Science **276**, 1530 (1997)

[34] S. Rosén, R. Peverall, J. ter Horst, G. Sundström, J. Semaniak, O. Sundqvist, M. Larsson, M. de Wilde, and W. J. van der Zande, Hyperfine Interact. **115**, 201 (1998)

[35] W.J. van der Zande, in Dissociative Recombination: Theory, Experiment and Applications, (World Scientific, 2000), p.251

[36] S. Dats, R. Thomas, S. Rosén, M. Larsson, A.M. Derkatch, F. Hellberg, and W. van der Zande, Phys. Rev. Lett. **85**, 5555 (2000)

[37] R. Thomas, S. Rosén, F. Hellberg, A. Derkatch, M. Larsson, S. Dats, R. Dixon, W.J. van der Zande, Phys. Rev. A **66**, 032715 (2002)

[38] M. Larsson and R. Thomas, Phys. Chem. Chem. Phys. **3**, 4471 (2001)

[39] S. Strasser, L. Lammich, S. Krohn, M. Lange, H. Kreckel, J. Levin, D. Schwalm, Z. Vager, R. Wester, A. Wolf, and D. Zajfman, Phys. Rev. Lett. **86**, 779 (2001)

[40] R. Wester, F. Albrecht, M. Grieser, L. Knoll, R. Repnow, D. Schwalm, A. Wolf, A. Baer, J. Levin, Z. Vager, and D. Zajfman, Nucl. Instrum. and Meth. A **413**, 379 (1998)

[41] B.R. Frieden, in *Picture Processing and Digital Filtering*, edited by T.S. Huang (Springer-Verlag, Berlin, 1979), p. 240

[42] R.O. Loo, G.E. Hall, H.-P. Haerri, and P.L. Houston, J. Phys. Chem. **92**, 5 (1988)

[43] J.W. Thoman, Jr., D.W. Chandler, D.H. Parker, M.H.M. Janssen, Laser Chem. **9**, 27 (1988)

[44] D.W. Chandler, J.W. Thoman Jr., M.H.M. Janssen, and D.H. Parker, Chem. Phys. Lett. **156**, 151 (1989)

[45] D.P. Baldwin, M.A. Buntine, and D.W. Chandler, J. Chem. Phys. **93**, 6578 (1990)

[46] T. Suzuki, V.P. Hradil, S.A. Hewitt, P.L. Houston, and B.J. Whitaker, Chem. Phys. Lett. **187**, 257 (1991)

[47] M.A. Buntine, D.P.Baldwin, and D.W. Chandler, J. Chem. Phys. **96**, 5843 (1992)

[48] V.P. Hradil, T. Suzuki, S.A. Hewitt, P.L. Houston, and B.J. Whitaker, J. Chem. Phys. **99**, 4455 (1993)

[49] B.L.G. Bakker, D.H. Parker, G. Hancocl, and G.A.D. Ritchie, Chem. Phys. Lett. **294**, 565 (1998)

[50] B. Buijsse, W.J. van der Zande, A.T.J.B. Eppink, D.H. Parker, B.R. Lewis, and S.T. Gibson, J. Chem. Phys. **108**, 7229 (1998)

[51] A.A. Bracker, E.R. Wouters, A.G. Suits, and O.S Vasyutinskii, J. Chem. Phys. **110**, 6749 (1999)

[52] D.H. Parker and A.T.J.B. Eppink, J. Chem. Phys.**107**, 2357 (1997)

[53] H. Helm, N. Bjerre, M.J. Dyer, D.L. Huestis, and M. Saeed, Phys. Rev. Lett. **70**, 3221 (1993)

[54] C. Bordas, M.J. Dyer, T. Fairfield, H. Helm, K.C. Kulander, Phys. Rev. A **51**, 3726 (1995)

[55] W.K. Kang, Y.S. Kim, K.H. Jong, Chem. Phys. Lett. **244**, 183 (1995))

[56] C. Blondel, C. Delsart, and F. Dulieu, Phys. Rev. Lett. **77**, 3755 (1996)

[57] L.S. Bontuyan, A.G. Suits, P.L. Houston and B.J. Whitaker, J. Phys. Chem. **97**, 6342, (1993)

[58] N. Yonekura, C. Gebauer, H. Kohguchi, and T. Suzuki, Rev. Sci, Instum.**70**, 3265 (1999)

[59] J.P. Simons, J. Phys. Chem. **91**, 5378 (1987)

[60] P.L. Houston, J. Phys. Chem. **91**, 5388 (1987)

[61] J. Winterhalter, D. Maier, J. Hoerkamp, V. Schyja, and H. Helm, J. Chem. Phys. **110**, 11187 (1999)

[62] C. Nicole, I. Sluimer, F. Rosca-Pruna, M. Warntjes, M. Vrakking, Ch. Bordas, F. Texier and F. Robicheaux, Phys. Rev. Lett. **85**, 4024 (2000)

[63] A.T.J.B. Eppink and D.H. Parker, Rev. Sci. Instrum.**68**, 3477 (1997)

[64] L. J. Frasinski, K. Codling, P. Hatherley, J. Barr, I. N. Ross, and W. T. Toner, Phys. Rev. Lett. **58**, 2424 (1987)

[65] D. T. Strickland, Y. Beaudoin, P. Dietrich, and P. B. Corkum, Phys. Rev. Lett. **68**, 2755 (1992)

[66] J. H. Posthumus, J. Plumridge, M. K. Thomas, K. Codling, L. J. Frasinski, A. J. Langley, and P. F. Taday, J. Phys. B **31**, L553 (1998)

[67] F. Rosca-Pruna, E. Springate, H.L. Offerhaus, M. Krishnamurthy, N. Farid, C. Nicole, and M.J.J. Vrakking, J. Phys. B **34**, 4919 (2001)

[68] F. Rosca-Pruna, E. Springate, H.L. Offerhaus, M. Krishnamurthy, N. Farid, C. Nicole, and M.J.J. Vrakking, J. Phys. B **34**, 4939 (2001)

[69] C.J. Dasch, Appl. Opt. **31**, 1146 (1992)

[70] C. Bordas, F. Paulig, H. Helm, D.L. Huestis, Rev. Sci. Instrum. **67**, 2258 (1996)

[71] M.J.J. Vrakking, Rev. Sci. Instrum. **72**, 4084 (2001)

[72] T. Kinugawa and T. Arikawa, J. Chem. Phys. **96**, 4801 (1992)

[73] K. Tonokura and T. Suzuki, Chem. Phys. Lett. **224**, 1 (1994)

[74] C.R. Gebhardt, T.P. Rakitzis, P.C. Samartzis, V. Ladopoulos, T.N. Kitsopoulos, Rev. Sci. Instrum. **72**, 3848 (2001)

[75] L.Dinu, A.T.J.B. Eppink, F. Rosca-Pruna, H.L. Offerhaus, W.J. van der Zande, and M.J.J. Vrakking, Rev. Sci. Instrum. **73**, 4206 (2002)

[76] R.Bobbenkamp, Ph.D. Thesis, Bielefeld, 2002

[77] D. Strasser, X. Urbain, H. B. Pedersen, N. Altstein, O. Heber, R. Wester, K. G. Bhushan and D. Zajfman, Rev. Sci. Instrum. **71**, 3092 (2000)

Chapter 2

Three-dimensional detection in velocity map imaging

We illustrate the use of a three dimensional (x, y, t) CCD camera detection system in an ion imaging experiment. The time measurement is based on the decay characteristics of the phosphor screen which is recorded in two successive images by a double exposure CCD camera. The strength of the method is illustrated in a velocity map imaging experiment on iodine molecules that are ionized and dissociated by intense femtosecond laser pulses. Singly and doubly charged iodine fragments are detected and their (x, y) coordinates and arrival time are recorded in an event counting routine. We estimate the time resolution of the system to be 1.3 ns. We show that the fragment velocity distribution derived from the (x, y, t) data is similar and in some conditions more accurate than the distribution obtained by an mathematical inversion of the (x, y) data only. This principle of detection can be used in all situations in which inversion methods are impossible, for example, when the particle distribution does not have an axis of symmetry.

2.1 Introduction

In 1987, Chandler and Houston developed the first ion imaging apparatus [1, 2]. On a well defined spot molecules were photodissociated and fragments were ionized. The fragments were accelerated in a uniform field and visualized on the detector. The position-sensitive detector used in their setup consisted of two microchannel plates, a phosphor screen and a CCD camera. The inversion method used to retrieve the three-dimensional velocity distribution was a Hankel transform of the Fourier transform of the projected image. In 1997, Eppink and Parker improved the resolution of the imaging technique by changing the conventional grid electrodes with three-plate open electrodes [3]. This new electrostatic lens avoided distortions present in imaging with grids and by using appropriate voltages on the electrodes, ions with the same velocity vector produced at different positions in the focus were projected on the same point on the detector (on a spot with a diameter of 80 μm). This technique was called velocity map imaging.

In this chapter, we present the use of a multiparticle time- and position sensitive detector in an ion velocity map imaging experiment based on a double exposure CCD camera in order to determine the (v_x, v_y, t) distribution for all particles simultaneously with a time resolution of about 1 ns. For each collected particle the (x, y, t) data are recorded in a time-resolved event counting (TREC) routine, after which the full 3D kinematics can be retrieved. We illustrate the resolution of the system in an experiment on molecular iodine photodissociated with femtosecond intense Ti:sapphire laser pulses.

2.2 Method

In the experiment, a femtosecond laser is focused on a pulsed molecular iodine beam. The molecular beam is formed by flowing neon through a cell containing solid I_2 and by expanding the mixture through a pulsed valve. The beams are crossed perpendicular to each other in a plane perpendicular to the time-of-flight (TOF) axis of the imaging spectrometer (see Fig.2.1).

The laser is a home built Ti:sapphire CPA (chirp pulse amplification) system operating at 50 Hz and delivering pulses with a 50 fs duration at an 800 nm central wavelength [4].

In the experiments reported in this paper the duration of the pulses was lengthened to 200 fs by applying a chirp to the pulses using the grating compressor. The polarization of the laser is either parallel to the detector surface or perpendicular to it. The ionization area is located inside an electrostatic lens suitable for velocity map imaging. The lens consists of a repeller plate (+5730 V) and two accelerator electrodes: a extractor (+4460 V) and the ground electrode.

In the present experiments, the laser induces a multiphoton Coulomb explosion

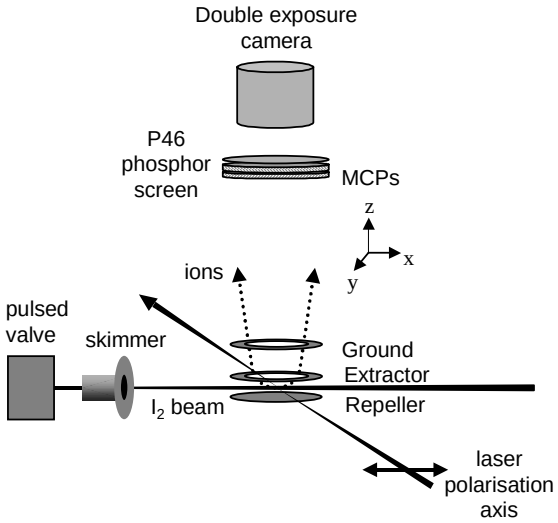

Figure 2.1: *Scheme of the experimental setup. A skimmed pulsed molecular beam of iodine is crossed with an intense femtosecond laser pulse at the centre of a velocity map imaging lens system. The laser polarisation can be chosen either perpendicular to the detector surface (that is in the* $\boldsymbol{z}$*-direction) or parallel to the detector surface (that is in the* $\boldsymbol{x}$ *-direction). The ions are extracted towards a MCP detector (*$\boldsymbol{z}$*-direction), equipped with a P46 phosphor screen. The double exposure camera detects position (*$\boldsymbol{x}$*, and* $\boldsymbol{y}$*-coordinates) and relative arrival time* $\boldsymbol{t}$ *of all particles.*

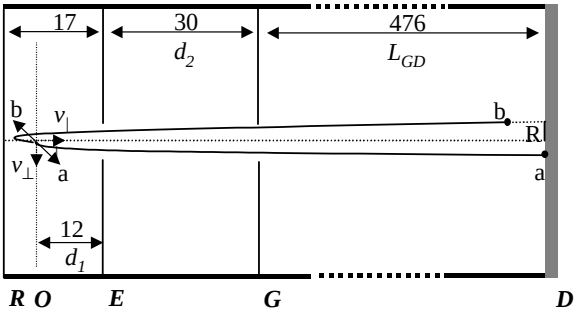

Figure 2.2: *Scheme of the experimental setup relevant for the time-of-flight calculations. Molecules are dissociated at O in the first extraction region defined by the repeller (R) and the extractor (E). EG (ground plate) is the second part of the extraction region. The extraction fields are chosen to meet the velocity map imaging demand. GD is the drift region. Trajectories of two particles '**a**' and '**b**' are sketched. The displacement on the detector (D) is indicated with **R**. The distances are expressed in mm.*

process of the molecular iodine. The molecules are ionized on the rising edge of the laser pulse and a multiple ionization process followed by a Coulomb explosion takes place once the molecular ions start to dissociate and proceed to a critical internuclear distance of approximately 10 a.u. [5]. The resulting ions are extracted into the ion imaging spectrometer (see Fig. 2.2). After extraction, the ions fly through a field-free tube and they arrive at an imaging detector consisting of a double MCP capacitively coupled with a phosphor screen of type P46 ($\phi = 70$ mm, Hamamatsu F2226-24PX). The arrival time of the ions at the detector depends on the m/q ratio, where m is the mass of the ion and q is its charge. Therefore, by gating the detector, specific charged fragments can be selected.

A double exposure CCD camera (LaVision, modified Imager3 VGA) placed behind the phosphor screen records an image of the phosphor screen and the intensities of the spots corresponding to individual ions. Due to the fast interline transfer of the CCD chip, the camera is capable of taking two successive images of the same phosphor decay for each event that originates from a single laser pulse. Subsequently, the arrival time can be found for each event from the ratio of intensities measured in both images [6]. The principle of double exposure CCD camera has been extensively described in the Section 1.5.2. Another point to mention is the synchronization between the CCD camera and the laser. The double exposure camera is designed to work with an internal trigger, synchronized to an internal clock, acting as the master clock for the

experiment. In our setup, the operation of the laser system requires the laser to be the master clock in the experiment, triggering the pulsed molecular beam, the voltage on the MCP and the camera. Unfortunately, perfect synchronization is lost and the response of the camera with respect to the laser trigger jitters (up to 40 ns) from one laser shot to another. Of course, this jitter is transferred directly onto the time information. Our solution was to determine the shift in the timing for each laser pulse and to correct for it. The time-of-flight (TOF) distribution of the ions produced by one laser shot is symmetric around a mean TOF value (the TOF for fragments ejected parallel to the detector or with zero kinetic energy release). It is therefore possible to calculate an *average* TOF and to express for each particle the arrival time with respect to this new reference. This method introduces a statistical error in the timing as described below. Alternatively, we have tried to calibrate the times-of-flight of the particles by explicitly measuring the arrival of the laser at the apparatus using a photodiode where the detection electronics was triggered by the camera. In this way the jitter between the firing of the laser and the switching of the camera is quantified. Unfortunately, we have thus far not been able to improve the calibration of the jitter using this method, possibly due to small, shot-to-shot variations in the times-of-flight of the ions.

The experiment reconstructs the recoil velocities from the arrival time and the position coordinates of the fragments on the detector. In Fig. 2.2 we assume that the particles a and b are ejected with the same energy but in opposite directions. Whereas particle a arrives after a time-of-flight of $t^a_{tot} = t_{OE} + t_{EG} + t_{GD}$ particle b, ejected backwards, travels longer $t^{tot}_b = t_{turning} + t_{OE} + t_{EG} + t_{GD}$. The arrival time-of-flight difference equals the turn around time in the extraction field. We assume flat electric fields inside all electrostatic lenses. Then, the turn around time is $t_{turning} = 2v_{\parallel}/a_1$, with a_1, the acceleration of the ion between repeller and extractor and $v_{\parallel} = v\cos(\alpha)$, the projection of the velocity on the detector axis, z. In this approximation (see Fig. 2.2) the intermediate time t_{OE} is :

$$t_{OE} = \frac{(2a_1d_1)^{\frac{1}{2}}}{a_1} - \frac{1}{a_1}|v_{\parallel}| + \frac{1}{2a_1(2a_1d_1)^{\frac{1}{2}}}v^2_{\parallel}, \tag{2.1}$$

At the position 'E' in Fig. 2.2 the velocity is nearly independent of the parallel component of the recoil velocity. Hence, the effect of $v_{\parallel}$ on the total time-of-flight from E to D (the detector) can be neglected. For a kinetic energy of 1 eV the maximum contribution of the $v^2_{\parallel}$ term is 0.4 ns for I^+ and 0.14 ns for I^{2+} (values that represent less than 2% of the total time difference). For simplicity we chose to neglect this contribution in the last term of Eq. (2.1). This time-of-flight is approximately equal to:

$$t_{tot} = t_{av} - \frac{1}{a_1}\cos(\alpha)v, \tag{2.2}$$

where t_{av} is the time-of-flight for particles in a plane parallel to the detector ($\alpha = 90°$), α is the ejection angle with respect to the lens axis and v is the velocity corresponding to the kinetic energy released in the process. In this approximation the time distribution is symmetrical around t_{av}. The velocity v can now be expressed in the observed parameters:

$$v = \sqrt{\frac{R^2}{t_{tot}^2} + a_1^2 * \Delta t^2}, \tag{2.3}$$

where $R = c * R_m$, R_m is the measured distance on the detector between the position of the fragment and the centre of the image, c is the calibration constant of the apparatus and of the velocity imaging technique and $\Delta t = t_{tot} - t_{av}$. The camera provides the position (x, y) and arrival time t_{tot} of the particles. The center of the image (x_c, y_c) and t_{av} have to be determined.

The angle α follows from:

$$\alpha = arc\tan(\frac{R}{t_{tot}} * \frac{1}{a_1 \Delta t}) \tag{2.4}$$

In the next paragraphs we discuss how the experimental conditions, computational method and physical process itself affect the time resolution.

In the absence of an extraction field, for a single value of the kinetic energy release, the fragments lie on an expanding sphere and the relative velocity between the two fragments is conserved. In the electrostatic field, the ions are accelerated and the relative velocity between the fragments along the field direction decreases in time; one could say that, both in velocity space and in real space, the electric field deforms the sphere into a pancake. This squeezing results in a reduction of the time difference between the arrival of the two fragments at the detector.

In the approximation of flat electric fields the pancaking squeezes only the timing and it has no effect on the distance between particles in the plane of the detector. The maximum time-of-flight difference, Δt, in this approximation is equal to the turning time for a fragment ejected backward, against the electric field. The time range could therefore be increased by decreasing the acceleration in the repeller-extractor region (see Eq. (2.2)). One should be aware that the acceleration cannot be changed arbitrarily because modifications of the electric fields affect the focusing properties of the lens and the detection efficiency of the MCPs.

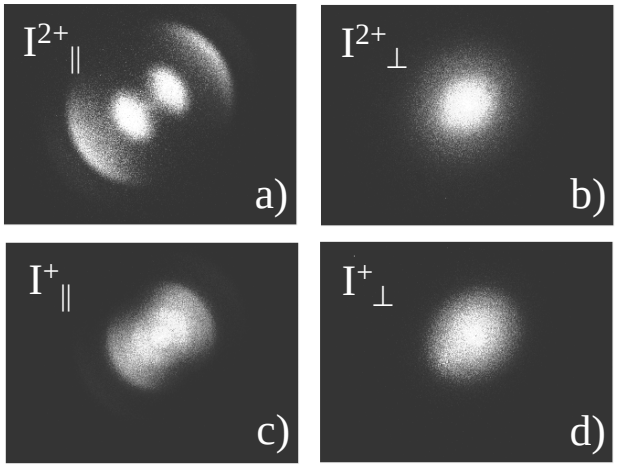

Figure 2.3: *Experimental images recorded using femtosecond dissociative ionisation of molecular iodine. The four situations shown are* (*a*) I^{2+}*, polarisation parallel;* (*b*) I^{2+}*, polarisation perpendicular;* (*c*) I^{+}*, polarisation parallel;* (*d*) I^{+}*, polarisation perpendicular.*

2.3 Results

2.3.1 Experimental results

The products of the multiphoton Coulomb explosion process are neutrals and singly and multicharged iodine ions. As described, the detector is gated in time which enables the detection of individual charges and masses. For the purpose of illustrating the potential of the 3D detector, we detect I^{+} and I^{2+} fragments for two different orientations of the laser polarization. A parallel image refers to the situation when the laser polarization is parallel to the detector surface. A perpendicular image corresponds to the laser polarization being perpendicular to the detector surface. In traditional 2D ion imaging techniques only parallel images are recorded, such that the dynamical information is fully revealed in the xy plane. In the perpendicular configuration a large part of the dynamical information is encoded in the arrival time of the particles on the detector. For practical reasons, the orientation of the camera is chosen such that laser polarization makes an angle of 45 degree with the xy- grid.

Figure 2.3 shows four images corresponding to two different orientations of the laser polarization for the detection of I^{+} and I^{2+}. Images a and c show results for detection of $I^{2+}$and I^{+} in the parallel configuration, whereas images b and d show

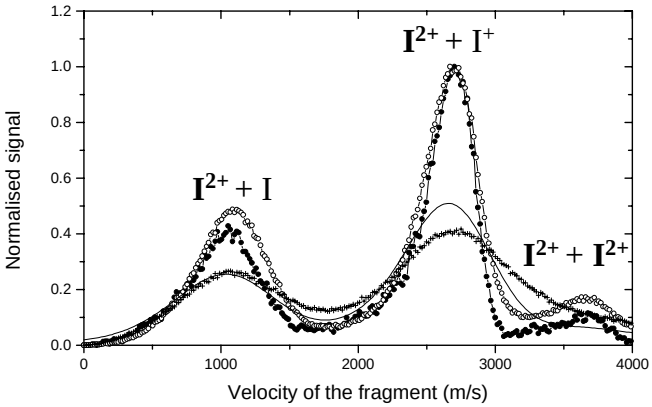

Figure 2.4: I^{2+} *fragment velocity distributions from the data in Figs. 2.3a and 2.3b. (∘) polarisation parallel, using* ***(x,y,t)*** *data; (•) iterative inversion using* ***(x,y)*** *data; (+) perpendicular polarisation, using* ***(x,y,t)*** *data; (-) velocity distribution obtained from convoluting the iterative inversion results with the time resolution to simulate the results obtained in the perpendicular configuration.*

results for detection of $I^{2+}$and I^{+} in the perpendicular configuration. In the experiments with the laser polarization parallel to the detector several velocity classes can be deduced from the appearance of structures with different diameters, whereas no such information is apparent in the images taken in the perpendicular configuration. We note that images a, c and d contain events produced in 2000 laser shots of maximum 400 particles each, whereas image b is integrated over 4000 laser shots of maximum 300 particles each.

In these experiments, dissociation follows the removal of several electrons by the intense laser field. In the following we present the velocity distributions of the fragments determined on the basis of images $2.3a - d$ (with the associated arrival time measurements). In Figure 2.4 a comparison is presented between the velocity distributions which can be obtained from Fig. 2.3a and Fig. 2.3b. The velocity distribution reveals the presence of three Coulomb induced dissociation channels, where the I^{2+} ion which is measured is formed along with an I atom or an I^{+} or I^{2+} ion, respectively. The first velocity peak corresponds to a charge-asymmetric fragmentation $(I^{2+} + I)$ [5, 7], the second peak to a dissociation channel where the undetected ion

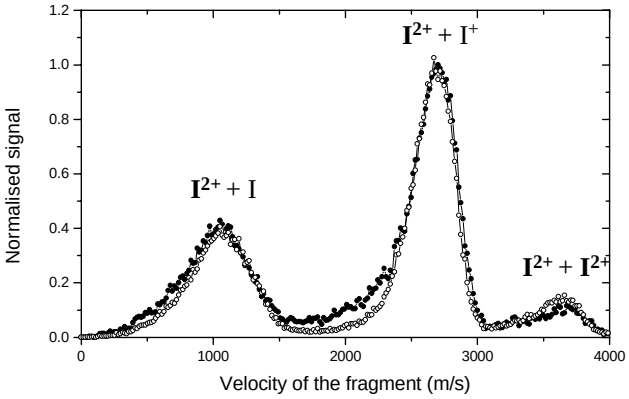

Figure 2.5: *I^{2+} fragment velocity distributions from the data in Fig. 2.3a. (○) polarisation parallel, using (**x,y,t**)-data and a selection of events $80^o < a < 90^o$ such that the arrival time difference is very small; (●) iterative inversion using (**x,y**)-data.*

is I^+ ($I^{2+} + I^+$) and the small peak at higher velocity to a channel where the other fragment ion is also I^{2+} ($I^{2+} + I^{2+}$). The Coulomb interaction dominates the dissociation process, therefore highly charged ions appear at higher fragment velocity. The broad energy distribution is due to the range of internuclear distances over which the ionization step can occur.

The experimental data shown in Fig. 2.3*a* can be treated in two different ways, (i) by calculating the velocity distribution from the (x, y, t) data or (ii) by means of a mathematical inversion of the 2D image [8]. Method (ii) is the traditional method to obtain the velocity distribution in an imaging experiment, and, apart from deficiencies which can occur in measurements due to problems like counting noise and/or detector inhomogeneities, gives a benchmark result that we can test the quality of our 3D measurement against. Figure 2.4 shows that the calculated velocity distribution from the (x, y, t) data of Fig. 2.3*a* agrees satisfactorily with the velocity distribution obtained by iterative inversion of the same data, ignoring the time information. The positions and the widths of the dominant features in the velocity distribution are clearly reproduced, and the only difference is a slight loss in resolution in the 3D method due to the finite precision of the arrival time measurement.

The velocity distribution for the data of Fig. 2.3*b* can only be calculated from

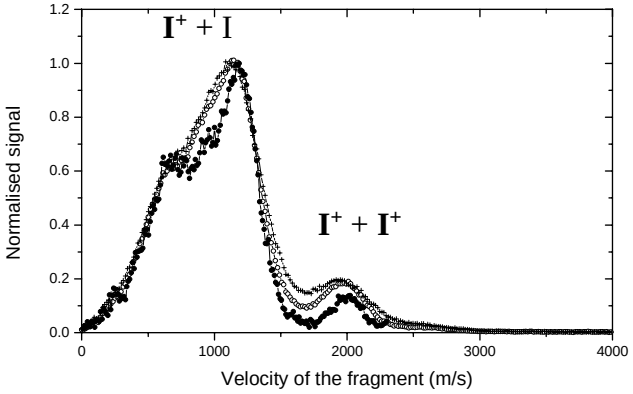

Figure 2.6: *I^+ fragment velocity distributions from the data in Figs. 2.3c and 2.3d. (∘) polarisation parallel, using (**x,y,t**) data; (•) iterative inversion using (**x,y**) data; (+) perpendicular polarisation, using (**x,y,t**) data.*

the (x, y, t) data. Figure 2.3*b* does not contain distinguishable dissociation channels. Figure 2.4 clearly shows that the velocity distribution does contain at least two distinguishable velocity structures. At the same time it is clear that for this set of data the peaks in the velocity distribution are clearly broader. This broadening is due to fact that the velocity distribution is predominantly encoded in the arrival time distribution of the ions, which is measured with a precision $\delta t/t$ which is inferior to the precision $\delta x/x$ of the spatial measurements. We simulated the last result by taking the iterative inversion curve to be the "true" velocity distribution and by assuming a Gaussian distribution error in the timing with $\sigma = 1.7$ ns. The result is shown as the solid curve in Fig. 2.4. This simulation is very satisfactorily. Clearly, the quality of this result could be improved by reducing the extraction field strengths, which increases the width of the arrival time distribution.

The importance of the arrival time measurement is revealed in Fig. 2.5, where the velocity distribution obtained by mathematical inversion is compared to a velocity distribution which is obtained from the 3D method, based on selection of events around the "*average*" time-of-flight $t_{tot} = t_{av}$. In practice an angular slice with $80^o < |\alpha| \leqslant 90^o$ was selected. In this case, the comparison suggests that the results based on the 3D method have a resolution which is slightly better than the results from the iterative procedure. We note that an analogous selection based on the application of

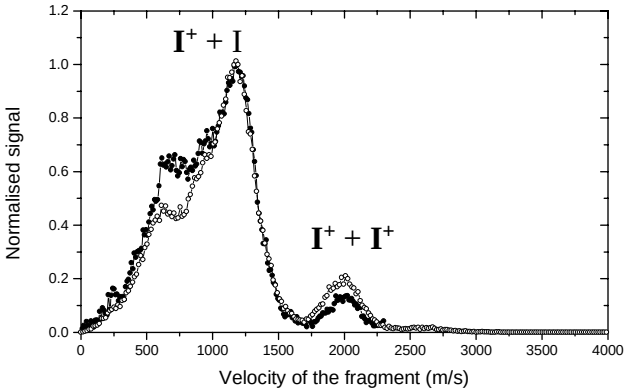

Figure 2.7: *I^+ fragment velocity distributions from the data in Fig. 2.3c. (∘) polarisation parallel, using (**x,y,t**) data using a selection of events $80° < a < 90°$ such that the arrival time difference is very small; (·) iterative inversion using (**x,y**) data.*

a time slice was used by Gebhardt et al. [9].

In Figures 2.6 and 2.7 results of the measurements detecting I^+ ions are shown (Figures 2.3*c* and 2.3*d*). As one can see from Figs 2.3*a* and 2.3*c*, in case of I^+ ions the velocity distribution shows less structure. Similar to Fig. 2.4, Figure 2.6 shows the results obtained by the 3D method, in both the parallel and perpendicular configuration. The agreement with the results of the mathematical inversion of the parallel data of Fig. 2.3*c* is very good. The time resolution derived from the experimental data is 1.2 ns (standard deviation). As was the case for the I^{2+}results discussed before, both measurement techniques reveal the same information about the product channels in the experiment, namely the formation of I^+ in combination with either I atoms or I^+ ions. In the $I^+ + I$ channel, the velocity distribution is not single-peaked, but contains at least two contributions. The $I^+ + I^{2+}$ channel, which was very prominent in the I^{2+} measurements, is missing in Fig. 2.6, since the experiment was performed at a slightly lower laser intensity, in order to limit the count rate to a level where individual ions can be distinguished on the camera. The velocity distribution obtained by mathematical inversion of the 2D data is slightly better than the results obtained by the 3D methods.

As Figure 2.7 shows, extraction of an angular slice from the data solves the problem

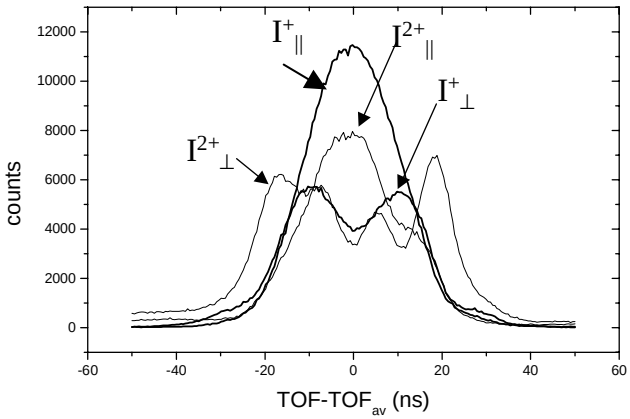

Figure 2.8: *The measured arrival time distributions for the experiments shown in Figs. 2.3(a)-2.3(d). The average time-of-flight time (*$\mathbf{TOF}_{av}$*) is determined for each laser shot independently. The labels at the curves refer to the charged state of the ion and the experimental configuration;* $I_{\parallel}^{2+}$*- Fig 2.3(a);* $I_{\perp}^{2+}$*- Fig 2.3(b);* $I_{\parallel}^{+}$*- Fig 2.3(c);* $I_{\perp}^{+}$*- Fig 2.3(d).*

of the loss of resolution in the parallel configuration and yields a velocity distribution with a resolution very similar to the mathematical inversion, comparable to the results for I^{2+} in Fig. 2.5. At small fragment velocities, Fig. 2.7 shows some differences in the relative magnitude of the different fragment channels. The resolution of the angular distribution in the 3D method depends on the accuracy of the observed timing. At high velocities the angular distribution gives the "real" angular distribution, whereas at lower velocity more and more events move out of the angular selection window due to the uncertainty in the flight-time.

In Figure 2.8 a summary is given of the arrival time distributions of the I^{+} and I^{2+} fragments in both the parallel and the perpendicular configurations. The quality of the arrival time determination with the double exposure camera is such that even without use of the position information the different fragment channels can already be distinguished in the perpendicular configuration. The asymmetry (more pronounced for the I^{2+} perpendicular configuration) is due to background. Figure 2.8 provides strong support for the discussion of the resolution in the velocity distribution in the different cases discussed above.

The resolution in the velocity distribution depends on the quality in the timing and in the position. In the present set up, the relative accuracy in the timing is worse than the relative accuracy in the position determination. The anisotropy of the

photofragment process makes it often possible to optimize the resolution in the imaging technique. For example, in those cases where the position resolution exceeds the accuracy in the timing, the laser polarization can be chosen parallel to the detector. The results shown above indicate that the relative timing resolution depends on the timing range, which depends on the strength of the extraction field, on the kinetic energy release and on the charge of the detected fragments. As will be described in the next section, the timing resolution in our present experiments also depends on the accuracy of the determination of the t_{av}. In the next section, the position and the time resolution will be analyzed.

2.3.2 Computational results

As explained above in Eq. (2.3), calculation of the kinetic energy release requires the determination of the centre-of-mass coordinates and the *average* time-of-flight value, t_{av}.

The position of the centre-of-mass of the image is fixed during the experiment and it can be estimated from the average 2D image with good accuracy. In our experiment, the *average* time, t_{av} can differ up to 40 ns from one laser shot to another . This is due to the internal jitter in the response of the camera when triggered externally. In order to correct for this jitter we determine t_{av} for each laser shot separately, by averaging the arrival time of the particles. Since in one laser shot we detect no more than 400 particles, the t_{av} determination is affected by statistical errors. We estimated this error by performing a numerical simulation using the distributions of the number of particles per laser shot (see Table I) in the different cases and the observed arrival time distribution of fragments (see Fig. 2.8). For each case, we simulated 2000 laser shots. For each simulated laser shot, a t_{av}^{sim} is calculated by averaging the arrival time of the simulated events. The resulting distribution of t_{av}^{sim} approximates a Gaussian with a standard deviation σ_{stat}. The values for each configuration are given in Table I. This statistical error can be decreased by averaging over a higher number of particles, but one should be aware that the number of particles per laser shot is limited by the resolving power of the camera.

The values of σ_{stat} depend both on the number of particles detected and on the experimental arrival time distributions. The smallest value of σ_{stat} is obtained for I^+ in the parallel configuration, where the spread of the arrival times is relatively small (see Fig. 2.8), and where the number of particles detected was described by a relatively narrow distribution around $\overline{N} = 300$ (see Table I). By comparison, measurements of I^{2+} in the parallel configuration - with an arrival time distribution with a comparable width - gave a larger value of σ_{stat} because the distribution of the number of particles was significantly broader, with a maximum appearing at $\overline{N} = 225$. When using I^{2+} in the perpendicular configuration the determination of σ_{stat} suffered not only from the low number of counts per image but also from the large spread in the arrival times of the ions.

Table I. The relevant parameters for the time resolution of the system.

	$I_{\parallel}^{2+}$	$I_{\perp}^{2+}$	$I_{\parallel}^{+}$	$I_{\perp}^{+}$
$\overline{N}$	225	140	300	215
ΔN	220	125	80	50
$\sigma_{stat.}$	0.73	1.27	0.52	0.82
$\sigma_{total}^{calc.}$	1.27	1.64	1.16	1.33
$\sigma_{total}^{exp.}$		1.7		1.2

$\overline{N}$ - the mean value of number of particles detected for each laser shot in one experiment;

ΔN - the FWHM of the histogram of number of particles detected for each laser shot in one experiment;

$\sigma_{stat.}$ (ns) - the calculated statistical time error in determination of t_{av};

$\sigma_{total}^{calc.}$ - the calculated time error in the experiments;

$\sigma_{total}^{exp.}$ - the experimental time error.

The dependence of σ_{stat} on the number of particles and the arrival time distribution is further illustrated in Fig.2.9. Four curves are shown that represent the expected σ_{stat} for the cases under consideration (I^+ and I^{2+} in the parallel and the perpendicular configuration), as a function of the number of particles in each laser shot, in a simulation where the number of particles was held constant for each laser shot. The I^+ and I^{2+} measurements in the parallel configuration yield by far the best results, in agreement with the fact that these cases have the narrowest arrival time distribution.

The statistical error σ_{stat} dominates over all other timing errors in the experiments. In principle, it can be avoided by using the camera in a synchronized mode where the camera acts as the masterclock of the experiment. In this way there is no jitter in the response of the camera and the t_{av} can be determined by averaging the arrival time for all the particles for all laser shots together. This method requires very stable operation of the ion lenses, otherwise fluctuations in the time-of-flight of the fragments will lower the resolution of the timing.

Other sources of error are also present. Trajectory calculations reveal that the size of the interaction region (1x1x0.03 mm^3, with the 0.3 mm in the z direction) causes a time error with a standard deviation less than 0.3 ns. The error is dominated by the width of the interaction region in the z direction, along the lens axis. The 1 mm size of the interaction region in the xy plane causes a negligible time error with a standard deviation smaller than 0.08 ns.

The effective time error, $\sigma_{total}^{exp.}$, can also be calculated from the experimental data using the perpendicular configuration and considering the Iterative Inversion velocity

distribution as "the true" velocity distribution. The values for $\sigma_{total}^{exp.}$ are given in Table I. It shows that the experimentally determined values for $\sigma_{total}^{exp.}$ agree well with the estimated time errors $\sigma_{total}^{calc.}$.

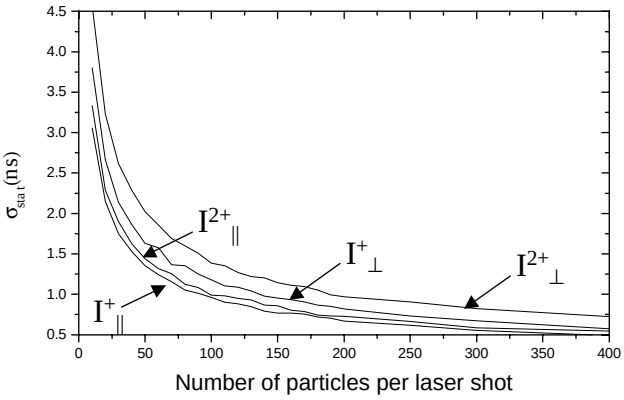

Figure 2.9: *Standard deviation in the determination of* $\mathbf{t}_{av}$ *as a function of the number of particles per laser shot. The curves refer to the four experimental configurations, which provide differently shaped time distributions.*

In conclusion, we have presented the use of a multiparticle time- and position sensitive detector in an ion velocity map imaging experiment. We have illustrated the resolution of the system (1.3 ns) in an experiment on molecular iodine photodissociated with femtosecond intense Ti:sapphire laser pulses. The detector is based on a double exposure CCD camera which retrieves for each collected particle the (x, y, t) information. The timing accuracy and dynamic range are determined by the decay time of the phosphor. In the present experiments, we estimate the dynamic range to be about 100 ns. Using different phosphors, the dynamic range can be changed. The results reveal that a good agreement can be found between the fragment velocity distributions obtained by a mathematical inversion procedure of 2D (x, y) data and the velocity distributions which are directly obtained in the 3D measurement, and illustrate that it will be possible to use the 3D method in situations where the mathematical inversion of 2D data is no longer applicable.

Bibliography

[1] D. W. Chandler, P. L. Houston, J. Chem. Phys. **87**, 1445 (1987)

[2] A. J. R. Heck, D. W. Chandler, Annu. Rev. Phys. Chem. **46**, 335 (1995)

[3] A. T. J. B. Eppink , D. H. Parker, Rev. Sci. Instrum. **68**, 3477 (1997)

[4] F. Rosca-Pruna, E. M. Springate, H. L. Offerhaus, M. Krishnamurty, C. Nicole, M. J. J. Vrakking , J. Phys. B **34,** 4919 (2001)

[5] J. H. Posthumus, A. J. Giles, M. R. Thompson, W. Shaikh, A. J. Langley, L. J. Frasinski and K. Codling, J. Phys. B: At. Mol. Opt. Phys. **29,** L525 (1996)

[6] R.Bobbenkamp, Ph.D. Thesis, Bielefeld, 2002

[7] J. H. Posthumus, J. Plumridge, M. K. Thomas, K. Codling, L. J. Frasinski, A. J. Langley and P. F. Taday, J. Phys. B: At. Mol. Opt. Phys. **31,** L553 (1998)

[8] M. J. J. Vrakking, Rev. Sci. Instrum. **72,** 4090 (2001)

[9] C. R. Gebhardt, T. P. Rakitzis, P. C. Samartzis, V. Ladopoulos and T. Kitsopoulos, Rev. Sci. Instrum. **72**, 3848 (2001)

Chapter 3

Photodestruction of NO_2^-

We present an experiment on the photodestruction of the NO_2^- anion at 266 nm. We have quantified the competition between photodetachment and photodissociation and have identified the nature of the photodissociation process from the photofragment angular distribution. This study involves a novel technique; time resolved multico-incident detection photofragment spectroscopy. A three dimensional double exposure CCD camera is employed. The system provides the position (x, y) and the relative arrival time (t) of all fragments. In the case of photodissociation events, NO and O^- fragments are detected for each event. The detection of multiple events per laser shot is made possible by using centre-of-mass selection.

3.1 Introduction

The photodestruction of molecular anions has not been studied in detail because of experimental difficulties. Photodestruction is the sum of two competing processes: photodetachment and photodissociation. With sufficiently energetic photons, or in weakly bound systems, also dissociative photodetachment is possible [1, 2]. By using the same MCP detector for the detection of all molecular products, i.e., fragments from photodissociation as well as neutral molecular products from photodetachment, absolute branching ratios can be determined. The branching between the different processes is important under many conditions in very dilute plasmas, such as our own atmosphere. The products of photodetachment, free electrons and neutrals have different reactivity and affect the plasma in a very different way than the photodissociation products. The photodestruction of NO_2^- plays a role as intermediate in the chemistry of the D-region of the ionosphere [3].

Nitrogen dioxide has a very large electron affinity $EA \sim$ 2.275 eV [4]. The anion and the neutral molecule have similar $N - O$ internuclear separations (1.15 Å for NO_2^- and 1.19 Å for NO_2) [4]. The attached electron induces a small bond-length contraction. The bond angle for the ground state NO_2^- ($X\ ^1A_1$), $\theta = 117.5°$ is smaller than the bond angle of the neutral ground state $\theta = 135.1°$ [5]. The dissociation energy is $\sim$ 4 eV [6], which is more than that of the neutral parent molecule by about 0.8 eV. Most experiments have concentrated on the photodetachment channel for this anion. When photodestruction was studied, no distinction was made between photodissociation and photodetachment. A number of experiments have concentrated on the existence of possible peroxide isomers with energies close to that of the anion ground state. Here, we determine for the first time the competition between the two destruction channels at a photon energy where both pathways are fully open. Moreover, we provide kinetic energy release distribution and photofragment anisotropy information for the photodissociation channel.

3.2 Method

The nitrogen dioxide anion, NO_2^- is produced in a hollow cathode discharge ion source filled with O_2 and N_2 gas in proportions of 5:1. The discharge is maintained at 600 V and 20 mA. The negative species are extracted at 5 kV and the NO_2^- ions are mass selected by a Wien filter. The continuous molecular ion beam of NO_2^- is introduced into a fast beam setup (see Fig. 3.1). By means of four deflection plates the beam is guided through the apertures of the apparatus. Two Einzel lenses are used to focus the beam through the exit aperture of the ion source region and to reduce the radial size of the beam in the region of interaction with the laser. The NO_2^- anion beam is intersected at 90 degrees by ultraviolet laser radiation. The laser system used for this experiment was a 50 Hz Spectra Physics Nd-YAG laser. The 532 nm output of the

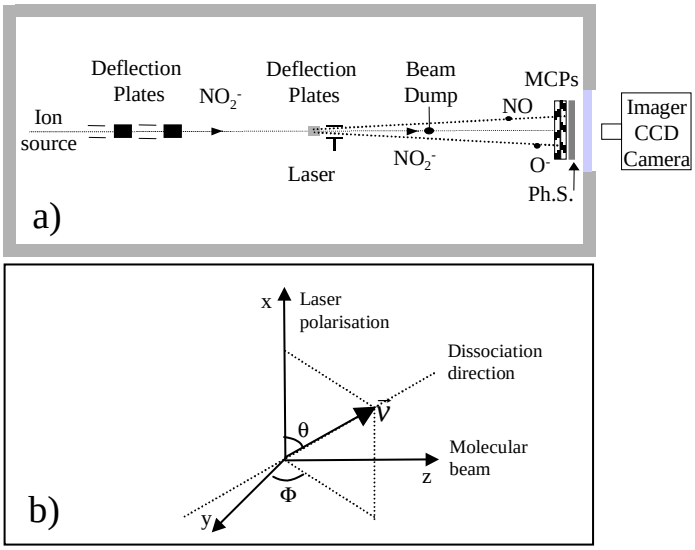

Figure 3.1: *a) Scheme of the experimental setup. A continuous molecular ion beam of NO_2^- is crossed with a 25 Hz laser pulse (266 nm). Photodissociation and photodetachment occur leading to NO_2, NO and O^- fragments. The use of the beam dump is optional as well as the use of deflection plates after the laser interaction region. The Imager CCD camera measures the position (x, y) and the arrival time t of the fragments on the detector. b) Schematic of the dissociation process.*

Nd-YAG laser is frequency doubled in a BBO non-linear crystal and the energy of the UV laser pulse, measured after the interaction region is ~ 10 mJ. The polarization of the laser is chosen parallel to the detector surface, along the y axis (see Fig. 3.1). The two processes we investigate are photodetachment and photodissociation of NO_2^-.

$$NO_2^- + h\nu \rightarrow NO_2 + e^-, \tag{3.1}$$
$$\rightarrow NO + O^-. \tag{3.2}$$

The photodetachment signal consists of neutral NO_2 molecules flying in the same direction as the initial NO_2^- beam. The photodissociation signal, on the other hand,

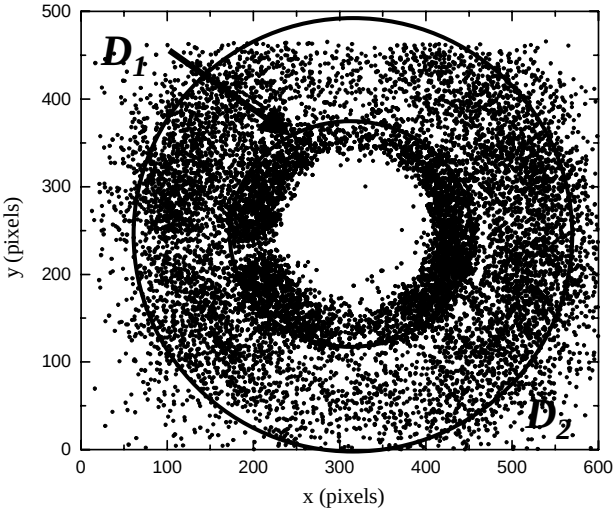

Figure 3.2: *Photodissociation signal of NO_2^- at 266 nm. The two rings D_1 and D_2 indicate the presence of two different masses. The ratio D_2/D_1 is 1.85, a value in good agreement with a mass ratio of 30/16. The central arrow shows the direction of the laser polarization.*

consists of NO and O^- fragments flying away from the parent beam direction with velocities related to the kinetic energy released in the dissociation process. Other possible dissociation channels such as $N + O_2^-$ are energetically closed. After a time-of-flight of ~ 8.47 μs the fragments reach the detector consisting of two microchannelplates (MCPs) and a P46 phosphor screen. For a good signal-to-noise ratio, the detector is gated with respect to the firing of the laser. The voltage on the front of the MCP is raised to the optimum value (2 kV difference over the MCP stack) when the laser induced fragments are expected to arrive. The detection gate is open for 400 ns. Between laser shots, the voltage on the front of the MCP is decreased by 800 V to a value that does not permit particle detection.

Outside the vacuum system a so-called three-dimensional (3D) double exposure CCD camera (LaVision, modified Imager3 VGA) records images of the phosphor screen. The principle of the 3D camera is described in detail elsewhere [7,8]. In brief, the camera records the image of the phosphor screen and the intensity of the spots corresponding to individual particles. Due to the fast interline transfer of the CCD

chip, the camera is capable of taking two successive images of the same phosphor decay for each single laser pulse. Subsequently, the arrival time can be found for each particle from the ratio of intensities measured in both images [9]. The detection system retrieves the (x, y) coordinates of the spots with $\sim$ 80 μm resolution and the arrival time of the particles with $\sim$ 1 ns resolution. This information is used to reconstruct the orientation of the molecule at the moment of dissociation and to calculate the kinetic energy released in the process.

$$KER = \frac{E_0}{L^2}\frac{m_1 m_2}{(m_1+m_2)^2}(D^2 + v_0^2\Delta t^2)(1 + 2\frac{m_1 - m_2}{m_1 + m_2}\frac{v_0\Delta t}{L}), \quad (3.3)$$

$$\theta = \arctan\frac{\sqrt{(\Delta y)^2 + (v_0\Delta t)^2}}{\Delta x}, \Phi = \arctan\frac{v_0\Delta t}{\Delta y}. \quad (3.4)$$

where m_1 and m_2 are the masses of the two fragments NO and O^-, D is the distance between them on the detector , Δt is the arrival time difference of the fragments, $L = 1.25$ m is the distance between the reaction region and the detector, E_0 is the kinetic energy of the fast beam (5 keV), and v_0 is the translational velocity of the NO_2^- anions ($\sim 1.5 * 10^5$ m/s). The angle θ is defined with respect to the laser polarization axis (see Fig. 3.1b).

The camera provides the master clock of the experiment and it controls the firing of the laser and the gating of the MCPs. The acquisition rate is limited by the camera to 25 Hz.

3.2.1 Multicoincident detection

This detection system providing (x, y, t) coordinates of the particles allows detection of multiple dissociation events. The data is taken and analyzed for each laser shot separately. The maximum number of fragments detected per laser shot is in principle only limited by the finite resolution of the camera chip, 640x480 pixels and the size of the spots, 3x3 pixels. In case of a coincident measurement, when the fragments must be correlated as coming from the same parent molecule, the maximum number of particles that can be resolved depends strongly on the experimental conditions, namely the size of the parent molecular beam.

The correlation is performed by centre-of-mass selection. In the case of a homonuclear diatomic molecule, the two fragments have identical mass and the centre-of-mass calculation is straightforward. The calculation is performed for each combination of two particles. Only those pairs having their centre-of-mass inside a confined region defined by the size of the parent beam are considered true coincidences. In principle, the narrower the molecular beam is, the higher is the number of dissociation events that can be resolved. In this particular experiment where the fragments have different mass (30 amu and 16 amu) the nature of the fragments must be identified prior to centre-of-mass calculation.

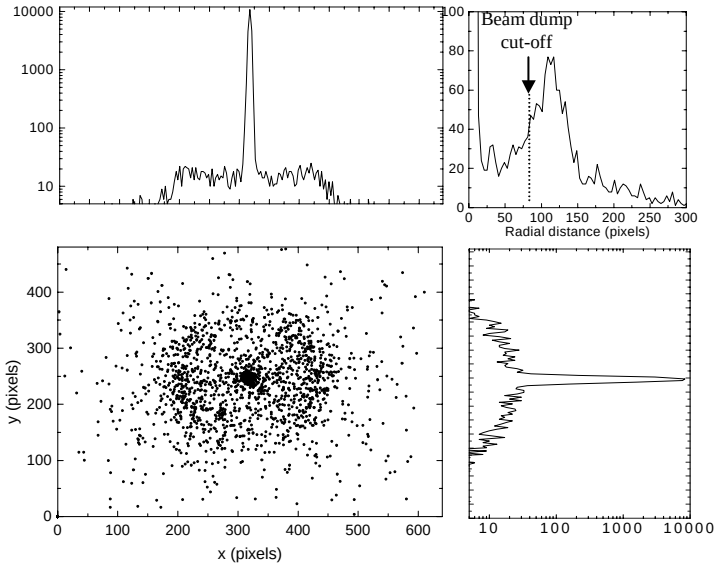

Figure 3.3: *Photodestruction signal of NO_2^- at 266 nm. Only the neutral fragments are detected. The central peak represents NO_2 photodetachment signal while the rest of the counts, distributed around the central peak are NO fragments from photodissociation. From the x and y histograms, the branching between the two processes can be determined. The upper right plot shows the estimated radial distribution of the neutral NO calculated with respect to the center of the parent beam.*

During a coincident measurement, we can detect all photodissociation products, neutrals and ions. For each laser shot up to 10 fragments are recorded. This number is determined by experimental conditions (molecular beam intensity, laser intensity).

We avoided the use of any electric field after the interaction with the laser such that the negatively charged fragments can travel undisturbed towards the detector. We placed a circular beam dump (ϕ = 1 mm) after the laser interaction region to stop the parent beam, which otherwise would saturate the detector in the central region. We detect only fragments resulting from photodissociation processes which have enough kinetic energy ($>$ 0.5 eV) and a sufficient velocity component in the (x, y) plane to escape the beam dump. The raw (x, y) data, as it is recorded by the camera over 180 000 laser shots at a photon energy of 4.66 eV is shown in Fig. 3.2. In the middle of the detector there are no counts due to the presence of the beam dump. Around the shadow of the beam dump, two main rings can be distinguished,

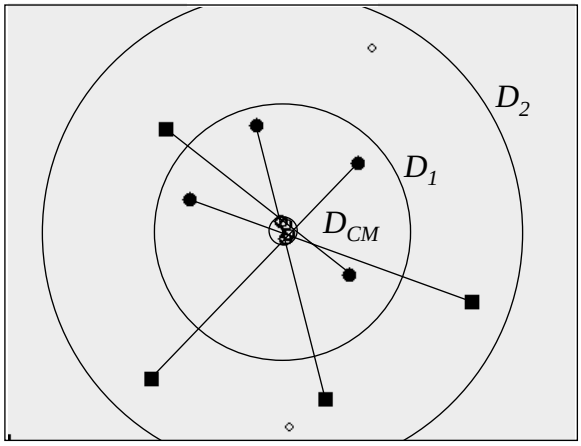

Figure 3.4: *Sample of the images taken during laser shots. 10 fragments are detected; from their position we identify the nature of each fragment: NO (•) and O^- (■). For each pair of NO and O^- the centre of mass is calculated. We plot only those centre of mass that lie inside the inner ring D_{CM}. Uncorrelated fragments are represented by (∘).*

the outer limit being shown by the two circles D_1 ($\phi = 300$ pixels) and D_2 ($\phi = 560$ pixels) . The fragments detected inside the D_1 circle are mostly fragments having the high mass (NO fragments), while those detected outside this ring must have a lighter mass (O fragments).

We can also determine which one of the fragments carries the charge. For this purpose, we have applied an electric field after the laser interaction region to assure that the only fragments that reach the detector are neutral species. We do not use any beam dump since the ionic parent beam is also deflected. The raw (x, y) data integrated over 30 000 laser shots at a photon energy of 4.66 eV is shown in Fig. 3.3. The histograms of particles coordinates show a narrow strong peak in the middle of the image, corresponding to the NO_2 photodetachment signal. The size of the peak, $\phi \simeq 30$ pixels, indicates the size of the parent beam on the detector D_{CM} ($\phi \simeq 3$ mm). Most of the fragments resulting from a dissociation process and having a velocity component in the plane of the detector are confined inside the ring D_1.

From the size of the ring it is clear that neutral fragment has a higher mass than

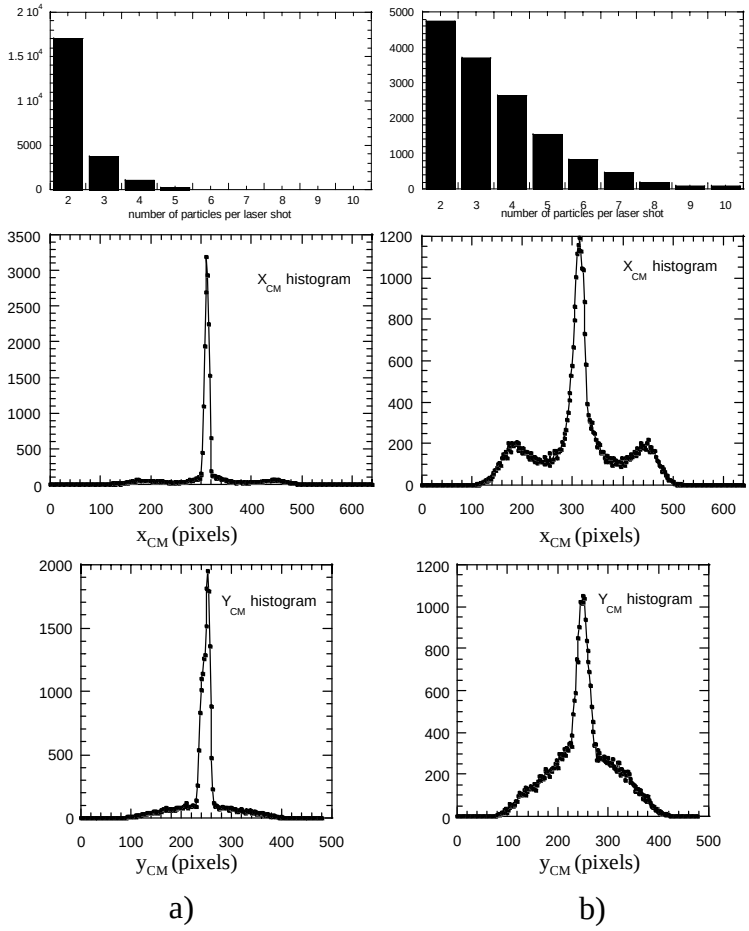

Figure 3.5: *Centre-of-mass determination for two different data sets: a) low ion beam intensity; b) high ion beam intensity. The position histograms of the centre-of-mass for each combination of NO and O^- particles are shown. The fragments resulting from the same molecule appear in the central peaks.*

the ionic fragment. We conclude that the charge is taken by the oxygen fragment and we identify the photodissociation products as NO and O^- fragments. For a coincidence measurement we analyze the images taken at each laser shot separately. Figure 3.4 is a selected example of an image taken during a single laser shot.

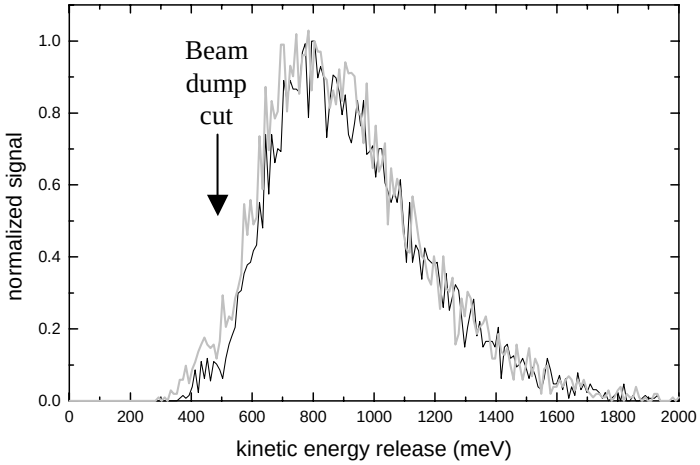

Figure 3.6: *Kinetic energy release spectrum. No significant difference can be observed by analyzing separately laser shots with maximum 2 particles detected (black curve) and laser shots contributing with more than 8 particles (grey curve).*

Ten particles are detected in this image. From the (x, y) position of the fragments we assign them as being NO, if they lie inside D_1 ring, or as O^- fragments if they are found in between the D_1 ring and the D_2 ring. Once the mass of the fragment is know, we calculate the centre-of-mass position for every pair of NO and O^-. If the centre-of-mass lies inside the D_{CM} ring, the pair is a true coincidence and their centre-of-mass is plotted. Out of ten fragments detected, eight were successfully correlated, while two of them were not. The two uncorrelated fragments are very likely to originate from a dissociation event of which the other fragment has not been detected. It is important to stress here that since the detection efficiency of the MCPs is $\sim 50\%$, only in 25% of the cases both fragments are detected. In two-body break-up studies, the possibility to detect unlimited number of particles increases the detection rate considerably.

In Fig. 3.5 we present the center-of-mass distributions for two data sets taken at very different count rates, one corresponding to a low molecular beam intensity and another one corresponding to a high molecular beam intensity. The data has been taken in coincidence by allowing all fragments, ions and neutrals to reach the detector (similar to the data presented in Fig. 3.2) while blocking the central beam with the flag. From the histogram of number of particles detected per laser shot, the low count rate data set (see Fig. 3.5 *a*) is characterized by a detection of mostly 2 particles per laser shot while for the high count rate data set (see Fig. 3.5 *b*) up to 10 particles are detected. The mass of each fragment is identified and the centre-of-mass position for all combinations of NO and O^- fragments are calculated. The results are plotted in x_{CM} and y_{CM} histograms. The central peaks are a direct measure of the size of the molecular parent beam at the detector. In Fig. 3.5 *b* the width of the centre-of-mass peak is larger than the one seen in Fig. 3.5 *a*. This reflects the fact the size of the ion source exit aperture that defines the maximum size of the parent beam was increased from 400 μm to 1150 μm. The shoulders in Fig. 3.5 *b* are due to false coincidences obtained by calculating the centre-of-mass for pairs of NO and O^- resulting from different parent molecules. These false coincidences are easily avoided by centre-of-mass selection. The condition for a coincidence to be real is that both x_{CM} and y_{CM} belong to the centre-of-mass peak.

Of course, it is possible that fragments resulting from different molecules give the correct centre-of-mass position. These events cannot be differentiated from the real events and they contribute to the background. We estimate $\sim 5\%$ of the pairs are accidental coincidences. In the case of low count rate data less than 2% of the events are accidental coincidences. It is obvious that the narrower the centre-of-mass peak is, the higher is the accuracy in the determination of real coincidences.

In Fig. 3.6 we compare the kinetic energy release spectra for the two data sets. From the low beam intensity data set we analyze only those laser shots where 2 particles are detected. We compare this KER spectrum with the one obtained from analyzing the high beam intensity data set by selecting only the laser shots where at least 8 particles are detected. The two spectra show no qualitative difference proving that by allowing higher count rate, the quality of the data is preserved. The cut-off around 500 meV is due to the flag ($r \sim 85$ pixels) which intercepts also fragments with small recoil velocities.

For coincidence detection, we avoided the use of any electric field. Since the O^- fragment is negatively charged, its trajectory is slightly perturbed by residual fields and the Earth's magnetic field. The observed displacement along the x axis is approximately 10 pixels (~ 1 mm on the phosphor screen) and 15 pixels along y. Since most of the O^- fragments are isolated from the NO fragments, it is possible to correct the coordinates of the O^-. For illustration, in Fig. 3.7 we present two histograms of all x coordinates of all fragments detected during a coincidence measurement (data set presented in Fig. 3.2), before and after correction. The two inner peaks correspond to the NO signal, while the outer peaks are O^- fragments. It can be seen that, the

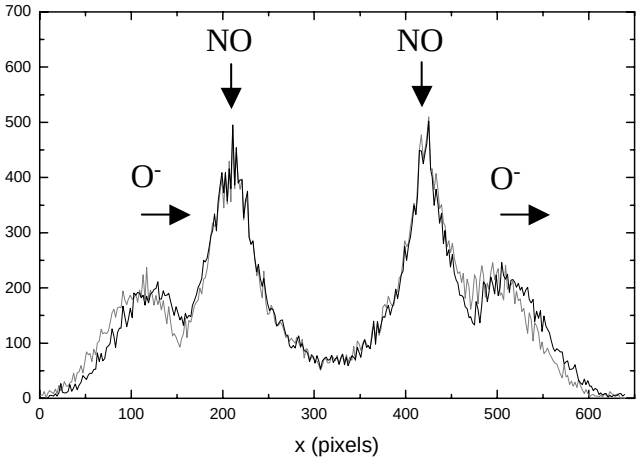

Figure 3.7: *Histograms of x coordinates of the fragments before correction (grey curve) and after the 10 pixels correction of the O^- x coordinates (black curve).*

two projected rings have their centre displaced by ~ 10 pixels. The KER distribution is generated after the correction of the (x, y) coordinates for the O^-.

3.3 Results

3.3.1 Branching between photodetachment and photodissociation

The photodestruction of the NO_2^- takes place via photodetachment and photodissociation processes. For measuring the branching between the two processes we detect only the neutral NO_2 molecules and NO fragments as it is shown in Fig. 3.3. In order to have an accurate estimate of the branching, we lowered the molecular beam intensity such that mostly one fragment is detected per laser shot (92% of the cases). This is necessary since the photodetachment signal is confined in a much smaller region on the detector than the photodissociation signal. By lowering the count rate to one fragment, we avoid overlapped photodetachment counts that cannot be resolved. This experiment is nearly background free and all signal detected is related to the presence of the laser. The particles detected in the center of the detector, confined in a circular region ($\phi = 30$ pixels) are neutral NO_2 from photodetachment process, while the

particles distributed around it are NO fragments from the photodissociation process. We found that 7.5% of the excited NO_2^- decay via photodissociation. This result is the most important new physical result of this work. We note, that the photon energy (4.66 eV) is not so much larger than the binding energy (3.96 eV). The nature of the electronic excited state is unknown other than that the transition occurs along a parallel transition (see below). In view of the limited excess energy, photoexcitation may well take place via quasi-bound states with a certain vibrational lifetime, which may then undergo enhanced photodetachment. We note that this experiment does not provide the information whether the photodetachment signal is due to a direct photodetachment process or the result of photoexcitation of the anion to an excited state that undergoes autodetachment. A photoelectron energy spectrum would be more revealing for this distinction than the present experiment, which only measures the neutral fragment yield. The photoelectron spectrum is sensitive to the changing overlap between the anion ground state and the anion excited state with the different neutral product states. In the case of photodetachment of the excited molecular state, at higher photon energies and larger recoil velocities, the photodissociation branching may well be significantly larger.

3.3.2 Kinetic energy release spectrum and angular distribution.

In Fig. 3.6 we present the kinetic energy release spectrum for the photodissociation of NO_2^- induced by a 266 nm (4.66 eV) photon. The kinetic energy release for each dissociation event is calculated according to Eq. 3.3. Since the dissociation energy is $\sim$ 4 eV [6], assuming that no energy is stored as internal energy (neither in the parent molecule nor in the photodissociation products), the expected KER is $\sim$ 0.66 eV. The experimental data shows a large distribution of KER centered on 0.8 eV. The conservation of energy during dissociation of NO_2^-, taking into account the internal energies reads:

$$E_{int}^{NO_2^-} + h\upsilon - D_0 = E_{avl} = E_{int} + KER \tag{3.5}$$

Equation 3.5 expresses that the final observed kinetic energy release (KER) of the fragments increases with the internal energy of the anion and with photon energy. The KER decreases if the molecular (NO) and atomic (O^-) fragments end up internally excited. In the molecular fragment, energy can be stored in the form of rotational and vibrational energy. As will be described below, energy stored in fragment rotation influences the photofragment anisotropy. During the recoil, if the force is along the NO bond direction in the bent NO_2^- geometry, a significant fraction of available energy has to end up in rotation of the NO fragment. Another reason for rotational excitation is a possible large change in binding angle in going from the molecular

ground state to the dissociative state. Vibrational energy may be added by the recoil force or by the contraction or extension of the NO -bond in going from the NO_2^- anion to the dissociation products.

We note that the coincidence KER spectrum of Fig. 3.6 lacks signal below 500 meV. As mentioned before, this is due to the presence of the beam dump. The broad radial distribution of the NO fragments detected in the absence of the beam dump (see Fig. 3.3) suggests that most events will escape the flag and reach the detector. Still, there are events appearing at radial distances smaller than 85 pixels (KER_{pos} < 500 meV), that in a coincidence detection are stopped by the beam dump. These low KER values suggest that the NO fragment can convert a big part of the energy from the dissociation process into internal energy. Busch and Wilson [10] developed a model to predict the energy partitioning in the photodissociation of neutral NO_2. Taking into account the smaller bond angle of NO_2^-, we find that 24% of the E_{avl} would appear as rotational energy of the NO fragment and 76% as KER.

It is more important to realize that surprisingly large KER values are observed in the spectrum, which implies contribution of ro-vibrationally excited NO_2^- anions in the negative ion beam, indicating a non-thermal process in the ion source. The absence of clear structure in the KER spectrum, makes it impossible to say anything about the internal energy distribution in the initial ion beam. It is noteworthy that no autodetachment signal was observed in this experiment. The autodetachment channel would point at a part of the ion beam with a significant internal energy of more than 2.5 eV. It has been mentioned in the literature [6, 11] that in the hollow cathode discharge ion source filled with O_2 and N_2, vibrationally excited states may also be produced. In these reports, an onset of the photodetachment signal was observed at about 1.8 eV, indicating internal energies exceeding 0.5 eV. Our observation of KER values around 1 eV are in agreement with even larger internal energies as we expect some 25% of the excess energy at least to end up in NO rotation.

The product angular distribution (see Fig. 3.8) is described by:

$$I(\theta) \sim [1 + \beta P_2(\cos\theta)], \tag{3.6}$$

where θ is angle defined by the orientation of the molecule during dissociation with respect to the laser polarization and $P_2(\cos\theta)$ is the second Legendre polynomial. The histogram of the angular orientations of the fragments shows a large anisotropy parameter $\beta = 1.4 \pm 0.1$. Clearly, the electronic transition is a parallel transition. The predictive value of the anisotropy parameter in triatomics is smaller than in the case of diatomic molecules. For diatomics, a parallel transition yields an anisotropy parameter of $\beta = 2$. If the excited state has a finite lifetime larger than the rotational period, the anisotropy parameter reduces to $\beta = 1/2$. In triatomics, other phenomena influence the resulting anisotropy parameter. For molecules with a bent geometry, such as NO_2^-, the dipole moment is not parallel to the bond that breaks. In the case of axial recoil, implying a repulsive force along the bond direction, the maximum anisotropy parameter is reduced to:

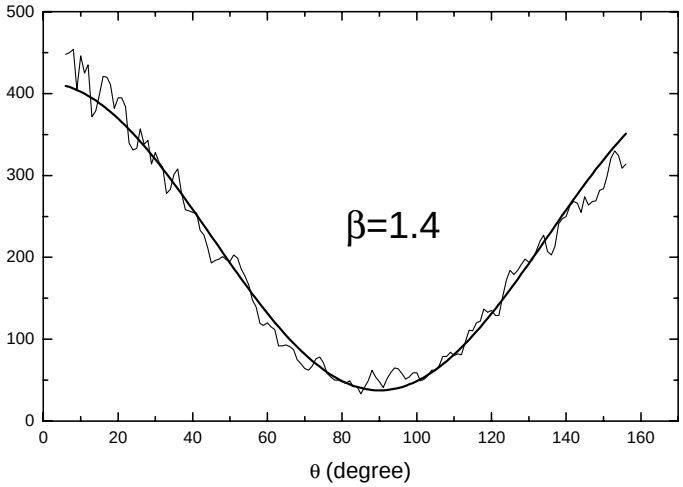

Figure 3.8: *The angular distribution of the fragments in the detector plane with respect to the laser polarization (see Eq.(3.4)). Fitting the histogram (thick curve) the anisotropy parameter* $\beta = 1.4$ *is obtained.*

$$\beta \sim 2P_2(\cos\alpha), \tag{3.7}$$

with α the angle between the bond axis and the transition dipole moment. For a bond angle of 135° as in the case of neutral NO_2, this yields an anisotropy parameter of 1.54, close to the value reported in [12]. We note that this does not imply that the NO fragment is without rotational excitation.

In fact, axial recoil, as defined above, results in rotational excitation of the fragment depending on the molecular geometry. For the present case with an equilibrium angle of the NO_2^- of 117.5°, an anisotropy parameter results of, $\beta = 1.2$, which is in fact smaller than the measured value in this work. In the case that the transition occurs between states with different equilibrium geometries, in particular the equilibrium angle, the excited state molecule will be formed with a considerable amount of bending excitation. The competition between the torque related to the bending motion and the axial recoil force determines the final anisotropy. The effect of the torque may be expressed in an angle ψ, which weighs the radial kinetic energy release. The anisotropy parameter is written as $\beta = 2P_2[\cos(\alpha+\psi)]$ [13]. If a transition takes place towards a state with a more linear geometry than the ground state geometry, the combination of forces along the rupturing bond and in the perpendicular direction may in fact lead to an increase in the anisotropy parameter. In our case our anisotropy

parameter would imply a value of $\psi = -5°$. In general however, large torques result in a further reduction of the anisotropy parameter. In fact, the shape of the excited state potential determines the lifetime of the excited state and the distribution of the forces over bending and recoil motion. This result in a correlation between the fragment rotational energy and the observed anisotropy parameter. As in diatomics, a lifetime of the excited complex, that is comparable to the rotational period of the parent anion, also reduces the anisotropy parameter.

In our experiments, we find that the kinetic energy release spectrum contains dominantly values from 500 meV to more than 1 eV. The magnitude of the observed KER values implies the necessity of considerable excitation energy in the parent anion. It is unlikely that most of the available energy ends up in rotational energy of the NO fragment. The magnitude of the anisotropy parameter indicates a short lifetime of the excited state. Finally, the value of $\beta = 1.4$ suggests that the excited anion state may have a more linear geometry than its parent anion state. It is of interest to note that the possible presence of an autodetachment channel in the excited state may affect the anisotropy parameter. For example, long-lived anionic excited states, which would reduce the anisotropy parameter, may more prone to the autodetachment process and do not contribute to the photofragment channel.

The anion of nitrogen dioxide is a species that is important in the upper atmosphere. This molecular anion is more stable than its parent neutral, an unusual situation. The excess electron is captured in a bonding orbital. In view of its stability, photodestruction will be an important channel for removal of these species in the ionosphere. To the best of our knowledge the photodestruction of the NO_2^- has not been determined in much detail. This work provides the branching of the two pathways (7.5% photodissociation versus 92.5% photodetachment). As important, this research shows that coincident detection of molecular fragments from photodissociation in order to obtain high resolution KER information is possible also when using relatively low repetition rate lasers. The combination of a detector that can determine the arrival position and arrival time of many particles and a setup with well defined beam properties ensures this possibility.

Bibliography

[1] K.A. Hanold, A.K. Luong, R.E. Continetti, J. Chem. Phys. **109,** 9215 (1998)

[2] R. Li, R.E. Continetti, J. Phys. Chem. A **106,** 1183 (2002)

[3] L. Thomas, Radio Sci. **9,** 12 (1974)

[4] S.B. Woo, E.M. Helmy, P.H. Mauk, A.P Paszek, Phys. Rev. A **24**,1380 (1981)

[5] C. Meredith, R.D. Davy, G.E Quelch, H.F. Schaefer, J. Chem. Phys. **94**, 1317 (1991)

[6] B.A. Huber, P.C. Cosby, J.R. Peterson, J.T. Moseley, J. Chem. Phys. **66**, 4520 (1977)

[7] L.Dinu, A.T.J.B. Eppink, F. Rosca-Pruna, H.L. Offerhaus, W.J. van der Zande, M.J.J. Vrakking, Rev. Sci. Instrum. **73**, 4206 (2002)

[8] D.Strasser, X.Urbain, H.B. Pedersen, N.Altstein, O.Heber, R.Wester, K.G. Bhushan, D.Zajfman, Rev. Sci. Instrum. **71**, 3092 (2000)

[9] R.Bobbenkamp, Ph.D. Thesis, Bielefeld, 2002.

[10] G.E. Busch, K.R. Wilson, J. Chem. Phys. **56**, 3626 (1972)

[11] E. Herbst, T.A. Patterson, W.C. Lineberger, J. Chem. Phys. **61**,1300 (1974)

[12] A.V. Demyanenko, V. Dribinski, H. Reisler, M. Meyer, C.X.W. Qian, J. Chem. Phys. **111**, 7383 (1999)

[13] G.E. Busch, K.R. Wilson, J. Chem. Phys. **56**, 3638 (1972)

Chapter 4

Predissociation and autoionization of Rydberg states in H_2

We present single-photon spectroscopy in molecular hydrogen starting from the metastable $c^3\Pi_u^-$ state to a number of triplet nd-Rydberg states ($v = 0 - 4$, $n > 12$). Using fast beam spectroscopy both the autoionization channel and the predissociation channel are quantified, field-free as well as with small electric fields. The use of fast beam photofragment spectroscopy makes it possible to determine in the predissociation signal the initial ro-vibrational levels in the $c^3\Pi_u^-$ state. Coupling with the $i^3\Pi_g$ state is assumed to be responsible for field-free predissociation of the $v = 0$ Rydberg levels. The stronger observed predissociation channel of the $v = 1$ Rydberg levels is due to the non-adiabatic interaction with the $h^3\Sigma_g^+$ state in combination with l-mixing due to the external electric field. No direct evidence is found for possible predissociation of the gerade Rydberg states by low lying ungerade states. The competition between autoionization and predissociation is discussed in terms of possible consequences for dissociative recombination involving low energy electron collisions with the H_2^+ molecular ion.

4.1 Introduction

The spectroscopy of molecular hydrogen has been studied in great detail over many decades with many different techniques. Most of the molecular states in hydrogen are Rydberg states, which have one confined orbital and one more diffuse outer orbital. The lower lying states have been calculated with very high precision by Kołos and Wolniewicz [1–3]. The Rydberg states have rich dynamics with radiation, autoionization, and predissociation as potential decay channels. Most of these processes have been studied not only experimentally but also theoretically, often employing Multichannel Quantum Defect Theory (MQDT) [4–7]. Most research has been directed to the p-electron Rydberg series, being accessible from the electronic ground state with one photon. In these *ungerade* Rydberg series, also higher angular momentum *ungerade* states have been studied (f-series) starting from the ground state [8, 9]. Using multi-photon processes also the *d-* and *s-gerade* Rydberg series have been detected and characterized [10]. Being a light molecule, the triplet and the singlet states are not connected spectroscopically, hence, the triplet Rydberg series are not accessible from the electronic ground state. Still, these Rydberg states have been studied starting from the long-lived metastable $c^3\Pi_u^-$-state, which has an excitation energy of approximately 11.6 eV, and which may be produced by low energy electron impact or using charge transfer collisions between molecular hydrogen ions and alkali atoms, such as sodium, rubidium or cesium [11,12]. For these reasons, most studies in triplet hydrogen have focussed on the *nd-gerade* Rydberg series [13–15]. To the best of our knowledge no triplet *np-ungerade* Rydberg series have been detected. Using microwave spectroscopy, Lundeen and co-workers have measured high-resolution spectra of nonpenetrating high l-states [16,17]. Hyperfine structure in low l-states of very high n-Rydberg states has been recently reported in a beautiful series of experiments [18].

The electronic structure of molecular hydrogen results in dynamics, which differs strongly for different symmetries and multiplicities. Molecular hydrogen has doubly excited states in which both electrons occupy an excited orbital. The lowest doubly excited state is the $(2p\sigma_u)^2\ ^1\Sigma_g^+$ state and it crosses the ionic ground state near the outer turning point of the second ($v^+ = 1$) vibrational level (see Fig. 4.1). The lowest repulsive *ungerade* state and the lowest triplet *gerade/ungerade* states are the $(2p\sigma_u 2s\sigma_g)\ ^{1,3}\Sigma_u^+$ and $(2p\sigma_u 2p\pi_u)\ ^3\Pi_g$ states, which cross the ionic ground state near the outer turning point of the $v^+ = 5 - 6$ vibrational levels. The different doubly excited characters have large effects on the lower lying adiabatic electronic states. The $(2p\sigma_u)^2\ ^1\Sigma_g^+$ -character is responsible for the double well character in the first members of the $(ns\sigma_g)\ ^1\Sigma_g^+$ states. The $(2p\sigma_u 2p\pi_u)\ ^3\Pi_g$ doubly excited state is visible in the potential barrier in the $(3d\pi)\ i^3\Pi_g$ state. Also in the next member of the $^3\Pi_g$ series, the $(4d\pi)\ ^3\Pi_g$ state, the effect of the doubly excited character is present. Vibrational autoionization of $(4d\pi)\ ^3\Pi_g$ levels excited from high $v = 9 - 12$ of the $c^3\Pi_u^-$ state, with a change of up to 10 vibrational quanta has been observed [19, 20]. This extreme non-Frank-Condon behavior was attributed to the interaction of singly

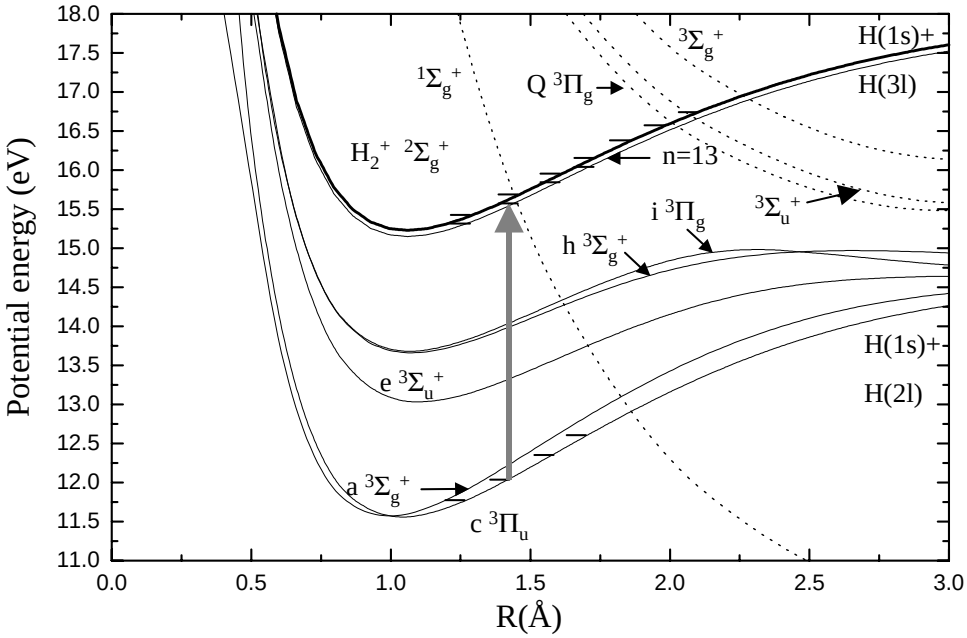

Figure 4.1: *Potential enery curves for molecular hydrogen. The black lines are the diabatic potentials for molecular hydrogen from Ref.* [35]. *The repulsive curves are taken from Ref.* [25].

excited $(4d\pi)$ $^3\Pi_g$ state and the doubly excited $(2p\sigma_u 2p\pi_u)$ Q_1 $^3\Pi_g$ state.

Apart from the intrinsic interest in understanding and potentially manipulating the decay dynamics of the Rydberg states, a direct relation exists between the dynamic behavior of these Rydberg states and the efficiency and dynamics of low energy electron collisions on molecular hydrogen, $H_2^+ + e^- \rightarrow H(1s) + H(nl) + KER$. This process is called dissociative recombination (DR). The kinetic energy of the fragments depends on the internal state of the molecular ion, the collision energy and the internal energy of the excited $H(nl)$ hydrogen fragment. In accordance with the concepts of the very successful multichannel quantum defect theory (MQDT), low energy collisions of electrons with the molecular ion core have a large resemblance with the interactions between the Rydberg electron and the ionic core. The latter interactions cause the perturbations and decay of the associated Rydberg states. Real electron collisions sample all partial waves and both multiplicities. In many calculations involving DR of H_2^+ only the so-called direct DR process through the capture of an $\varepsilon d\sigma_g$-electron in the doubly excited $(2p\sigma_u)^2$ $^1\Sigma_g^+$ -repulsive state, is taken into

account [21–24]. The logical consequence of this restriction is that neither the triplet channels nor the *ungerade* partial waves are considered to result in DR. A best observed estimate of the DR rate at 300 K (electron temperature) is $2 * 10^{-8} cm^3 s^{-1}$, a value that is significantly smaller than the DR rate of many other species.

Next to the DR mechanism that involves capture of the continuum electron into a doubly excited state, an alternative mechanism has been postulated for the cases of HeH^+ and H_3^+ [25, 26]. The observation of a significant DR rate of HeH^+ required a new mechanism as this ion lacks a doubly excited state with a crossing through the bottom of the ionic ground state potential curve. In this mechanism, electron capture occurs directly into the dissociation continuum of lower lying Rydberg ($n = 3$) states in a quasi-one electron process driven by the nuclear kinetic energy d/dR-operator. Logically speaking, this process may contribute to the DR rate in molecular hydrogen for the triplet channels, as well as for the singlet *ungerade* channel.

We present here single-photon spectroscopy in molecular hydrogen starting from the metastable $c^3\Pi_u^-$ state to a number of triplet nd-Rydberg states ($v = 0 - 4$, $n = 12 - 16$ for $v = 0$). Using fast beam spectroscopy both the autoionization channel and the predissociation channel are quantified. We believe that an observable competition between autoionization and predissociation of these Rydberg states is a good indication or maybe even a necessary (but not always sufficient) condition for DR to be efficient. By exciting the Rydberg states in a static electric field, these experiments reveal dynamics of both *ungerade* and *gerade* Rydberg states. The states that we excite have been observed before by Eyler and Pipkin [8] and Knight and Wang [14]. These authors detected the different levels using vibrational autoionization, causing the vibrational ground state levels to remain undetected.

In the present experiment also the vibrational ground state is observed by detecting predissociation products with such detail that the initial state is ro-vibrationally resolved. The present experiment uses the same microchannelplate (MCP) detector to detect the products of autoionization (H_2^+ ions) and predissociation ($H - H$ pairs), which makes it possible to assess the absolute branching.

In the following, we present our experimental setup (section 4.2), followed by a more detailed description of the triplet Rydberg levels in Hund's case-d in combination with the effect of applying a weak electric field (section 4.3). The experimental results are described in section 4.4. Section 4.5 contains an interpretation of the results, including the consequences for the DR process.

4.2 Experiment

The experimental setup is shown in Fig. 4.2. The positive ions are produced in a hollow cathode discharge ion source and extracted at 5 kV. The ions of interest, H_2^+, are mass selected by a Wien filter and introduced in a fast beam apparatus. By means of four deflection plates, the beam is guided through the apertures of the apparatus.

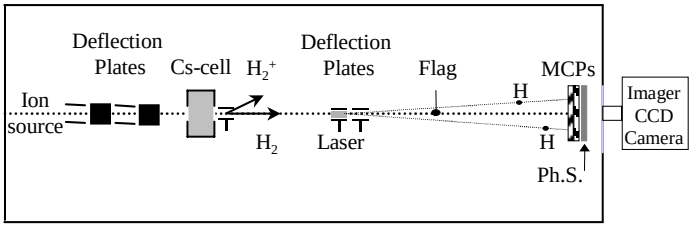

Figure 4.2: *Schematics of the apparatus. The molecular ion beam is produced in a hollow cathode ion source. The beam is extracted at 5 keV and neutralized via charge-transfer reactions with Cs. By single photon absorption Rydberg states are populated. Predissociation and autoionisation are the dominant decay paths of these high Rydberg states. A 3D detector records the position* ($\boldsymbol{x,y}$) *and the arrival time* ($\boldsymbol{t}$) *of each detected particle.*

Two Einzel lenses are used to focus the beam through the exit aperture of the ion source region and to reduce the radial size of the beam in the region of interaction with the laser. After approximately 170 cm the beam passes through a cell of Cs vapor where charge-exchange processes take place.

Part of the H_2^+ ion beam is neutralized and metastable excited states of molecular hydrogen are populated ($H_2^+(X^2\Sigma_g^+) + Cs \rightarrow H_2(c^3\Pi_u) + Cs^+$). The residual ion beam is deflected after the collision cell. The neutral beam travels undisturbed along the setup axis and 50 cm away from the cell it passes a 1 mm diaphragm and enters the interaction region with the laser. The molecular beam and the laser cross at 90 degrees. The laser system used for this experiment consists of a 50 Hz Spectra Physics Nd-YAG laser pumping a Lambda Physik ScanMate dye laser. The output of the ScanMate (around 690 nm) is frequency doubled by a KDP-C non-linear crystal. The UV laser light has an energy of 5 mJ per pulse and it is line focused into the apparatus onto the molecular beam. The length of the line focus (1−2 cm) determines the overlap region between the molecular beam and the laser. Photons are absorbed and high Rydberg states are populated. The lifetime of these Rydberg states is short compared with the time-of-flight of the molecules in the laser region (∼15 ns/cm) therefore we can say that autoionization and predissociation occur inside the laser focus. The processes that can take place are:

$$H_2 + h\nu \rightarrow H_2^*(Rydberg) \rightarrow H_2^+ + e^-, \quad (4.1)$$
$$\rightarrow H_2^*(Rydberg) \rightarrow H + H \quad (4.2)$$

If predissociation (see Eq. (4.2)) occurs, two hydrogen atoms fly apart with a kinetic energy corresponding to the internal state of the Rydberg molecule. After a time-of-flight of ~ 1.8 μs the atoms hit the time- and position-sensitive detector. By measuring the kinetic energy release in the predissociation process, useful information can be extracted concerning the molecular Rydberg state (the energy of the state, the angular orientation of the molecule, etc.).

If the molecule is oriented perpendicular to the setup axis z while dissociating, the kinetic energy released is encoded in the distance between the fragments. If the molecule is oriented along the z axis, the fragments arrive in the same spot on the detector, but with a maximum time difference. For a randomly oriented molecule, the kinetic energy release can be expressed:

$$KER = \frac{E_0}{4L^2}(D^2 + v_0^2 \Delta t^2), \quad (4.3)$$

where E_0 is the kinetic energy of the beam (5 keV), L is the distance between laser region and detector (125 cm), D is the distance between the fragments on the detector, v_0 is the velocity of the beam ($\sim 7 * 10^5$ m/s) and Δt is the arrival time difference of the fragments.

In order to determine the kinetic energy release, both fragments must be detected. Two particles are recognized as fragments of the same molecule if their centre-of-mass coincide with the centre-of-mass of the ion beam.

The detector consists of a stack of two microchannelplates and a $P46$ phosphor screen. A double exposure CCD camera is placed behind the phosphor screen. The camera retrieves the (x, y) coordinates of the spots with 80 μm resolution and the arrival time of the particles with 1 ns resolution [27, 28]. The camera is the master clock of the experiment and it runs at 25 Hz.

4.3 Rydberg states

The Rydberg states that are studied in this paper may be described as a hydrogenic Rydberg electron orbiting a H_2^+ ($^2\Sigma_g^+$) ion core. We use Hund's case-d to describe these states. The angular momentum of the excited electron, $\mathbf{l}$, is decoupled from the molecular axis and is coupled to the angular momentum of the ionic core ($\mathbf{R} = \mathbf{N}^+$). The total angular momentum and $\mathbf{N}$ is the vector sum $\mathbf{N} = \mathbf{R} + \mathbf{l}$. The initial $c^3\Pi_u^-$ state is described in Hund's case-b. In this coupling scheme the electronic orbital

angular momentum **L** couples strongly to the molecular core and the projection Λ is a good quantum number. The rotational states are indexed according to N_c, the total angular momentum exclusive of spin. We use the index c to distinguish it from the total angular momentum of the Rydberg states, N. In the initial $c^3\Pi_u$ state only one of the parity states is metastable; the $c^3\Pi_u^+$ state is rapidly predissociated by the $b^3\Sigma_u^+$ -state. As a consequence, the *para*-hydrogen occupies the even angular momentum states, while the *ortho*-hydrogen occupies the odd angular momentum states. From the c-state, with a $2p\pi_u$ outer electron, in the single electron picture, either nd- or ns-states can be excited. The transition strength of $ns \leftarrow 2p$ is smaller than the $nd \leftarrow 2p$ by a factor of 30 [15]. Hardly any ns-transitions have been reported so far. To the best of our knowledge the $4s^3\Sigma_g^+$ is the only Rydberg state (with n larger than 3) that has been detected [29].

The transition to the Rydberg state is characterized by $H_2(c^3\Pi_u^-)+h\nu \rightarrow H_2^*(^2\Sigma_g^+ + nd)$. The accurate energy levels of the initial $c^3\Pi_u^-$ state are taken from Dieke's table [30]. The values are corrected by 149.6 cm^{-1} [9, 31]. The constants for the H_2^+ ($^2\Sigma_g^+$) are $\omega_e = 2321.7\ \mathrm{cm}^{-1}$, $\omega_e\chi_e = 66.2\ \mathrm{cm}^{-1}$, $B_e = 30.2\ \mathrm{cm}^{-1}$, $\alpha_e = 1.68\ \mathrm{cm}^{-1}$and $D_e = 0.618\ \mathrm{cm}^{-1}$ [32].

In order to accurately estimate the energy of the rotational Rydberg states we used an *ab initio* model developed by Eyler and Pipkin [13]. This model has been successfully applied [9, 14]. In brief, the lowest-order couplings that perturb the Rydberg electron from hydrogenic energies are considered. There are two effects: (1) The potential experienced by the outer electron is expanded into a multipole series, in which the quadrupole moment of the H_2^+ core is the first non-zero term; (2) The presence of the outer electron induces mixing of the core states and this is taken into account by considering the polarizability of the H_2^+ core. The matrix elements of the polarizability and quadrupole moment perturbations are obtained in a case-d basis. The derived first-order energy corrections are:

$$E^{(0)} = -A*C*Q(v,R) - \frac{1}{2}B*\alpha(v,R) - \frac{1}{3}A*B*\gamma(v,R), \tag{4.4}$$

$$A = \frac{3Y(Y-1) - 4R(R+1)L(L+1)}{2(2L-1)(2R-1)(2L+3)(2R+3)}, \tag{4.5}$$

$$B = \frac{\frac{1}{2}[3n^2 - L(L+1)]}{n^5(L+\frac{3}{2})(L+1)(L+\frac{1}{2})L(L-\frac{1}{2})}, \tag{4.6}$$

$$C = \frac{1}{n^3(L+1)(L+\frac{1}{2})L}, \tag{4.7}$$

$$Y = R(R+1) + L(L+1) - N(N+1). \tag{4.8}$$

The $Q(v,R)$, $\alpha(v,R)$ and $\gamma(v,R)$ are polarizability and quadrupole constants. Eyler and Pipkin calculated these constants for $v = 0-3$ and $R = 0-3$. They

observe a weak dependence of these constants on the rotational quantum number and a stronger dependence on the vibrational level [13].

In our *ab initio* calculation we use their formalism Eq. (4.4) and the values for polarizability and quadrupole constants. For $R = 4 - 6$ we use extrapolated values of the constants. The transitions $H_2^*(v, R, N) \longleftarrow H_2(c^3\Pi_u^-)(v, N_c)$ are indexed by (R, N, N_c). The allowed optical transitions are characterized by $\Delta N = 0, \pm 1$ and a strong propensity rule reads $R(\text{or } N^+) = N_c$. The conservation of *ortho-* and *para-*hydrogen, demands $R = N_c$, $N_c \pm 2$. The latter change is unlikely because of the weak interaction of the Rydberg electron with the ionic core. The shape of the potential curves and the similarity of the vibrational constants of the initial state ($\omega_e = 2466.9$ cm^{-1}) and the ionic state ($\omega_e = 2321.7$ cm^{-1}) explains the prevailing of $\Delta v = 0$ transitions over $\Delta v \neq 0$ transitions.

Autoionization processes involve an interaction of the outer electron with the ionic core, which results in a decrease of the vibrational energy with one quantum, accompanied by excitation of the Rydberg electron in the ionization continuum. Predissociation conserves the overall parity and the total angular momentum of the states involved. The predissociation channels either have the same overall symmetry (homogenous interaction) or, for example in case of rotational coupling, electronic orbital angular momentum and rotational angular momentum are exchanged. In the present experiments, the excited Rydberg states dissociate into $H(1s)+H(2l)$ fragment pairs.

4.4 Results

The experiments take place in a *fast beam* apparatus, which allows a large detection probability of the fragments on a MCP detector. The detection probability of ionic H_2^+ is similar to the detection probability of the atomic fragments $H(1s)$ and $H(2l)$, therefore comparison between autoionization and predissociation yield is possible. We note that the metastable hydrogen molecules are excited in a crossed beam setup. All these excited molecules decay and the fragments are detected. Hence, the signal strength does not reflect the decay rates but more the excitation probabilities involved. In the case of competition, the ionization and dissociation yields reveal the ratio between the two decay pathways. In our experiment, two observations exist that directly reveal crude limits of the absolute decay rates. Lifetime broadening may reveal very short-lived states in the wavelength spectra. Very long-lived states (lifetimes > 20 ns) will produce distorted kinetic energy release features in our coincidence spectrum.

By scanning the laser over 5 nm ($343.3 - 348.3$ nm) we induce transitions from the initial $c^3\Pi_u^-$ state ($v = 0 - 4$) to high Rydberg states that subsequently predissociate to the first excited dissociation limit. A sample of the raw data is presented in Fig. 4.3 (a). The data is integrated over thousands of laser shots; in the middle of the picture one can see the shadow of the flag used to dump the undissociated parent

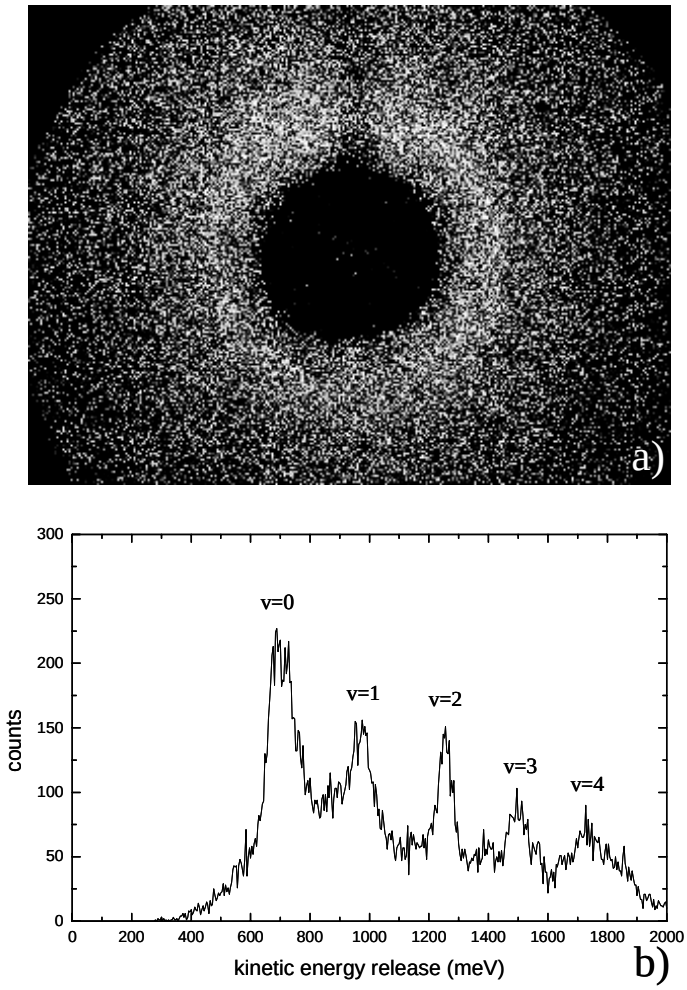

Figure 4.3: *a) Raw data for the predissociation scan between 343.3-348.3 nm; b) KER histogram over the same photon range; five peaks are observed, indicating excitation from the* $v = 0 - 4$ *levels in the* $c^3\Pi_u^-$ state.

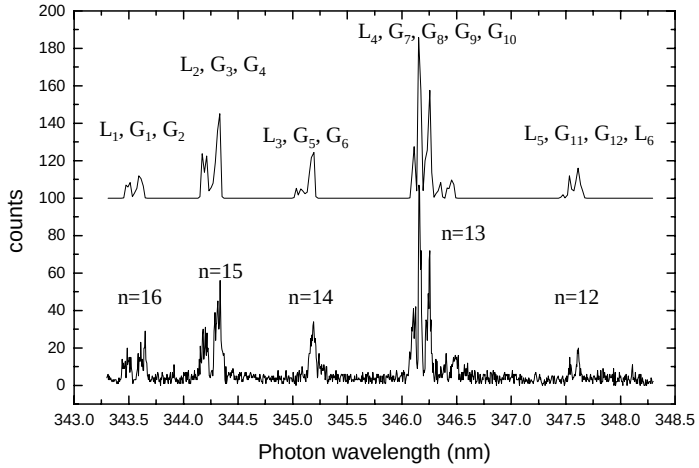

Figure 4.4: *Predissociation scan of $v = 0$ Rydberg states. In the upper part the fit of the predissociation scan is shown. The observed lines are indicated. Often few rotational transitions cannot be resolved and they appear as G_i lines (see* Table I*).*

beam. Each dissociation event consists of two fragments detected in coincidence and having the centre-of-mass confined in a central region of 50x80 pixels (the CCD chip has 640x480 pixels). For each dissociation event the camera records the (x, y) position of the particles as well as the arrival time t. Figure 4.3 (b) shows the calculated KER spectrum (see Eq. (4.3)), integrated over the whole wavelength spectrum. The peaks are labeled with the initial vibrational state. The change in photon energy during the scan is much smaller than the vibrational separation. The width of the vibrational peaks is caused by the change in photon energy (maximum 50 meV over the full scan) and the presence of different rotational states in the fast metastable beam.

The spectrum also contains background signal related to spontaneous dissociative decay of vibrational excited states in the fast beam. We can distinguish between a background dissociation and a laser induced one using the time selection. The latter implies that photofragments arrive at the detector only in a time window ($\sim$ 30 ns) related to the firing of the laser. The fragments resulting from background dissociations appear continuously distributed over the detection gate ($\sim$ 200 ns). By imposing the restriction on the arrival time of the fragments we decrease the

background level by 85 %.

The observed KER values can be used to generate state-selective predissociation spectra. In the case of autoionization, only the molecular ion is detected, which makes it impossible to determine the initial state for each event. Another major advantage of predissociation study is allowing the investigation of the $v = 0$ Rydberg levels. These states lie below the ground state of the ion H_2^+ ($^2\Sigma_g^+$), therefore they appear only in the predissociation scans.

4.4.1 Predissociation of $v = 0$ Rydberg states

The KER spectrum is used for selecting only predissociation events originating from $v = 0$ levels (by selecting only events that have a KER between 600 meV and 800 meV). In Fig. 4.4 we present the $v = 0$ spectrum over the 343.3−348.3 nm wavelength region. Five groups of lines can be seen, corresponding to five different Rydberg states ($n = 12$ to $n = 16$). Each group contains contributions from different rotational transitions. With the exception of the $n = 13$ states, for each electronic Rydberg state we observe contributions of 8 rotational transitions, originating from $c^3\Pi_u^-$ ($N_c = 1-3$) via Rydberg states characterized by $R = N_c = 1-3$ and $N = 1-4$. The $n = 13$ state is the strongest and 15 rotational transitions contribute to the spectrum. The transitions are characterized by $R = N_c = 1-5$ and $N = 1-6$.

In the upper part of Fig. 4.4 we present a least square linear fit of the $v = 0$ predissociation spectrum. We use the calculated energies of 46 transitions that are expected to appear in the (343.3 − 348.3 nm) wavelength region to generate 46 Gaussian distributions representing the individual rotational transitions. The resolution of our experiment does not allow to resolve the rotational spectrum entirely. Out of the 46 transitions we identified 6 individual rotational transition $L_1 - L_6$ and 12 groups of transitions $G_1 - G_{12}$. These distributions appearing at wavelengths fixed by the *ab initio* calculation are used for the fitting of the predissociation spectrum. The fit is a linear combination of 18 lines:

$$y(\lambda) = \sum a_l * L_l(R, N, N_c, \lambda) + \sum b_l * G_l(\lambda) \tag{4.9}$$

The L_l refer to individual rotational transitions indexed by the quantum numbers R, N and N_c, while $G_l(\lambda) = \sum L(R, N, N_c, \lambda)$ describe transitions that are not resolved. The results, consisting of fit coefficients a_l and b_l, are presented in Table I. These 18 coefficients describe the predissociation yield of the 18 lines. The unresolved rotational transitions that contribute to each G_l line are specified by their index (R, N, N_c).

As mentioned earlier, the intensity of the peaks represents the excitation probability in combination with the population of the initial state. Only in the case of two or more decay channels is the intensity also determined by the relative decay rate of the

different channels. The spectrum in Fig. 4.4 shows a surprising odd-even oscillation in intensity; the $n = 13$ and $n = 15$ are clearly more intense than the neighboring states. The fit coefficients reveal this very clearly (see Table I). Table I also shows that the contribution of the *para*-rotational levels ($N_c = 2$) is weaker than the contribution of *ortho*-rotational levels (odd N_c). The $n = 13$ Rydberg state is particularly strong. Possible reasons for an enhanced excitation probability are discussed below.

TABLE I. Summary of $H_2^*(R, N) \longleftarrow H_2(c^3\Pi_u^-)(N_c)$ $v = 0$ transitions.

Obs. Lines[a]	Transitions[b] (R,N,Nc)	Fit coefficients %	Rydberg series	Fit coefficients[c] %
L_1	*121*	1.1 ± 1.0	n=16	6.1
G_1	*111+232+222+212*	0.9 ± 1.0		
G_2	*343+333+323*	4.1 ± 0.5		
L_2	*121*	4.8 ± 0.5	n=15	20.8
G_3	*111+232+333+212*	3.8 ± 1.0		
G_4	*343+333+323*	12.2 ± 2.0		
L_3	*121*	0.6 ± 1.0	n=14	10.5
G_5	*111+232+222+212*	0.7 ± 1.0		
G_6	*343+333+323*	9.2 ± 1.0		
L_4	*121*	6.4 ± 1.0	n=13	53.0
G_7	*232+111+222*	21.6 ± 2.0		
G_8	*212+343+333+323*	19.6 ± 2.0		
G_9	*454+444+434*	1.9 ± 1.0		
G_{10}	*555+565+545*	3.4 ± 0.5		
L_5	*121*	0.3 ± 0.5	n=12	9.5
G_{11}	*232+222+111*	2.5 ± 0.5		
G_{12}	*212+343+333*	3.9 ± 0.5		
L_6	*323*	2.8 ± 1.0		

[a] L_i labels single transitions; G_i labels a group of transitions.

[b] Contributing rotational transitions are indexed after quantum numbers R, N and N_c.

[c] Integrated predissociation yield for one Rydberg state.

We note that the best fit of $v = 0$ transitions has been obtained for a quantum defect of -0.01 ± 0.005, indicating that the d-Rydberg states are degenerate with the high l-series.

The $n = 13$, $v = 0$ Rydberg states shows a particularly strong predissociation behavior. The strong yield makes it possible to further distinguish the individual

transitions by selecting within the $v = 0$ KER peak also the different rotational levels. Table II shows these results together with the calculated $n = 13$, $v = 0$ rotational transitions that are taken into account in the fit. The *ab initio* formalism of Eyler and Pipkin has been used to calculate the energy of the Rydberg rotationally excited states. The photon energies as well as the KER corresponding to each of these transitions are shown. One can see that some of the rotational transitions appear almost at the same excitation frequencies (i.e., *232*, *111* and *222* forming the G_7 line). The frequency difference for these transitions is less than 1 cm^{-1}, a splitting that our experimental resolution cannot resolve. Still, transitions that originate from different rotational states ($N_c = 1$ and $N_c = 2$) have different kinetic energy release values (see Table II).

TABLE II Details of the $H_2^*(n = 13, R, N) \longleftarrow H_2(c^3\Pi_u^-)(N_c)$ $v = 0$ transitions.

Ab initio					Fit	KER Analysis
Transitions (R,N,N_c)	Energy[a] (cm^{-1})	transitions (cm^{-1})	KER (meV)	Obs. lines	Coefficients %	Coefficients[b] %
121	123827.3	28885.58	676.0	L_4	12.2	12.2
232	123943.7	28881.18	690.4	G_7	40.9	11.5*
111	123821.9	28880.20	675.3			17.9
222	123942.3	28879.80	690.3			11.5*
212	123939.6	28877.04	689.9	G_8	36.9	4.5
343	124117.7	28875.17	712.0			10.8*
333	124117.1	28874.65	711.9			10.8*
323	124114.9	28872.44	711.7			10.8*
454	124347.8	28867.46	740.5	G_9	3.6	1.2*
444	124347.7	28867.34	740.5			1.2*
434	124345.7	28865.39	740.3			1.2*
555	124632.5	28858.05	775.8	G_{10}	6.6	2.2*
565	124632.4	28857.95	775.8			2.2*
545	124630.7	28856.28	775.6			2.2*

[a] *Ab initio* calculation using Eyler and Pipkin formalism for the energy of rotationally excited Rydberg states.

[b] From KER analysis the contribution of different N_c states is estimated.

* These transitions initiated from the same N_c state cannot be resolved and they appear as with equal contribution.

We separate the rotational transitions by analyzing only events with KER of 660-680 meV. This spectrum has a dominant contribution from $N_c = 1$ transitions. We repeat the selection of dissociation events for KER values between 680-700 meV, corresponding to $N_c = 2$ transition as well as for 700-725 meV, corresponding to

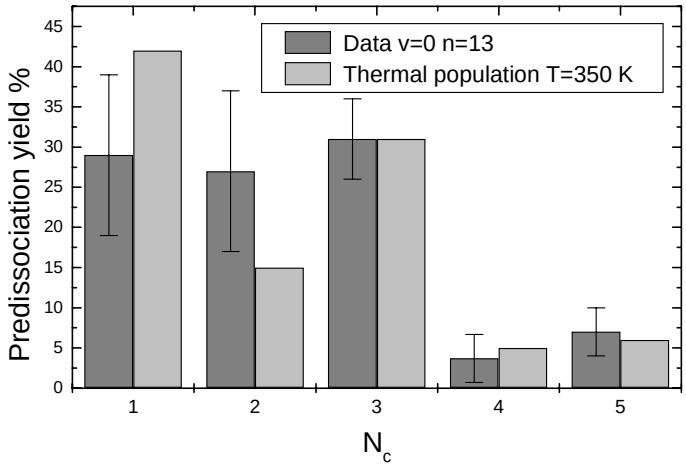

Figure 4.5: *Comparison between the rotational* ($R = N_c$) *contribution to the* $n = 13$, $v = 0$ *spectrum and an expected rotational population of the* $c^3\Pi_u^-$ $(v = 0)$ *at* $T = 350$ *K.*

$N_c = 3$ transition. Three spectra have been obtained, which contain dominantly rotational transitions starting from one defined N_c state. By fitting these three spectra with $N_c = 1$, $N_c = 2$ and $N_c = 3$ transitions respectively we obtain the relative contributions of different rotational states to the G_7 and G_8 lines of $v = 0$ spectrum. We stress here that this method helps us to estimate the contribution of different rotational transitions to the same line, but it does not resolve the contribution of different transitions starting from the same rotational state N_c (i.e., *232* and *222* forming the G_7 line). These transitions cannot be resolved and therefore they appear in Table II with equal coefficients.

Despite of the limited spectral resolution, the use of the KER analysis makes it possible to quantify the contribution of the different initial rotational states to the observed intensity. This is certainly relevant as an indication for the nature of the perturbations that affect the observed peak strengths. Figure 4.5 compares the observed contributions of the different rotational states with an expected population using a thermal rotational distribution at $P(N_c) = (2N_c + 1) * c * e^{\frac{-\beta_e N_c(N_c+1)}{kT}}$ at $T = 350$ K. Under inclusion of the para-ortho modulation c, we observe a satisfactorily agreement. We conclude that the large intensity of the $n = 13$ Rydberg state is not a consequence of a rotational state dependent interaction with another state.

As we have described before, these experiments have been performed in the presence of a weak electric field of about 200 Vcm^{-1} (see Fig. 4.2). The effect of this

small field differs for the $v = 0$ levels in comparison to $v = 1$ levels. Whereas for the $v = 1$ levels, the observed predissociation yield changes significantly, this is not the case for $v = 0$ levels. In Fig. 4.6 we present two scans over the G7 line $n = 13$, $v = 0$, with and without the electric field. No difference is observed in the predissociation yield. A change in width is observed and it is attributed to the Stark structure of the states involved. The resolution of the experimental setup (~ 0.2 cm^{-1} laser bandwidth and ~ 0.2 cm^{-1}Doppler shift) in combination with the fact that G_7 line contains contributions from three transition *232*, *111*, and *222*, separated by ~ 1 cm^{-1} and ~ 0.4 cm^{-1} respectively accounts for the width of the line in the absence of electric field (see Fig. 4.6 (a)).

In the presence of electric field, the n-fold degeneracy of each rotational Rydberg states is lifted and the Rydberg state splits into a Stark manifold of k-states. The energy of each Stark state can be approximated by $E = -\frac{1}{2n^2} + \frac{3}{2}Fnk$, where the quantum number k runs from ($n-1$, $n-3$, ..., $-n+1$) for $m = 0$ and ($n-2$, $n-4$, ..., $-n+2$) for $m = 1$ and F is the electric field (a.u.) [33]. The splitting between two consecutive Stark states of $n = 13$ Rydberg state, in the presence of a 200 Vcm^{-1} electric field, is ~ 0.166 cm^{-1}. The maximum split (for $k = n-1, -n+1$) is ~ 4 cm^{-1}. Taking into account the Stark splitting, we can reproduce the width of the G_7 line (see Fig. 4.6(a)).

As mentioned before, the experiment makes it possible to deduce a lifetime of the upper state only if the lifetime broadening can be observed in the spectrum or, in case of very long lifetimes, from the tail of the KER peaks at smaller apparent KER values. From the analysis of the KER distributions we do not observe any asymmetry (see Fig. 4.6 (b)). No clear lifetime effect has been observed, neither with nor without the electric field. In both cases, the natural line width is smaller than 0.5 cm^{-1}. The above observations do not imply that the electric field has no effect on the predissociation lifetime. If the lifetime is reduced or enhanced in the range from 10 ps to 10 ns, this would not results in a change in the observed quantities. We have only shown that predissociation is the dominant decay channel for these Rydberg levels in the presence and in the absence of a static field. As will be shown below, in the case of the $v = 1$ levels, the predissociation yield depends strongly on the external electric field.

4.4.2 Predissociation and autoionization of $v = 1 - 4$ Rydberg states

For excited vibrational Rydberg states, autoionization becomes an open decay channel competitive to the predissociation channel. Since the lowest triplet unbound $Q^3\Pi_g$ state, leading to the $n = 2$ dissociation limit crosses the Rydberg states around $v = 5-6$ [19,20,25] direct predissociation of $v = 1$ Rydberg states is very unlikely. In contrast to this, in the presence of an electric field, we observed predissociation signal from $v = 1$, $n = 13 - 18$ Rydberg states (see Fig. 4.3(b)) as well as from $v = 2 - 4$

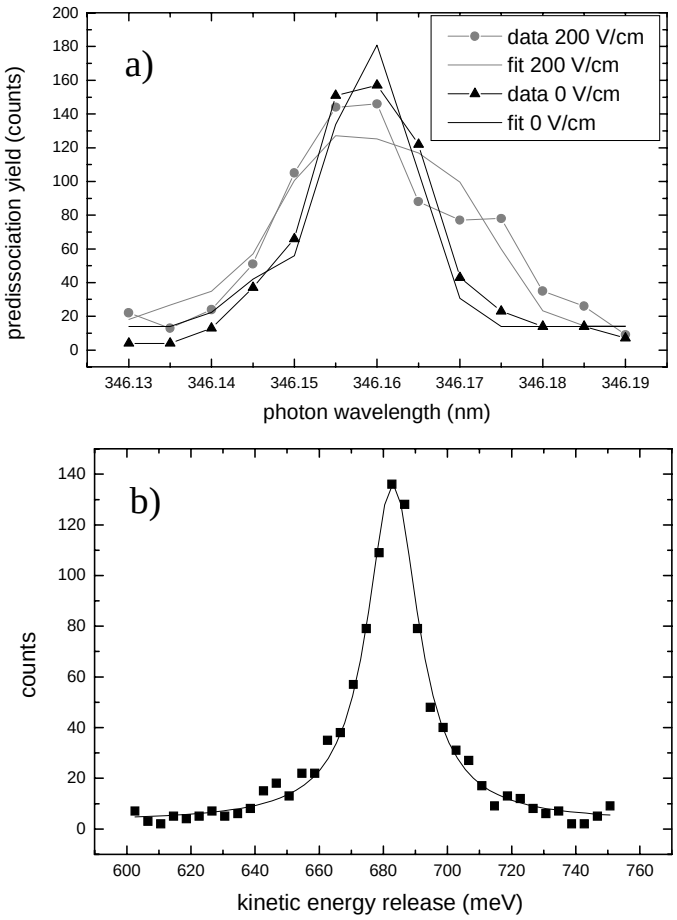

Figure 4.6: *a) Two scans over G_7 line ($n = 13$, $v = 0$) in the absence of the electric field and at 200 V/cm electric field. The width of the experimental lines can be fitted by taking into account the Doppler broadening (0.2 cm^{-1}), the laser bandwidth (0.2 cm^{-1}) and the Stark splitting. No indication of lifetime broadening is present suggesting lifetimes longer than 5 ps. b) The KER histogram over G_7 line in the absence of electric field shows no significant asymmetry. A lifetime longer than 20 ns would appear as a tale at lower KER values.*

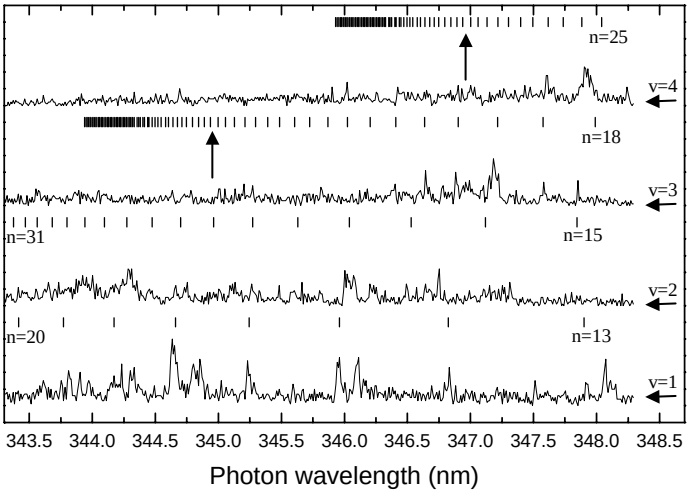

Figure 4.7: *Predissociation scans of $v = 1 - 4$ Rydberg states. For clarity only the 111 transitions are shown (field-free). The two arrows show the value of the IP in the presence of an 200 Vcm^{-1} electric field.*

Rydberg states.

By selecting events having a KER between 950 meV and 1050 meV we select transitions initiated from $c^3\Pi_u^-$ ($v = 1$) rotational states. The predissociation spectrum is presented in the lower part of Fig. 4.7. With photon wavelengths between 343.3 nm and 348.3 nm we excite the $n = 13 - 20$ Rydberg states ($v = 1$). The quality of the data does not permit a quantitative measurement of the predissociation yield for independent rotational transitions (R, N, N_c). Most of the peaks in the predissociation spectrum can be assigned. For clarity in Fig. 4.7 we show the position of the *111*-transitions. The predissociation spectra of Rydberg series ($v = 2 - 4$) are obtained in similar way using KER restrictions. The spectra are presented in Fig. 4.7 together with the position of the *111*-transitions of each n-Rydberg state. The lowest n-Rydberg state excited is specified for each vibrational spectrum. For $v = 3$ and $v = 4$ Rydberg series all the n-Rydberg states with $n > 18$ and $n > 25$ respectively are excited.

The scans have been performed in the presence of a 200 Vcm^{-1} electric field in the laser interaction region. The Stark splitting of the Rydberg states increases with n and the maximum Stark splitting increases with $n * (n - 1)$. At high values of n,

the different rotational transitions overlap due to Stark splitting. For $v = 4$ Rydberg states, the transition energy difference between different rotational states is larger than the n spacing. As a consequence, the rotational transitions of different Rydberg states mix and appear less as individual lines and more as a continuous band. The same continuous band appearance can be seen for the $v = 3$, $n > 23$ Rydberg states. Another effect of the presence of the electric field is a tilt of the Coulomb potential of the molecular core in the direction of the field. The ionization potential IP is lowered with $\Delta E = -\alpha\sqrt{F}$, where $\alpha = 6.12$ cm^{-1} and F is the electric field expressed in Vcm^{-1}. For a 200 Vcm^{-1} electric field, the IP is lowered by ~ 86.5 cm^{-1}. The Rydberg states characterized by $n < 35$ are situated below this saddlepoint. The Rydberg series with $n > 35$ are above the saddlepoint and they ionize directly. The two arrows in Fig. 4.7 indicate the position of the lowered IP of the $v = 3$ and $v = 4$ levels.

The $v = 1$ Rydberg states are energetically above the H_2^+ ($^2\Sigma_g^+$) ($v = 0$) ionic state and autoionization is possible. Autoionization is faster than predissociation. At zero electric field autoionization is the dominant decay channel for the $v = 1$ Rydberg states and predissociation is zero. The predissociation channel opens in the presence of the field (already at 25 Vcm^{-1}) and it shows a fast increase with the electric field. In Fig. 4.8(a) we present the predissociation yield of $n = 15$, $v = 1$, $R = 1$ Rydberg state versus the electric field. At zero electric field the predissociation yield is zero (background level). By increasing the electric field up to 100 Vcm^{-1} the predissociation yield increases fast. Between 100 and 200 Vcm^{-1} the predissociation yield remains constant within the experimental error and for higher electric field it shows a slow decrease. In Fig. 4.8(b) we present the autoionization yield versus electric field. The autoionization signal shows no significant dependence on the electric field. For electric fields higher than 100 Vcm^{-1}, the predissociation yield accounts for 8 % of the decay of the $n = 15$, $v = 1$, $R = 1$ Rydberg states, the rest 92 % decaying via autoionization. We conclude that the electric field does not significantly affects the excitation probability, represented by the sum of autoionization and predissociation signal, but it does affect the relative rates of these two processes.

The absence of predissociation signal for $v = 1$ Rydberg states at zero electric field indicates that the d-character of the Rydberg electron renders the predissociation a rate sufficiently small that the competition with autoionization is lost. In general, the autoionization as well as predissociation depends on the angular momentum of the outer electron. Both interactions require a collision of the Rydberg electron with the ionic core. This collision becomes very ineffective for high angular momentum states ($l > 3$). The effect of the electric field on the predissociation fraction suggests strongly that the p, and s-character, that the electrons acquire in the static electric field, drives the predissociation process. It is of interest to note here that the angular momentum mixing in Hund's case-d implies an effective mixing of *gerade* and *ungerade* character.

An ionization spectrum was obtained by counting the deflected laser induced ions onto the detector (see the grey spectrum in Fig. 4.9). The ionization spectrum con-

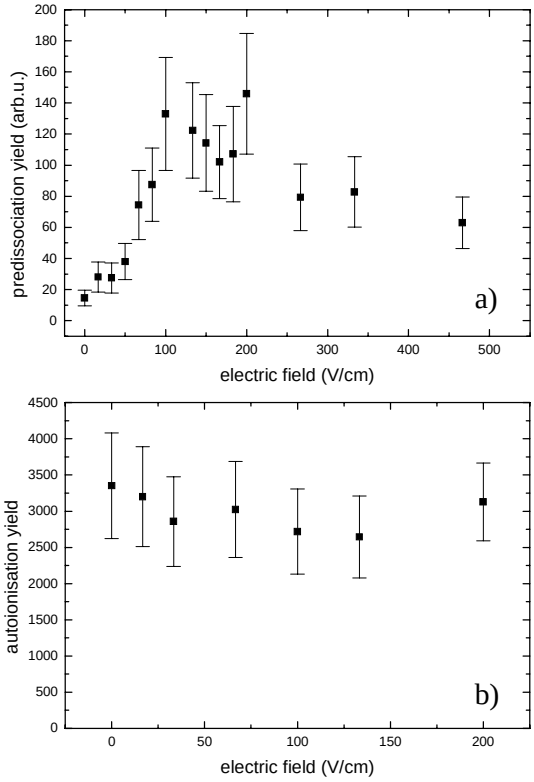

Figure 4.8: a) *The predissociation yield of $n = 15$ $v = 1$ $N = 1$ Rydberg states versus electric field. b) The autoionisation yield of the same Rydberg states versus electric field.*

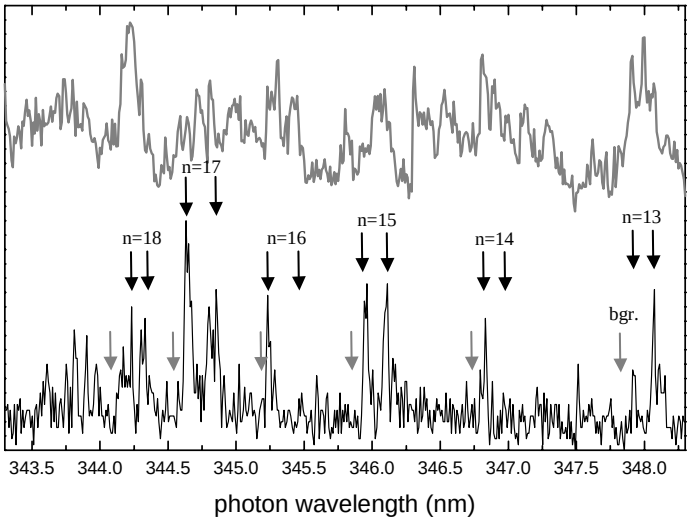

Figure 4.9: *Predissociation scan of $v = 1$ Rydberg states (black spectrum) versus autoionisation scan (grey spectrum). The branching ratios are measured at 10 photon wavelengths corresponding to $R = N_c = 1$ and $R = N_c = 3$ transitions. The background is measured at photon wavelengths indicated by the grey arrows.*

tains much more lines than the predissociation spectrum mainly because the ionization spectrum has contributions from all vibrational states that are excited, while predissociation spectrum shows only $v = 1$ transitions. In order to measure the branching ratios between the predissociation and autoionization, we set the laser wavelength on the most dominant predissociation transitions, usually characterized by $R = N_c = 1$ and $R = N_c = 3$. Both predissociation and autoionization signals are corrected for background.

The photon wavelengths corresponding to background measurements are chosen in the vicinity of the $v = 1$ transitions, as it is shown by the arrows in Fig. 4.9. In case of predissociation, after selection of the laser induced events, the background yield is low and the predissociation is accurately measured. In case of autoionization, due to the complexity of the spectrum, the background yield is much less accurately measured. It is still possible to estimate the competition between the two decay channels.Figv1dission

In case of odd and even principal quantum numbers, the average predissociation rate is ~ 7 % and ~ 2 % respectively.

4.5 Discussion and conclusions

As described in the introduction, the dissociation and autoionization dynamics of high lying Rydberg states are related to the relative DR rates of the different electron partial waves and total electronic multiplicity (total spin, $\mathbf{S} = 0$, or $\mathbf{S} = 1$). This connection between DR and Rydberg state dynamics should not be confused with the so-called indirect channel in DR [34], in which the electron-ion collision cross section shows sharp resonance features, which are attributed to the temporarily formation of quasi-bound, vibrationally excited, Rydberg states. In fact, these resonances in the DR cross sections in many cases reduce the cross section related to the direct DR process [4]. The connection between DR and the dynamics of excited Rydberg states is inspired by the ideas behind MQDT, in which the interaction between the outer diffuse Rydberg electron is closely related to the dynamics of a low energy electron collision with the molecular ion. The advantage of studying Rydberg state dynamics is that the effect of the different electron partial waves can be isolated in principle.

This study has addressed via the study of the associated Rydberg states, triplet electron collisions along the $d(\lambda)_g$ partial waves. In our study these Rydberg states are formed through excitation of the $2p\pi_u$ electron of the metastable c-state. We have observed that the d-series are subject to predissociation in the case that autoionization is energetically not allowed. Hence this holds for the nd_g, $v = 0$ levels. In field free conditions, the excited vibrational levels do not show any measurable predissociation. Recent theoretical work by Florescu et al. addressing the role of triplet H_2 in low energy dissociative recombination, reveals a significant radial coupling strength between the electron-molecular ion channel and the $i^3\Pi_g$ state [35]. This state has a $3d\pi_g$ as outer electron. Its potential curve shows a suitable potential barrier offering a dissociation continuum.

It is well known from the singlet system that the nd ($N^+ = 0$) are mixed with the ns ($N^+ = 2$) Rydberg series. This coupling reflects the approximate conserved nature of the ionic core rotational quantum number, N^+, in the Hund's case-d description. An external electric field is causing Stark structure of the l-uncoupled electrons, resulting in further mixing of s- and d-character and admixture of higher electron angular momentum states as well as p-character. We note that this implies that in the presence of an electric field, the Rydberg states can mix and be predissociated by *ungerade* lower lying states. In the present experiments, we do not find a direct evidence for the enhancement of the predissociation rate of the $v = 0$ Rydberg series due to electric field. However, we find that the predissociation rate of the $v = 1$ Rydberg states is enhanced by the electric field. Hence, we conclude that the ns_g or the np_u character can interact with a lower lying Rydberg state offering a dissociative continuum. Florescu and co-workers have evaluated the radial coupling strength of the continuum low energy electrons with the different open dissociation channels and they have found that the $(3s\sigma_g)$ $h^3\Sigma_g^+$ state has the strongest interaction. The strongest *ungerade* channel is the $(3p\sigma_u)$ $e^3\Sigma_u^+$ state, a state with a quantum defect

that is unusually large for molecular hydrogen. According to Florescu et al., the importance of this state in the DR cross section is in between that of the $h^3\Sigma_g^+$ and the $i^3\Pi_g$ states. We conclude that our observations are in agreement with the h-state to be the dominant channel.

This triplet $3d$-channel in molecular hydrogen has similarities and important differences with the singlet analogue states. The difference is due to the presence of the doubly excited $(2p\sigma_u)^2\ ^1\Sigma_g^+$ state. Rottke and Welge have studied the $3d$-Rydberg series using the $B^1\Sigma_u^+$ state as intermediate state. Strong predissociation is reported but because of experimental reasons, predissociation and autoionization could not easily be distinguished in their work. These authors stress the importance of the $(2p\sigma_u)^2$ character in the F-state of molecular hydrogen, implying the importance of the doubly excited curve in the ionization continuum. It is this singlet channel that carries most of the strength of the DR process with low energy electrons [23, 36], in which the singlet $3d\sigma$-partial wave dominates the DR process.

In the singlet as well as in the triplet manifolds, nearly none of the members of the $(3s\sigma)$ Rydberg series have been observed. Their small quantum defects cause overlap with the $3d$-series, while their oscillator strength to the $3d$-series is stronger than the $3s$ series by a factor of 30. In the experiments from Rottke and Welge a small number of high lying ns-Rydberg states have been assigned [10]. In the triplet manifold, the autoionizing experiments did not reveal any ns-series. Eyler and Pipkin have reported the lower lying $(4s)^3\Sigma_g^+$ state, which was found to be efficiently predissociated for the levels $(v > 2)$ that are situated above the barrier in the $(3s)$ $h^3\Sigma_g^+$ state [29]. The predissociation lifetimes are reported to be the order of 500 ps. Using an n^3 scaling, this would give rise to predissociation lifetimes of the order of 10 nanoseconds for $n = 13$; again the observed electric field induced predissociation in our experiments can be attributed to the $nd - ns$ mixing processes.

In a nice series of experiments, Glab and co-workers have studied the singlet $p - ungerade$ series in a multiphoton excitation step via the $E^1\Sigma_g^+$ level [37, 38]. Also in this system, in field free conditions no predissociation was observed. In this research, the excited hydrogen fragments were detected using one-photon ionization with 532 nm light. Slow predissociation with lifetime much longer than 10 ns remains undetected in this experiment. After switching on an electric field, predissociation using excitation of the p-state resonances is observed, even at very small fields of 50 Vcm^{-1}. These authors point at the admixture of ns character to explain the predissociation [37]. In a second paper by Glab and Qin the competition between autoionization and dissociation is observed starting from the same Rydberg states with an excited $v = 1$ core [38]. Here direct evidence is given for the nd-states to be responsible for predissociation.

To the best of our knowledge, no reports exist on the triplet $p-ungerade$ Rydberg states. Lindsay et al. have studied the nf-series using autoionization as probe [9]. They remark on the large effects of an external electric field up to 1000 Vcm^{-1}, which decreases the signal to a large extent. The accuracy of the wavelength scans in this

work allowed to detection of perturbations directly in line widths. It is of interest to note that also in the $nf-$series, perturbations are found for the Rydberg states with principal quantum number $n = 11$, 13, and 15. Like in this work, it has not been possible to identify the perturber state.

In conclusion, a series of reports exist on the spectroscopy of many Rydberg series in molecular hydrogen. In combination with Stark fields, most of the partial waves have been addressed experimentally. In spite of all this research, the decay mechanisms have only been touched often indirectly. Because of the importance of this decay channels for understanding dynamic processes such as dissociative recombination, it is of relevance to quantify the partial autoionization and dissociation decay widths of the different Rydberg series, triplet as well as singlet.

Bibliography

[1] W. Kołos and J. Rychlewski, J. Mol. Spectrosc. **66**, 428 (1977)

[2] W. Kołos and J. Rychlewski, J. Mol. Spectrosc. **143**, 237 (1990)

[3] L. Wolniewicz, J. Mol. Spectrosc. **169**, 329 (1995)

[4] A. Giusti, J. Phys. B **13**, 3867 (1980)

[5] A. Giusti-Suzor, and Ch. Jungen, J. Chem. Phys. **80**, 986 (1984)

[6] S. Ross, and Ch. Jungen, Phys. Rev. Lett. **59**, 1297 (1987)

[7] S. C. Ross and Ch. Jungen, Phys. Rev. A **49**, 4353 (1994)

[8] E. E. Eyler, R.C. Short, and F.M. Pipkin, Phys. Rev. Lett **56**, 2602 (1986)

[9] M.D. Lindsay, A.W. Kam, J.R. Lawall, P. Zhao, F.M. Pipkin and E. E. Eyler, Phys. Rev. A **41**, 4974 (1990)

[10] H. Rottke and K.H. Welge, J. Chem. Phys. **97**, 908 (1992)

[11] D. P. de Bruijn, and J. Los, Rev. Sci. Instrum. **53**, 1020 (1982)

[12] H. Helm, D. P. de Bruijn, and J. Los, Phys. Rev. Lett. **53**, 1642 (1984)

[13] E.E. Eyler and F.M. Pipkin, Phys. Rev. A **27,** 2462 (1983)

[14] R.D. Knight and L. Wang, Phys. Rev. Lett. **55**, 1571 (1985)

[15] R. Kachru and H. Helm, Phys. Rev. Lett. **55**, 1575 (1985)

[16] W.G. Sturrus, E.A. Hessels, P.W. Arcuni, and S.R. Lundeen, Phys. Rev. A **44**, 3032 (1991)

[17] Z.W. Fu, E.A. Hessels, and S.R. Lundeen, Phys. Rev. A **46**, 5313 (1992)

[18] A. Osterwalder, R. Seiler, and F. Merkt, J. Chem. Phys. **113**, 7939 (2000)

[19] N. Bjerre, S.R. Keiding, L.L. Lembo and H. Helm, Phys. Rev. Lett. **60**, 2465 (1988)

[20] L.J. Lembo, N. Bjerre, D.L. Huestis and H. Helm, J. Chem. Phys. **92**, 2219 (1990

[21] D.R. Bates, Phys. Rev. **78**, 492 (1950)

[22] D. Auerbach, R. Cacak, R. Caudano, T. D. Gaily, C.J. Keyser, J.M. McGowan, J.B.A. Mitchell and S.F.J. Wilk, J. Phys. B **10**, 3797 (1977)

[23] A. Giusti-Suzor, J.N. Bardsley and C. Derkits, Phys. Rev. A **28**, 682 (1983)

[24] H. Takagi, in *Dissociative Recombination: Theory, Experiment and Application IV* , ed. by M. Larsson, J.B.A. Mitchell and I.F. Schneider, (World Scietific, Eds, 1999), p.180.

[25] S.L. Guberman, J. Chem. Phys. **78**, 1404 (1983)

[26] B.K. Sarpal, J. Tennyson and L.A. Morgan, J. Phys. B **27**, 5943 (1994)

[27] D. Strasser, X. Urbain, H.B. Pedersen, N. Altstein, O. Heber, R. Wester, K. G. Bhushan and D. Zajfman, Rev. Sci. Instr. **71**, 3092 (2000)

[28] L.Dinu, A.T.J.B. Eppink, F.Rosca-Pruna, H.L.Offerhaus, W.J. van der Zande, M.J.J. Vrakking, Rev. Sci. Instr.**73**, 4206 (2002)

[29] E.E. Eyler and F.M. Pipkin, J. Chem. Phys. **77**, 5313 (1982)

[30] H.M. Crosswhite, *The Hydrogen Molecule Wavelength Tables of Gerhard Heinrich Dieke* (John Wiley & Sons, Inc., 1972)

[31] T.A. Miller, and R.S. Freund, J. Chem. Phys. **61**, 2160 (1974)

[32] K.P. Huber and G. Herzberg, *Constants of Diatomic Molecules* (Van Nostrand Reinhold, New York, 1979)

[33] F.T. Gallagher, *Rydberg Atoms* (Cambridge Univ. Press, 1994)

[34] J.N. Bardsley, J. Phys. B **1**, 349 (1968)

[35] A.I. Florescu, V. Ngassam, I.F. Schneider and A. Suzor-Weiner, J. Phys. B **36**, 1205 (2003)

[36] H. Takagi, J. Phys. B **26**, 4815 (1993)

[37] K. Qin, M. Bistransin, and W.L. Glab, Phys. Rev. A **47**, 4154 (1993)

[38] W.L.Glab and K. Qin, J. Chem. Phys. **99**, 2345 (1993)

Chapter 5

Study of photodetachment and photodissociation in O_2^-

Using fast beam photofragment spectroscopy, we have studied the competition between photodissociation and photodetachment in O_2^-. The photodissociation fraction is $\sim 10\%$ and increases somewhat between 285 and 266 nm. High resolution photofragment spectroscopy shows that the O_2^- beam is composed of $v = 0$ ions only. The photofragment angular distribution has an anisotropy parameter $\beta = 1.9$, indicating that the process of dissociation has a parallel character, attributed to the $A\ ^2\Pi_u \longleftarrow X\ ^2\Pi_g$ transition. A detailed analysis of the kinetic energy release of the photofragments shows structure related to the distribution over the 6 fine-structure dissociation limits $O^-(^2P_{3/2,1/2}) + O(^3P_{2,1,0})$. The results are compared with an analytical diabatic dissociation model taking into account the long range charge-quadrupole interactions; the $A\ ^2\Pi_u$ state is described in a Born-Oppenheimer electrostatic aproximation and projected onto the different fine-structure states at large internuclear separation using analytical expressions derived from the long range charge-quadrupole interactions between O^- and O fragments.

5.1 Introduction

The O_2^- is a stable molecular ion. It has an electron affinity of 0.43 eV [1,2]. From Raman spectroscopy and autodetachment experiments, the vibrational constant is determined to be 1090 cm^{-1} [3,4]. The addition of an extra electron to the $^3\Sigma_g^-$ electronic ground in the antibonding π_g orbital state weakens the chemical bond and increases the equilibrium separation from 1.2075 Å in O_2 to 1.346 Å in O_2^- [2,5]. The ground state of the anion is of inverted $^2\Pi_g$ symmetry with a fine-structure constant $A = -20 \pm 2$ meV [2]. In contrast to its neutral counterpart, the anion O_2^- has low lying excited states that are coupled to the ground state via allowed dipole transitions. In fact, the first excited state is the $A\ ^2\Pi_u$ state [6,7], which is bound with respect to the first dissociation limit $O(^3P_2) + O^-(^2P_{3/2})$. The significant difference between the electron affinities of the O_2 molecule (0.43 eV) and the O atom (1.461 eV) [8–10] shifts the threshold for the photodissociation of O_2^- with respect to that of O_2 from 243 nm (5.1 eV) to 304 nm (4.08 eV). In planetary atmospheres, the photodissociation of O_2^- may be both a source of oxygen atoms and ions. In addition to this, O_2^- is a far more efficient absorber of near UV radiation than neutral oxygen. The superoxide anion O_2^- is considered to be the most important anion involved in the negative ion chemistry in the lower ionosphere [11]. Together with the O^- anion, O_2^- is at the base of a chain of chemical reactions leading to more complex negative ions.

Whereas the photodetachment of O_2^- has been studied in great detail, providing absolute cross sections, photoelectron angular distributions, and the observation of resonant states [1–5,12–14], the photodissociation of O_2^- has not received much attention. To the best of our knowledge, the photodissociation of O_2^- was first observed by Vestal and Mauclaire [15] in a tandem quadrupole mass spectrometer. They reported a cross section of $4.2 * 10^{-19}$ cm^2 for the photodissociation of O_2^- into $O + O^-$ at 4.07 ± 0.07 eV. More recently, the photodissociation of O_2^- has been studied by Johnson and co-workers [4,16]. These studies extended the investigation to a wavelength range 3.5 - 5.6 nm and reported a 3% branching of dissociation relative to direct electron photodetachment. Furthermore, the angular distribution of the ejected O^- corresponds to an anisotropy parameter $\beta = 1.2 \pm 0.1$. These authors identified the $A\ ^2\Pi_u$ electronic excited state as being involved in the photodissociation process. Dissociative attachment studies ($O_2 + e^- \rightarrow O_2^{-*} \rightarrow O + O^-$) indicate a $^2\Pi_u$ state as intermediate state [17,18]. Also, theoretical studies on the potential energy curves of O_2^- paid special attention to the $A\ ^2\Pi_u$ state [6,19–21].

In the present study, we have applied high resolution fast beam photofragment spectroscopy on O_2^- molecular ions produced in a continuous hollow-cathode discharge ion source. The kinetic energy of the $O - O^-$ fragment pairs is determined with sufficient resolution to assign unambiguously the initial vibrational state of the O_2^- ions. The final kinetic energy of the fragments is affected by the fine-structure splitting of the $O_2^-(^2\Pi_{g,\Omega})$ ($\Omega = 3/2, 1/2$) ground state, and the fine structure splitting of the $O^-(^2P_{3/2,1/2})$ and the $O(^3P_{2,1,0})$ fragments. The highly structured kinetic

energy release (KER) spectrum makes it possible to estimate the branching over the six possible dissociation limits. The results are compared to a calculation assuming a diabatic model in the transition between the long range where the interaction energies are dominated by the charge-quadrupole interaction between the fragments to the asymptotic region where the atomic spin-orbit interaction dominates over the long range electrostatic interaction. The angular distribution of the O fragments has an anisotropy parameter $\beta = 1.9$, a value that it is considerably closer to 2 than previously reported. The competition between the photodetachment (PDE) and photodissociation (PDI) is determined by detecting the O_2 products from PDE and the O atoms from the PDI process on the same detector in pulse counting mode. We find PDI/(PDI+PDE) $\sim$ 10%. Clearly, the photodissociation of O_2^- and hence the formation of O^- at wavelengths less than 300 nm should not be ignored in ionospheric models.

5.2 Methods:

5.2.1 Experimental

A continuous molecular beam of O_2^- is extracted at 5 keV from a hollow-cathode discharge ion source. The discharge is maintained at 600 V and 20 mA. The temperature of the source is $\sim$ 350 K. We optimized the O_2^- signal by introducing molecular nitrogen in the discharge chamber. The most important reactions describing the production of negative molecular oxygen ions in the source are: $O_2 + O_2 + e \rightarrow O_2^- + O_2$ and $N_2 + O_2 + e \rightarrow O_2^- + N_2$. The superoxide ions O_2^- are mass selected by a Wien filter and introduced in a fast beam setup (see Fig. 5.1). By means of four deflection plates, the beam is guided through the apertures of the apparatus. Two Einzel lenses are used to focus the beam through the exit aperture of the ion source region and to reduce the radial size of the beam in the region of interaction with the laser.

The O_2^- anion beam is crossed perpendicular by ultraviolet laser radiation. The laser system used for this experiment consists of a 50 Hz Spectra Physics Nd-YAG laser pumping a Lambda Physik ScanMate dye laser. The 532 nm output of the Nd-YAG laser or the output of the ScanMate (around 560 nm) is frequency doubled in a BBO nonlinear crystal. The UV laser radiation (266 nm or 275-285 nm) is focused in the setup in a region of 1x1x1 mm^3 (x, y, z). The UV laser energy, measured after the interaction region is $\sim$ 2 mJ. The polarization of the laser is chosen to be parallel to the detector surface.

The photodetachment signal consists of neutral O_2 molecules flying in the same direction as the initial O_2^- beam. The photodissociation signal, on the other hand, consists of O and O^- fragments scattering out of the parent ion beam due to the kinetic energy released in the dissociation process. After a time-of-flight of $\sim$ 7 μs the fragments reach a detector consisting of two microchannelplates (MCPs) and a

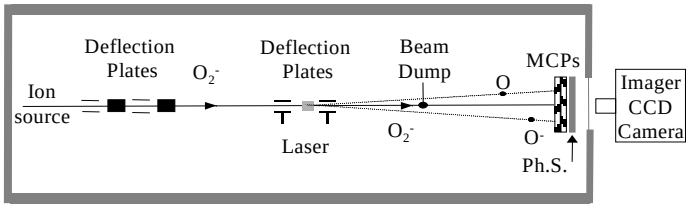

Figure 5.1: *Scheme of the experimental setup. A continuous molecular ion beam of O_2^- is crossed with a 25 Hz laser pulse (275-285 nm). PDE and PDI occur leading to O_2, O and O^- fragments. The use of the beam dump is optional as well as the deflection plates after the laser interaction region. The double exposure camera detects position (x and y-coordinates) and the relative arrival time difference of the fragments onto the MCP's.*

P46-phosphor screen. Outside the vacuum system, a double exposure CCD camera (LaVision, modified Imager3 VGA) records the images of the phosphor screen, from which the positions (x, y) and arrival time t of the detected fragments are obtained [22,23]. In brief, the camera records the image of the phosphor screen and the intensity of the spots corresponding to individual particles. Due to the fast interline transfer of the CCD chip, the camera is capable of taking two successive images of the same phosphor decay for each event that originates from a single laser pulse. Subsequently, the arrival time is deduced for each event from the ratio of intensities measured in both images [24]. Therefore, this camera retrieves not only the (x, y) coordinates of the spots ($\sim$ 80 μm resolution) but also the arrival time of the particles ($\sim$ 1 ns resolution).

The positions and arrival time difference between the two fragments resulting from a dissociation event are used to determine the orientation of the molecule during the dissociation process and to calculate the kinetic energy released in the process. Multiple dissociation events per laser shot can be detected, since coincident fragments have a centre-of-mass position in the middle of the detector. The camera is the master clock of the experiment. It controls the firing of the laser and it limits the acquisition rate to 25 Hz.

5.2.2 Theory: a diabatic model for the correlated fine-structure branching ratios

The Franck-Condon region of the ground state of the O_2^- ion is well described by adiabatic Born Oppenheimer (ABO) potentials, i.e., determined by the eigenvalues of the usual Coulomb Hamiltonian $\hat{H}_{coul}$. In this region, the projection of the electronic

orbital angular momentum on the molecular axis (Λ) is a good quantum number. The fine-structure splittings are much smaller than the binding energies derived in the ABO potentials. Since $\hat{H}_{coul}$ does not contain the spin, all the ABO states correlating with the $O^-(^2P) + O(^3P)$ dissociation limit are asymptotically degenerate. Near the dissociation limit at the long range, the spin-orbit coupling $\hat{H}_{SO}$ dominates the interaction amongst these states. Between the Franck-Condon region and the asymptotic region, a region exists, in which the charge-quadrupole, ion-atom interaction between the fragments is still significantly larger than the asymptotic atomic fine-structure interactions.

In the case of dissociation at very small recoil velocity the atomic fine-structure branching is best described by a spin-orbit adiabatic correlation diagram with Hund's case-c potentials. These potentials follow from the eigenvalues of $\hat{H}_{coul} + \hat{H}_{SO}$. The associated eigenfunctions are labeled by Ω, the projection of the total electronic angular momentum on the molecular axis, rather than Λ. Since the $A\ ^2\Pi_{u,3/2}$ and $A\ ^2\Pi_{u,1/2}$ states are the lowest $^2\Pi_u$ states for $\Omega = 3/2, 1/2$, respectively, they both correlate with the lowest $O^-(^2P_{3/2}) + O(^3P_2)$ limit. However, at the wavelengths used in this experiment, the recoil kinetic energy (approximately 500 meV) is much larger than the atomic fine-structure energy differences. Thus, this adiabatic model does not necessarily apply in the energy regime of our experiment.

In the high energy limit a diabatic or sudden model is expected to apply. The long range states are derived from a correlation diagram for the ABO states. In the present case, it is assumed that in the long range the molecular potentials are well described by the charge-quadrupole interaction. The diabatic wave function is projected onto a basis of product atomic fine-structure states in order to obtain the atomic fine structure distribution. A problem treating molecular dissociation to asymptotic fine-structure states was worked out with a similar analytic diabatic model for the photodissociation of neutral O_2 in the Herzberg region [29,30]. A similar treatment has been used in the experimental paper of Leahy *et al.* [31], which was based on the theory from Singer *et al.* [32].

The present treatment is different in two ways from the earlier. Dealing with an anion, the leading long range term is the charge-quadrupole interaction, which is stronger than the quadrupole-quadrupole interaction as for example in neutral O_2. Secondly the use of the long range interactions makes the full treatment analytical without using empirical parameters, as in Ref. [31,32].

Using the notation of Ref. [30] we express the orbital part of the ABO functions in the long range as product atomic wave functions

$$|l_a \lambda_a\rangle \, |l_b \lambda_b\rangle \,, \tag{5.1}$$

where the subscript a refers to the O^- ion and b to the neutral O atom, $l_a = l_b = 1$, and $\Lambda = \lambda_a + \lambda_b = 1$ for Π states. The neutral O_2 ABO states can be obtained by a

Clebsch-Gordon coupling of the atom states. However, for O_2^- it is more convenient to work in the uncoupled basis, since the charge-quadrupole interaction $V^{(0,2)}$ lifts the degeneracy of the $|11\rangle\,|10\rangle$ and $|10\rangle\,|11\rangle$ states and the off-diagonal matrix element between the states is zero.

A complication arises from the fact that two $^2\Pi_u$ states exist for each value of Ω correlating with the $O^-(^2P)+O(^3P)$ limit. In order to determine the wave function for the lowest state, i.e., the one correlating with the A state, we must consider the leading nonvanishing long range term in the multipole expansion of $\hat{H}_{coul}$. A calculation shows that the $|10>|11>$ state, i.e., the state with $\lambda_O = 1$, is the lowest. This can be readily understood qualitatively, since the $2p$ shell electron configurations of the $O(^3P)$ atom for $\lambda_O = 1$ and $\lambda_O = 0$ are $|p_{-1}p_0p_1\overline{p_1}|$ and $|p_{-1}p_0\overline{p_0}p_1|$, respectively. The $\lambda_O = 0$ configuration is higher in energy, since it has an extra electron in the p_0 orbital, which is pointing towards the O^-.

The ABO wave function is completed by adding a Clebsch-Gordon coupled atomic spin part (see Ref. [29])

$$|S\Sigma\rangle = \sum_{\sigma_a\sigma_b} |s_a\sigma_a\rangle\,|s_b\sigma_b\rangle\,\langle s_a\sigma_a s_b\sigma_b|\,S\Sigma\rangle, \tag{5.2}$$

where for the $A^2\Pi_\Omega$ states in the $^2P+^3P$ limit we have $S = 1/2, s_a = 1/2, s_b = 1$, and $\Sigma = \Omega - \Lambda$. Following Ref. [30] the product atomic fine-structure states are written as $|j_a\omega_a j_b\omega_b\rangle = |j_a\omega_a\rangle\,|j_b\omega_b\rangle$ with

$$|j_i\omega_i\rangle = \sum_{\lambda_i\sigma_i} |l_i\lambda_i\rangle\,|s_i\sigma_i\rangle\,\langle l_i\lambda_i s_i\sigma_i|\,j_i\omega_i\rangle, \quad i = a, b. \tag{5.3}$$

It is now straightforward to compute the transformation matrix elements

$$\langle j_a\omega_a j_b\omega_b|\,l_a\lambda_a l_b\lambda_b S\Sigma\rangle = \sum_{\sigma_a\sigma_b} \langle l_a\lambda_a s_a\sigma_a|\,j_a\omega_a\rangle\,\langle l_b\lambda_b s_b\sigma_b|\,j_b\omega_b\rangle\,\langle s_a\sigma_a s_b\sigma_b|\,S\Sigma\rangle, \tag{5.4}$$

and the fine-structure branching coefficients $P_{j_a,j_b}^{(\Omega,\lambda_a,\lambda_b)}$ are obtained as

$$P_{j_a,j_b}^{(\Omega,\lambda_a,\lambda_b)} = \sum_{\omega_a\omega_b} |\,\langle j_a\omega_a j_b\omega_b|\,l_a\lambda_a l_b\lambda_b S\Sigma\rangle|^2. \tag{5.5}$$

The results from the last equation are compared to the experimental results and to a purely statistical model in which the statistical multiplicity is assumed to describe the fine-structure distribution.

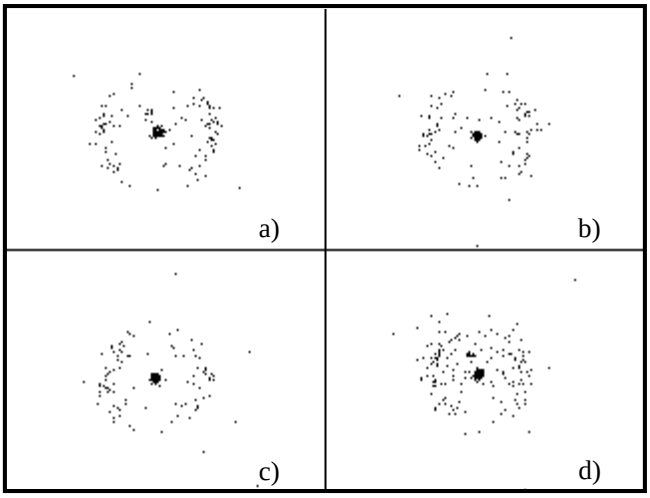

Figure 5.2: *2D detection of PDE and PDI neutral fragments. The ions (O_2^- and O^-) are deflected away after the laser interaction region and the beam dump is removed. The O_2 fragments from PDE are detected in the central part of the image. The diffuse distribution of particles are O neutrals from PDI. a) 275 nm; b) 279 nm; c) 282 nm; d) 285 nm;*

5.3 Results

5.3.1 Photodissociation versus photodetachment rate

As was shown before [16], for excitation energies larger than 4.08 eV the dissociation channel opens and the issue of the competition between electron detachment and photodissociation is relevant. Previous work showed a branching ratio of 3% between the two processes (3% PDI versus 97% PDE) [16] in the range of 4.5 eV.

In order to estimate the dissociation versus detachment branching ratio, we have detected the O_2 molecules and the O fragments on the same detector. We employ a 600 V/cm electric field to deflect the parent ion beam after the interaction with laser. This way we ensure that the only fragments that reach the detector are neutral species. By removing a beam dump, the neutral O_2 products are detected in the centre of the detector. We found virtually no signal in the absence of the laser light.

Figure 5.2 shows a sample of four data sets recorded at different laser wavelength between 275 nm and 285 nm. The particles detected in a confined region (10x10 pixels) in the centre of the detector are neutral O_2 products from the photodetachment process. The fragments found outside this small region are O fragments from

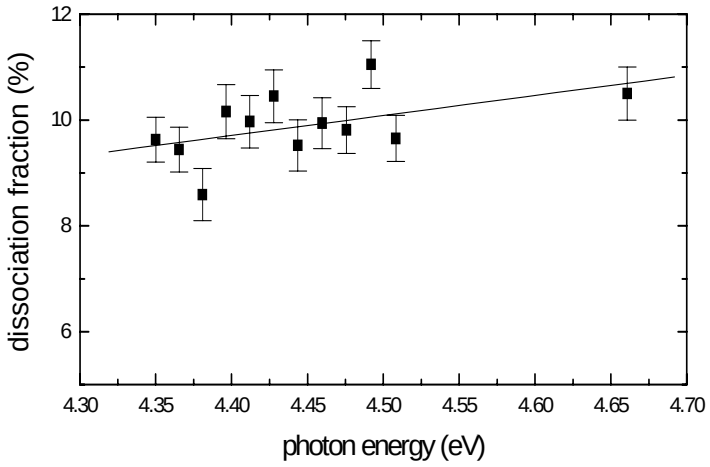

Figure 5.3: *Fraction of dissociation versus excitation energy. The dissociation fraction is defined as number of O fragments versus total number of detected particles (O and O_2).*

the photodissociation process. Figure 5.2 shows that the radius of the O fragment distribution, which is a measure of KER in the dissociation process, increases with photon energy, as expected.

We measured the branching ratio of the two processes over the wavelength region of 266-285 nm. The results are plotted in Fig. 5.3. Detecting both species, O and O_2 on the same detector in a pulse counting mode, makes this result insensitive to small gain differences in the detection of both species. The mean value of the branching ratio is 10%. A linear fit reveals a slight increase in the photodissociation efficiency to higher photon energies.

5.3.2 The angular distribution

A second experiment has been performed at 266 nm (4.66 eV) focusing on the photodissociation process itself. This experiment uses coincidence fragment detection, i.e., the photodissociation products O and O^- are recorded in coincidence. A beam dump is placed 20 cm away from the laser interaction region in order to avoid saturation of the central part of the detector, where the main negative ion beam arrives. The beam dump also blocks the neutral O_2 products from the photodetachment process.

The raw (x, y) data, as recorded by the camera over 20000 laser shots at 266 nm,

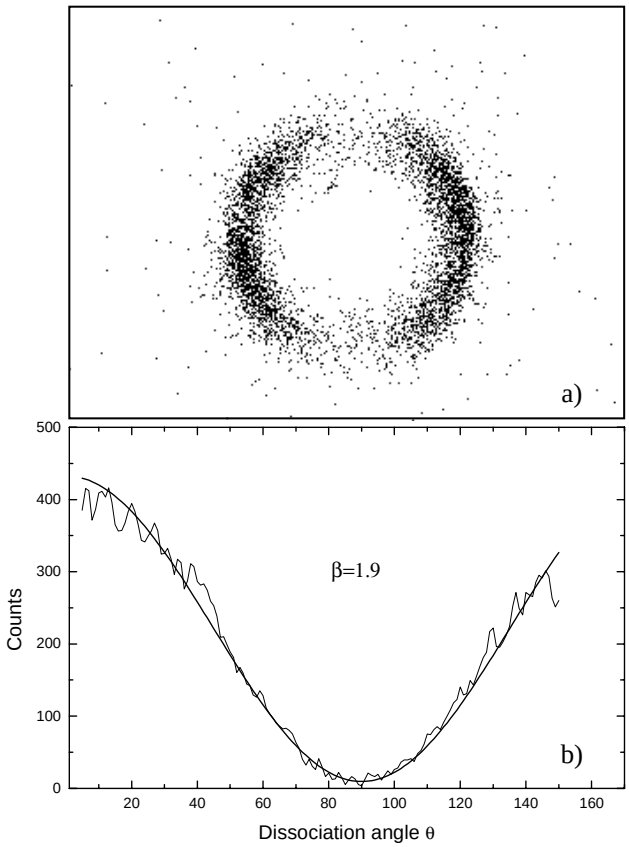

Figure 5.4: *a) Sample of raw (x,y) data recorded over 20 000 laser shots at 266 nm. The detection is performed in coincidence ($O + O^-$). The parent O_2^- beam is stopped by the beam dump. The arrow indicates the polarization of the laser; b) The angular distribution of the fragments. Fitting the histogram (thick curve) the anisotropy parameter $\beta = 1.9$ is obtained.*

is shown in Fig. 5.4(a). In this figure, each photodissociation event is represented by two dots on opposite sides of the centre of the image. Only one ring is present; it corresponds to one-photon transitions from the ground state $X^2\Pi_g(v=0)$ to the continuum of the $A^2\Pi_u$ state generating $O(^3P) + O^-(^2P)$ fragment atoms.

The dissociation process is a direct and fast process via a $A^2\Pi_u \longleftarrow X^2\Pi_g$ parallel transition. To verify this, the angular distribution of the fragments on the detector has been investigated. We recall here the expression for molecular dissociation using linearly polarized light:

$$I(\theta) = \frac{1}{4\pi}[1 + \beta(\tau)P_2(\cos\theta)]. \tag{5.6}$$

Here τ stands for the lifetime of the dissociative state and $\mathrm{P}_2(\cos\theta) = \frac{3}{2}\cos^2(\theta) - \frac{1}{2}$. For a direct dissociation process $\beta_\parallel(\tau = 0) = 2$ or $\beta_\perp(\tau = 0) = -1$, reflecting the character of the transition. In Fig. 5.4(b) a histogram of the angular distribution of the particles is shown. For each pair of fragments (O and O^-) detected in coincidence and recognized as resulting from the same parent O_2^- by centre-of-mass selection, we express the angle θ as the angle between laser polarization and the internuclear axis. The histogram shows a sudden decrease of signal around 165 degrees. This is an unfortunate consequence of the presence of the beam dump; the angular region from 150 to 175 degrees is hidden by the holder of the beam dump (data not shown). The solid curve is the best fit of the histogram (ignoring the region mentioned above). We have used for the fit the function expressed in Eq. (5.6). The anisotropy parameter β derived from the fit equals 1.9 ± 0.02, where the error gives the fitting uncertainty. Uncertainties on the absolute background level implies that our result is not inconsistent with $\beta = 2$. This result supports very well the belief that the dissociation happens via a $A^2\Pi_u \longleftarrow X^2\Pi_g$ parallel transition.

5.3.3 Experiment: the fine-structure at the dissociation limit

In our experiment, the full kinematics of the dissociation process are obtained via a three-dimensional coincidence detection. This information makes possible the identification of the initial state as well as the fine-structure of the dissociation limit, by means of KER spectra. For each coincidence event KER is calculated:

$$KER = \frac{E_0}{4L^2}(D^2 + v_0^2\Delta t^2), \tag{5.7}$$

where E_0 is the kinetic energy of the parent beam (5 keV), L is the length of the flight tube from the region where dissociation takes place to the detector, D is the distance measured on the detector between the two fragments, Δt is the arrival time difference of the particles and v_0 is the velocity of the parent beam. Figure 5.5 shows a histogram

of the observed KER distribution. As the spatial resolution of the apparatus is better than the temporal one, the resolution of the KER determination is increased by employing further selection of events. We select only events with a minimum time difference and a maximum spatial separation. These events are dissociations in the plane parallel to the detector. The observed KER values in the broad peak reveal that photodissociation starts from different rotational and fine-structure levels of the ground state $X\ ^2\Pi_g(v=0)$, leading to the $O(^3P_{2,1,0})+O^-(^2P_{3/2,1/2})$ limits. The near absence of a $v=1$ dissociation peak around 670 meV as well as $v=2$ dissociation peak around 800 meV reveals the absence of $X^2\Pi_g(v=1,2)$ levels in the initial ion beam or a dissociation probability that decreases very strongly with the vibrational quantum state, which is not very likely. This result is surprising in view of the expected stability of $O_2^-(v=1)$ and $O_2^-(v=2)$ states.

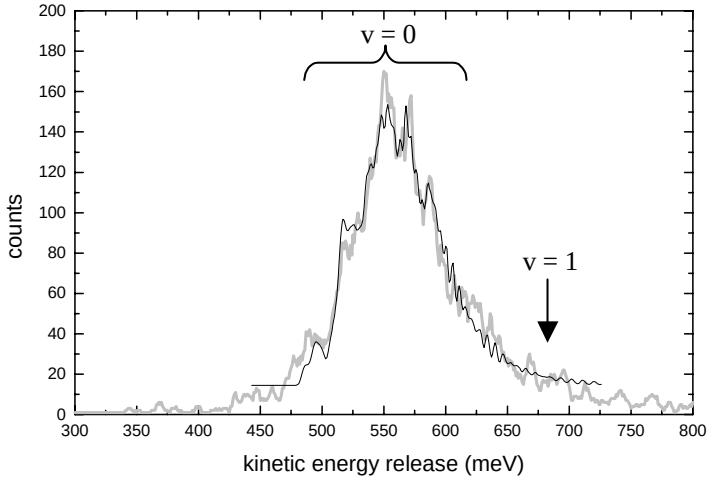

Figure 5.5: *The KER spectrum (thick grey curve) shows a broad but structural feature around 550 meV associated with transitions from* O_2^- $(X\ ^2\Pi_{g,\Omega})$ $(\Omega = 3/2, 1/2)$ *(*$v=0$*) states and leading to the* $O(^3P_{2,1,0})+O^-(^2P_{3/2,1/2})$ limits. *No photofragments starting from* O_2^- *(*$v=1$*) are observed. The fit (thin black curve) is a linear superposition of 12 possible fine-structure transitions and the background line. The results of the fit are presented in Table II.*

The superoxide ion has two spin-orbit ground states $O_2^-(X\ ^2\Pi_{g,\Omega})$ $(\Omega = 3/2, 1/2)$, which are split by $A = -20 \pm 2$ meV [2]. The lowest ground state is $O_2^-(^2\Pi_{g,3/2})$. The dissociation limit $O(^3P_j)+O^-(^2P_{j-})$ in fact forms a manifold of 6 dissociation limits. The fine structure splitting of $O(^3P_{2,1,0})$ is accurately known ($< 10^{-4}$ cm^{-1}) from laser magnetic-resonance experiments [25, 26]. The $^3P_1$ and $^3P_0$ levels are 19.65 eV

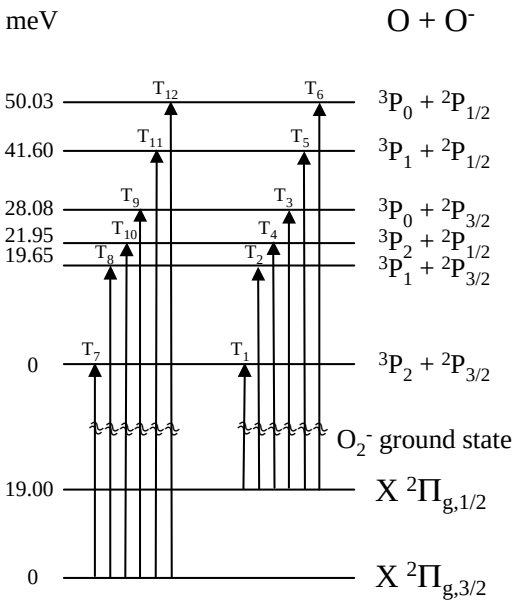

Figure 5.6: *The diagram shows the fine-structure of the ground state of O_2^- and of the dissociation limit ($O + O^-$). The arrows indicate the transitions used in the fitting of the KER spectrum. The relative energies are expressed in meV.*

and 28.08 eV, respectively, above the $^3P_2$ level. For the $O^-(^2P_{3/2,1/2})$ fine structure splitting, we have used the latest high precision result 177.084(14) cm^{-1}(21.95 meV), which has been obtained using photodetachment microscopy [10]. Figure 5.6 shows 12 possible transitions and relative energies of the fine-structure states used in the simulation of the KER spectrum.

The transition T_{12} originating from O_2^- $X\ ^2\Pi_{g,3/2}$ and ending on the dissociation limit $O(^3P_0)+O^-(^2P_{1/2})$ does not conserve the projection of total angular momentum exclusive of nuclear spin on the molecular axis, but it is considered in the fit and found to contribute. The rotational population of the anion ground state of $O_2^-(X\ ^2\Pi_g)$ is assumed to obey a thermal distribution. Considering the temperature of the ion source $T = 350$ K and the rotational constant $\beta_e = 1.16$ cm^{-1}, up to $R = 35$ rotational states are populated. The shape of each transition used in the fitting of the KER spectrum is

$$T_i(\Omega, j, j^-, x) = \sum_R (2R+1) * e^{\frac{-\beta_e R(R+1)}{kT}} * e^{\frac{-(x-KER)}{2\sigma^2}} \tag{5.8}$$

KER is the kinetic energy release taking into account the initial rotational state and the different asymptotic channels as defined by R, Ω, j and j^-. The KER resolution of the detector and imaging equals ($\sigma = 2$ meV). The Earth's magnetic field as well as stray electric fields affect the trajectories of the charged O^-. We actively compensate for this effect by employing a small electric field. Nevertheless, a small residual shift remains: $d \sim 400$ μm. Since the O and O^- fragments cannot be distinguished on the detector, the effect of magnetic field appears as an apparent splitting of each KER peak, one at KER corresponding to a distance between fragments $D-d$ and the other one at KER corresponding to a distance $D+d$. The splitting is ~ 31 meV. This effect is included in the shape of the transitions considered in the fit. The calculated maxima of the KER distribution for each transition, ignoring this instrumental complication, are presented in Table I.

Table I The diabatic and statistical model for the branching over the 12 transitions

Transitions	Ω	j	j^-	KER[a] meV	diabatic %	statistical %
T_1	1/2	2	3/2	573	0.1852	0.3704
T_2	1/2	1	3/2	553	0.3333	0.2222
T_3	1/2	0	3/2	545	0.1481	0.0741
T_4	1/2	2	1/2	551	0.0926	0.1852
T_5	1/2	1	1/2	531	0.1667	0.1111
T_6	1/2	0	1/2	523	0.0741	0.0370
T_7	3/2	2	3/2	554	0.5556	03704
T_8	3/2	1	3/2	534	0.1111	0.2222
T_9	3/2	0	3/2	526	0	0.0741
T_{10}	3/2	2	1/2	532	0.2778	0.1852
T_{11}	3/2	1	1/2	512	0.0556	0.1111
T_{12}	3/2	0	1/2	504	0	0.0370

[a] The maximum of the calculated KER distribution corresponding to a photon energy of 4.66 eV.

Not all of the 12 combinations (see Table I) of the two molecular ground states and the six dissociation limits, T_i, are individually resolved. Only seven groups of lines, G_i, are distinguished (see Table II). For example, transitions T_5, T_8 and T_{10} corresponding to almost the same KER are grouped together and taken into account in the fit as one line, G_4.

Table II Fit coefficients for the branching

Obs. Lines	Transitions	Fit coefficients %	diabatic %	statistical %
G_1	T_{12}	0.06 ± 0.01	0	0.0185
G_2	T_{11}	0.08 ± 0.01	0.0278	0.0555
G_3	$T_6 + T_9$	0.06 ± 0.03	0.0370	0.0555
G_4	$T_5 + T_8 + T_{10}$	0.33 ± 0.02	0.2778	0.2592
G_5	T_3	0.02 ± 0.03	0.0740	0.0370
G_6	$T_2 + T_4 + T_7$	0.29 ± 0.03	0.4907	0.3889
G_7	T_1	0.16 ± 0.03	0.0926	0.1852

In the simulation of the KER spectrum we have used a least square linear fitting routine. The input matrix consists of the 7 KER distributions representing the 12 transitions, G_i. A small constant background is added to account for the minor fraction of accidental coincidences. The detection of multiple coincidences per laser shot opens the possibility of recording accidental coincidences; an incorrect combination of two fragments coming from different dissociation events but having an apparent centre-of-mass in the region of acceptance for true coincidences. The best fits were obtained using 19 meV for the fine-structure splitting in the superoxide anion ground state. We note that the observed structures in Fig. 5.5 could only be consistently fitted using the known energy differences between the dissociation limits and the known instrumental parameters. This observation corroborates the origin of the observed structure in the KER peak. The error bars have been determined by fitting 100 realizations of the spectrum while changing the spectrum randomly within the statistical uncertainty per channel, on top of determining the sensitivity of the fit results towards changes in other parameters, such as the 19 meV fine-structure splitting, and the rotational temperature in the range of $T_r^{fit} = 300 \div 350$ K. We find that the data are best described limiting the fine-structure splitting to 19 ± 1.5 meV.

Table I also shows the calculated, theoretical results using the diabatic model described above, as well as the results of a simple statistical model. A fully adiabatic dissociation would result in population of the first dissociation limit, $O(^3P_2)+O^-(^2P_{3/2})$, only. With respect to the calculations, we note that the results of the diabatic model predict a significant larger population of the excited $O(^3P_J)$ states than the statistical in the case of the superoxide anion ground state, whereas the reverse is the case starting from the excited O_2^- ($\Omega = 1/2$) anion state. As can be deduced from Table I, the sum of the diabatic predictions, starting from the two molecular states and leading to a certain dissociation limit are identical to the statistical prediction. This remarkable observation cannot be general, since a necessary condition for this observation is that the selection rules allow the molecular state to connect to all possible dissociation limits. Certain allowed molecular symmetries do not meet this condition. At this moment, we have no explanation of this effect.

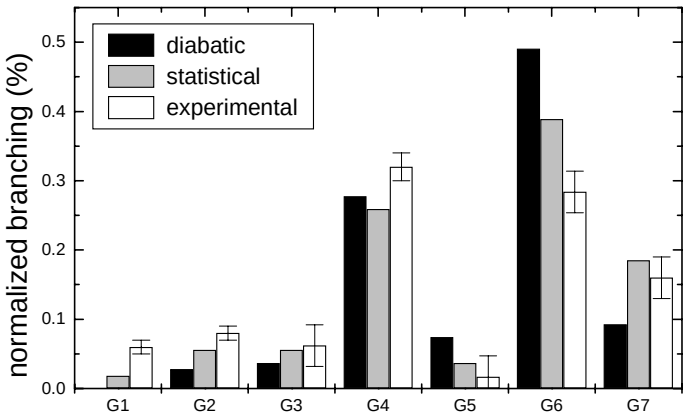

Figure 5.7: *The experimental branchings over the 7 groups of transitions (white columns) are compared with a diabatical calculation (black columns) and the statistical model (grey columns).*

Table II and Figure 5.7 show the comparison between the experimentally deduced branchings and the theoretical ones. Here some individual transitions have been grouped as described above. Note that the groups are numbered with increasing KER value, whereas the transitions are numbered as described in Table I. The experimental results are represented by the fit coefficients. For the comparison, we have adopted equal populations for both molecular fine-structure states. Unfortunately, we cannot deduce this population ratio directly from the data. We note that no *a priori* information has been used in the experimental fit. A very nice agreement is found between the calculated and predicted trends in the branching. The superoxide anion clearly does not dissociate adiabatically. It is, however, difficult to distinguish between the diabatic and the statistical model. Finally, we note that we observe a small contribution for G_1. This dissociation pathway does not conserve the projection Ω in going from the molecule ($\Omega = 3/2$) to the highest dissociation limit, $O(^3P_0) + O^-(^2P_{1/2})$ with total $\Omega = 1/2$.

5.4 Discussion

5.4.1 Photodetachment mechanism

We have found a dissociation fraction of approximately 10% slowly increasing with photon energy over a wavelength region between 285 and 266 nm. We have established that the dissociation process starts from O_2^- X $^2\Pi_{g,1/2,3/2}(v = 0)$ states only and that it takes place via the continuum of $A^2\Pi_u$, based on the anisotropy parameter. Finally, we have obtained information on the correlated product state information. First, we will discuss the photodetachment process, which can proceed via a number of pathways, both direct and indirect.

$$
\begin{aligned}
O_2^-(X^2\Pi_g) + h\nu &\rightarrow O_2(X^3\Sigma_g^-, a^1\Delta_g, b^1\Sigma_g^+) + e^-, && (5.9)\\
&\rightarrow O_2(c^1\Sigma_u^-) + e^-, && (5.10)\\
&\rightarrow O_2^-(A^2\Pi_u) \rightarrow O_2(X^3\Sigma_g^-, a^1\Delta_g, b^1\Sigma_g^+) + e^-, && (5.11)\\
&\rightarrow O_2^-(A^2\Pi_u) \rightarrow O_2(c^1\Sigma_u^-) + e^-. && (5.12)
\end{aligned}
$$

where Eqs. (5.9) and (5.10) refer to direct processes while Eqs. (5.11) and (5.12) refer to indirect processes, better described as autodetachment of the photoexcited intermediate $O_2^-(A^2\Pi_u)$ state. Two processes, Eqs. (5.10) and (5.12), have their energetic threshold at $\lambda \sim 275$ nm. The dominant valence electron configurations of the states involved are: $\pi_u^4\pi_g^3$ for the $O_2^-(X^2\Pi_g)$ state, $\pi_u^4\pi_g^2$ for the $O_2(X^3\Sigma_g^-, a^1\Delta_g, b^1\Sigma_g^+)$ states; $\pi_u^3\pi_g^3$ for the $O_2(c^1\Sigma_u^-)$ state; and $\pi_u^3\pi_g^4$ for the $O_2^-(A^2\Pi_u)$ state [6]. Eq. (5.9), Eq. (5.10) and Eq. (5.12) are one-electron processes; Eq. (5.11) is indirect and involves a two-electron process in the autodetachment step. Eq. (5.12) is the result of two one-electron processes, but has a very small Franck-Condon overlap in the autodetachment step at our excitation energies.

An absolute determination of the efficiencies of these pathways is not easy. The observed photodissociation fraction may reflect the relative cross sections of direct photodetachment and molecular excitation. However, a photodetachment signal due to autodetachment of the excited molecular anion state cannot be ruled out based on our observations. The measurements of the branching fraction, fine-structure distribution and anisotropy presented here do not contain direct information on the origin of the observed branching fraction. Bailey *et al.* concluded from studying autodetachment studies via bound vibrational levels in the $O_2^-(A^2\Pi_u)$ state that the absorption cross section to this state may well be equal to the photodissociation cross section [4]. The observation of vibrational structure in this experiment is suggestive for autodetachment lifetimes being much longer than a vibrational period. As a consequence, upon excitation molecular dissociation would be much faster than autodetachment.

In fact, an electron energy spectrum of the photodetached electrons could be more revealing in this respect. Autodetachment via the dissociative $O_2^-(A^2\Pi_u)$ state should

result in a change in the Franck-Condon factors with different product neutral O_2 vibrational levels. We have not found measurements in the literature in this direction. Further, it is of interest to note that the photodissociation branching does not change upon energetically opening of the reaction channels associated with Eqs. (5.10) and (5.12). Opening of these channels could increase the relative autodetachment rate and decrease the dissociation fraction.

Theory is more revealing in unraveling the different mechanisms. Recently, multichannel scattering calculations were performed [5], providing cross sections for the photodetachment of O_2^- leading to O_2 for photon energies up to 50 eV. Since this theoretical work was performed using a fixed nuclei approximation, the cross sections should be seen as total absorption cross sections. The distribution of the total cross section shows an overall smooth increase for photon energies up to 20 eV followed by a smooth and slower decrease towards an energy of 50 eV. The only prominent structure is a resonance appearing at photon energies between 5 and 6 eV (the cross section increases locally by a factor of four, up to $15 \div 20 * 10^{-18}\ cm^2$). The resonance has the configuration of $1\pi_u^3 1\pi_g^4$ [5] and it is attributed to the $O_2^-(A^2\Pi_u)$ state. Our experiment was performed in a wavelength region (4.35 - 4.66 eV) and the total theoretical cross section should be around $4.5 * 10^{-18} cm^2$. The main contributions to this cross section are processes of Eq.(5.9) ($\sim 2 * 10^{-18}\ cm^2$ for $O_2(X^3\Sigma_g^-) \leftarrow O_2^-(X^2\Pi_g)$, $\sim 1.5 * 10^{-18}\ cm^2$ for $O_2(a^1\Delta_g) \leftarrow O_2^-(X^2\Pi_g)$, $\sim 1 * 10^{-18}\ cm^2$ for $O_2(b^1\Sigma_g^+) \leftarrow O_2^-(X^2\Pi_g)$). All three partial cross section distributions in the eleven-channel calculation leading to $O_2(X^3\Sigma_g^-, a^1\Delta_g, b^1\Sigma_g^+)$ states show the same resonance around 5 eV. The resonance has a configuration of $1\pi_u^3 1\pi_g^4$ and it is attributed to the $O_2^-(A^2\Pi_u)$ state. Our experiment probes the low energy wing of this resonance. It is tempting to interpret the small increase in photodissociation fraction as the increase of this resonance. This would imply that at these energies the $O_2^-(A^2\Pi_u)$ state, once populated, decays mainly via dissociation processes, and it accounts for the high dissociation rate of 10%.

The contribution of the $O_2(c^1\Sigma_u^-) \leftarrow O_2^-(X^2\Pi_g)$(see Eq. (5.10)) is small in this wavelength region, as well as the contribution of Eq. (5.12) (according to the one channel calculation, the maximum cross section of this reaction is obtained for a photon energy of 10 eV). The rest of the states taken into account in this theoretical work show various maxima for photon energies higher than 10 eV and do not contribute significantly to the total cross section for photon energies below 5 eV.

As the photodetachment mechanism is likely to be dominated by direct one photon process as well, we describe our experiment by:

$$\begin{aligned} O_2^-(X^2\Pi_g) + h\nu(266 - 285nm) &\rightarrow O_2(X^3\Sigma_g^-, a^1\Delta_g, b^1\Sigma_g^+) + e^-, (\sim 90\%) \\ &\rightarrow O_2^-(A^2\Pi_u) \rightarrow O(^3P_j) + O^-(^2P_j), (\sim 10\%) \end{aligned} \quad (5.13)$$

It is tempting to conjecture that at the peak of the 5 eV resonance, photodissociation may even dominate over photodetachment [5]. A preliminary experiment

at a photon wavelength of 212 nm (5.8 eV) did not show any increase in the photodissociation fraction. The 212 nm has been obtained by frequency mixing of the fourth harmonic of the Nd:YAG (266 nm) with the fundamental wavelength of the same laser (1064 nm). It is possible that at this increased energy the autodetachment process via the $O_2(c^1\Sigma_u^-)$ state has increased significantly in strength, reducing the photodissociation rate.

5.4.2 The fine-structure of the dissociation limit

Understanding the dissociation dynamics of diatomic molecules implies being able to predict the distribution over the different fine-structure states. This type of research has not received a lot of attention because of the relatively small number of experiments that could be performed at this level of detail. With the improvements in ion imaging techniques, such as velocity map imaging [33], experiments at this detail for important atmospheric molecules may well become possible, see for example Ref. [**?**] on molecular oxygen. Using velocity map imaging, no correlated fine-structure information in the case of oxygen has been reported.

Coincident fast beam photofragment techniques have been able to obtain quantitative correlated information on the atomic fine-structure states employing the aspect of coincident detection. The experiment reported by Leahy *et al.* is an excellent example of how coincidence experiments can reveal details of the photodissociation of molecular oxygen via the Schumann-Runge states [31]. The complexity of the Schumann-Runge predissociation process and the fact that their theory required a small number of fitting parameters, makes it harder to draw firm conclusions. The present study of the superoxide anion is a favorable case for theoretical calculations. The dissociation process involves one dominant molecular state and the description of the charge-quadrupole interaction makes it possible to generate a diabatic model without any parameter. The experimental resolution reached in the present experiment was not sufficient to determine accurate branching fractions that can be compared quantitatively. The data show that dissociation is far from adiabatic and much closer to diabatic and statistical models. The presence of dissociation fragments at the channel that does not conserve Ω in the dissociation can not be explained within the present diabatic model.

The importance of the superoxide anion in atmospheric sciences resides dominantly in the chemistry in the upper atmosphere. In this region, the UV flux is intense. The reported 10% photodissociation should not be neglected in ionosphere models. Photodissociation of the superoxide anion is a source of the atomic anion, which may play a role in the upper atmosphere.

Bibliography

[1] R.J. Celotta, R.A. Bennet, J.L. Hall, M.W. Siegel, and J. Levine, Phys. Rev. **5,** 631 (1972)

[2] M.J. Travers, D.C. Cowles, and G.B. Ellison, Chem. Phys. Lettters **164,** 449 (1989)

[3] J. Rolfe, W. Holzer, W.F. Murphy, and H.J. Bernstein, J. Mol. Spectrosc. **26**, 543 (1968)

[4] C.G. Bailey, D.J. Lavrich, D. Serxner, and M.A. Johnson, J. Chem. Phys. **105**,1807 (1996)

[5] P. Lin and R.R. Lucchese, J.Chem. Phys. **114**, 9350 (2001)

[6] M. Krauss, D. Neumann, A.C. Wahl, G. Das, and W. Zemke, Phys. Rev. A **7**, 69 (1973)

[7] K.P. Huber and G. Herzberg, *Molecular Spectra and Molecular Structure: Constants of Diatomic Molecules* (Van Nostrand-Reinhold, New York, 1979)

[8] H. Hotop and W.C. Lineberger, J. Phys. Chem. Ref. Data **4**, 539 (1975)

[9] D.M. Neumark, K.R. Lykke, T. Andersen, and W.C. Lineberger, Phys. Rev. A **32,** 1890 (1985)

[10] C. Blondel, C. Delsart, C. Valli, S. Yiou, M.R. Godefroid, and S. Van Eck, Phys. Rev. A **64**, 052504 (2001)

[11] R.W. Schunk and A.F. Nagy, *Ionospheres- Physics, Plasma Physics and Chemistry*, (Cambridge, 2000)

[12] D.S. Burch, S.J. Smith, and L.M. Branscomb, Phys. Rev. **112**, 171 (1958)

[13] P.C. Cosby, R.A. Bennett, J.R. Peterson, and J.T. Moseley, J. Chem. Phys. **63**, 1612 (1975)

[14] P.C. Cosby, J.H. Ling, J.R. Peterson, and J.T. Moseley, J. Chem. Phys. **65**, 5267 (1976)

[15] M.L. Vestal, and G.H. Mauclaire, J. Chem. Phys. **67**, 8 (1977)

[16] D.J. Lavrich, M.A. Buntine, D. Serxner, and M.A. Johnson, J. Chem. Phys. **99,** 5910 (1993)

[17] R.J. Van Brunt and L.J. Kieffer, Phys. Rev. A**2**, 1899 (1970)

[18] P.D. Burrow, J. Chem. Phys. **59**, 4922 (1973)

[19] T.F. O'Malley, Phys. Rev. **155**, 59 (1973)

[20] G. Das, A.C. Wahl, W.T. Zemke, and W.C. Stwalley, J. Chem. Phys. **68**, 4252 (1978)

[21] G. Das, W.T. Zemke, and W.C. Stwalley, J. Chem. Phys. **72**, 2327 (1980)

[22] L. Dinu, A.T.J.B. Eppink, F. Rosca-Pruna, H.L. Offerhaus, W.J. van der Zande, and M.J.J. Vrakking, Rev. Sci. Instrum.**73**, 4206 (2002)

[23] D. Strasser, X. Urbain, H.B. Pedersen, N. Altstein, O. Heber, R. Wester, K.G. Bhushan, and D. Zajfman, Rev. Sci. Instrum. **71**, 3092 (2000)

[24] R. Bobbenkamp, Ph.D. Thesis, Bielefeld, 2002

[25] R.J. Saykally and K.M. Evenson, J. Chem. Phys. **71**, 1564 (1979)

[26] P.B. Davies, B.J. Handy, E.K. Murray Lloyd, and D.R. Smith, J. Chem. Phys. **68**, 1135 (1978)

[27] J.O. Hirschfelder, C.F. Curtiss, and R.B. Bird, *Molecular Theory of Gases and Liquids, (*John Wiley & Sons, Inc., 1954)

[28] G. Scoles, *Atomic and Molecular Beam Methods,* Vol. 1, (Oxford, 1988)

[29] M.C.G.N. van Vroonhoven and G.C. Groenenboom, J. Chem. Phys. **116**, 1954 (2002)

[30] M.C.G.N. van Vroonhoven and G.C. Groenenboom, J. Chem. Phys. **116**, 1965 (2002)

[31] D.J. Leahy, D.L. Osborne, D.R. Cyre, and D.M. Neumark, J. Chem. Phys. **103**, 2495 (1995)

[32] S.J. Singer, K.F. Freed, and Y.B. Band, Rev. Sci. Instrum. **79**, 6060 (1983)

[33] A.T.J.B. Eppink , and D.H. Parker, Rev. Sci. Instrum. **68**, 3477 (1997)

Summary

There are various ways of looking at molecular systems, depending on the aspects which are investigated. In this study we pay attention to the reaction of molecules with light. We look at individual molecules and characterize their behavior after the photon absorption. Even the simplest molecules turn out to be very complex systems. From the reaction of molecules with photons we learn not only the dynamics of the reaction but also the configuration of the molecule prior to photon absorption. From an energetic point of view a molecular system consists out of numerous possible configurations of energetic states. Initially the molecule "lies" in well defined and often known energetic state. The photon absorption translates into addition of energy to the molecular system. The molecules are brought into higher excited states which are often unstable. Various decay channels are possible, leading to breaking of the molecules into neutral or charged fragments. Using the latest detection techniques we record the "three-dimensional picture" of the reaction. The work presented in this thesis refers to the study of molecular systems that after photoexcitation can choose between different continua: ionization, autodetachment or dissociation. These dynamic processes imply that little structures can be found in the spectral domain. Detailed experiments on the products are required to unravel the processes.

The first part of this thesis refers to the development of the leading techniques in the field of molecular studies. **Chapter 1** is a detailed review of the two main techniques developed in the last two decades. We compare the fast beam technique with the ion imaging technique. In fast beam techniques, molecules are accelerated towards high keV energies prior to the dissociation process. In ion imaging techniques, the acceleration process is restricted to ionized fragments after the dissociation process. In the last part of this chapter, special attention is payed to the description of the apparatus used for the experiments presented in this thesis. We have improved the experimental technique necessary to obtain more insight into molecular processes, by selectively choosing the initial states, and by detecting the complete set of reaction products. The main part of the experiment comprises a fast beam apparatus, adapted for pulsed laser excitation, in combination with a three-dimensional multi-particle detector. The detection system, represents the most relevant part of the fast beam technique. The aim was to develop a time- and position-sensitive detector that allows

coincidence detection of multiple fragments with no dead time and good time- and position resolution. To achieve this, two systems have been developed. The first system uses a combination of a fast and sensitive CCD camera for position measurement and a 16-strip photomultiplier tube for the time measurement. The second detection system is a double exposure CCD camera, representing an elegant detection solution that combines in one device the time and position detection. This detector also provides an increased detection efficiency and multiparticle abilities. We present the use of a three-dimensional detection system in both fast beam and ion imaging setups.

A detailed analysis of the applicability of the double exposure CCD camera in a velocity map imaging setup is presented in **Chapter 2**. The strength of the method is illustrated in an experiment on iodine molecules I_2, that are ionized and dissociated by intense femtosecond laser pulses. Singly and doubly charged iodine fragments are detected and their (x, y) coordinates and arrival time (t) are recorded in an event counting routine. We estimate the time resolution of the system to be 1.3 ns. We show that the fragment velocity distribution derived from the (x, y, t) data is similar and in some conditions more accurate than the distribution obtained by an mathematical inversion of the (x, y) data only. This principle of detection can be used in all situations in which inversion methods are not possible, for example, when the particle distribution does not have an axis of symmetry.

The study of NO_2^- presented in **Chapter 3** is a challenge, also from an experimental point of view since this molecule is a triatomic. The analysis of the photodissociation of triatomic molecules requires a different approach than for the homonuclear diatomic molecules. The detection of charged fragments in a fast beam apparatus requires special attention. We present an experiment on the photodestruction of the NO_2^- anion at 266 nm. We quantify the competition between photodetachment and photodissociation and identify the parallel nature of the photodissociation process from the photofragment angular distribution. In the case of photodissociation events, both NO and O^- fragments are detected for each event. The detection of multiple events per laser shot is made possible by using centre-of-mass selection. The kinetic energy release spectrum is rather broad and featureless mainly due to the fact that the molecular NO fragment stores part of the kinetic energy release from the dissociation internally, as rotational and vibrational energy.

The complexity of molecular systems is nicely illustrated by the fact that even after many decades of work, many old questions have still to be answered, including those referring to the simplest molecular system, the hydrogen molecule. **In the second part** of the thesis we present new experiments on H_2 and O_2^-. **Chapter 4** refers to single-photon spectroscopy of H_2 starting from the metastable $c^3\Pi_u^-$ state to a number of triplet nd-Rydberg states ($v = 0 - 4$, $n > 12$). Using fast beam spectroscopy both the autoionization and the predissociation channels are quantified, field-free as well as with small electric fields. The results are discussed in terms of possible consequences for dissociative recombination involving low energy electron collisions with the H_2^+ molecular ion. Although surprising at first sight, a strong

analogy exists between low energy electron collision on a molecular ion that results in dissociation, a process called dissociative recombination, and the competition between autoionization and predissociation of high lying Rydberg states in molecules. The use of fast beam photofragment spectroscopy makes it possible to determine in the predissociation signal the initial ro-vibrational levels in the $c^3\Pi_u^-$ state. Coupling with the $i^3\Pi_g$ state is assumed to be responsible for field-free predissociation of the $v = 0$ Rydberg levels. The stronger observed predissociation channel of the $v = 1$ Rydberg levels is due to the non-adiabatic interaction with the $h^3\Sigma_g^+$ state in combination with l-mixing due to the external electric field. We have observed unusual behavior of the dissociation strengths for the different Rydberg states, the nature and cause of which still remains unanswered.

Unlike neutral molecules which have been studied in great detail, both theoretically and experimentally, molecular anions have not received as much attention. Photodetachment is the most studied reaction, but there are very few studies on the photodissociation of molecular ions such as O_2^- or NO_2^-. In the experiments presented in **Chapter 5**, the O_2^- molecules are subject to UV photon excitation. Photodetachment and photodissociation are the decay channels for the excited O_2^- molecules. The photodissociation fraction is $\sim 10\%$ and increases somewhat between 285 and 266 nm. High resolution photofragment spectroscopy shows that the O_2^- beam is composed of $v = 0$ ions only. The photofragment angular distribution has an anisotropy parameter $\beta = 1.9$, indicating that the process of dissociation has a parallel character, attributed to the $A\ ^2\Pi_u \longleftarrow X\ ^2\Pi_g$ transition. A detailed analysis of the kinetic energy release of the photofragments shows structure related to the distribution over the 6 fine-structure dissociation limits $O^-(^2P_{3/2,1/2}) + O(^3P_{2,1,0})$. The results are compared with an analytical diabatic dissociation model taking into account the long range charge-quadrupole interactions; the $A\ ^2\Pi_u$ state is described in a Born-Oppenheimer electrostatic approximation and projected onto the different fine-structure states at large internuclear separation using analytical expressions derived from the long range charge-quadrupole interactions between O^- and O fragments.

In conclusion we present a detection system suitable for fast beam apparatus as well as for velocity map imaging setups, capable of 3D detection of multiple particles. When using this detector in combination with a fast beam technique, fine structure resolution can be achieved. New spectroscopical data as well as new measurements (i.e. branching ratios for different decay channels, angular distributions of the fragments, KER distributions, etc.) have been performed for simple molecules as H_2, O_2^- and NO_2^-.

Samenvatting

Moleculaire systemen kunnen van veel kanten belicht worden. In het hier beschreven onderzoek analyseren we de reactie van moleculen met licht. Wij kijken daarbij naar individuele moleculen en karakteriseren hun gedrag na fotoabsorptie. Zelfs de simpelste moleculen blijken complexe systemen te zijn. Uit de reactie van moleculen met fotonen leren we niet alleen iets over de dynamica van de reactie, maar ook iets over de configuratie van het molecuul voorafgaand aan de fotoabsorptie. Een molecuul kan voorkomen in veel verschillende energietoestanden. Voor de reactie bevindt het molecuul zich in een goed gedefinieerde en vaak bekende toestand. De fotoabsorptie vertaalt zich in een toename in energie van het molecuul. De moleculen worden hierdoor in hogere toestanden gebracht, die vaak instabiel zijn. Meerdere vervalkanalen zijn mogelijk, welke tot het opbreken van de moleculen in neutrale of geladen deel-tjes leiden. Met behulp van de nieuwste detectietechnieken kunnen wij ons een direct beeld vormen van de reactie. Het in dit proefschrift gepresenteerde werk behandelt het onderzoek aan moleculaire systemen, die na fotoexcitatie tussen verschillende zogenaamde continua kunnen kiezen: ionisatie en autodetachment, waarbij een elektron het molecuul verlaat, of dissociatie, waarbij het molecuul breekt. Het voorkomen van deze continua impliceert dat er kleine structuren in het spectrale domein gevonden kunnen worden. Gedetailleerde experimenten zijn dan nodig om de processen te ontrafelen.

Het eerste gedeelte van dit proefschrift behandelt de ontwikkeling van de meest voorkomende technieken in het onderzoeksgebied van moleculaire studies. **Hoofdstuk 1** geeft een gedetailleerd overzicht van de twee voornaamste technieken, ontwikkeld in het veld van moleculaire dynamica in de twee laatste decennia. We vergelijken snelle-bundeltechnieken met ionen-afbeeldingstechnieken. In snelle-bundeltechnieken worden moleculen versneld naar hoge energie, voorafgaand aan het dissociatieproces. In ionenafbeeldingstechnieken wordt het versnellingsproces beperkt tot het versnellen van de geïoniseerde fragmenten, gevormd in het dissociatieproces. In het laatste deel van dit hoofdstuk geven we speciale aandacht aan het beschrijven van de opstelling zoals gebruikt in de gepresenteerde experimenten. Om meer details van de moleculaire processen te detecteren, hebben we de experimentele techniek verbeterd door de selectie van begintoestanden te implementeren en door alle reactieproducten

te detecteren. De opstelling is een snelle-bundelexperiment aangepast voor gepulste laserexcitatie in combinatie met een drie-dimensionaal multideeltjesdetector. Het detectiesysteem is het meest geavanceerde gedeelte in de snelle-bundeltechniek. Het doel was om een tijd- en plaatsgevoelige detector te ontwikkelen, die coïncidentiemetingen van meerdere fragmenten kan uitvoeren zonder dode tijd en met een goed oplossend vermogen voor tijd en plaats. Om dit te bereiken zijn twee systemen ontwikkeld. Het eerste systeem gebruikt een combinatie van een snelle en gevoelige CCD-camera voor positiemetingen met een 16-strip fotomultiplicatorbuis voor tijdmetingen. Het tweede detectiesysteem is een speciale CCD-camera die een elegante oplossing biedt om de tijd- en plaatsmetingen te combineren in één apparaat. Deze detector heeft ook een grote detectie-efficiëntie en mogelijkheden om meerdere deeltjes gelijktijdig te detecteren. We presenteren het gebruik van een drie-dimensionaal detectiesysteem in zowel de snelle-bundel als de ionen-afbeeldingopstelling.

Een uitgebreide analyse, onder toepassing van de speciale CCD-camera in de ionen-afbeeldingopstelling, wordt gepresenteerd in **Hoofdstuk 2**. De sterke kant van deze methode wordt geïllustreerd aan de hand van een experiment op joodmoleculen I_2, welke geïoniseerd en gedissocieerd worden door intense femtoseconde laserpulsen. Van enkelvoudig en dubbelgeladen joodfragmenten worden de plaatscoördinaten (x, y) en aankomsttijd (t) geregistreerd. We vinden dat het oplossend vermogen van het systeem rond de 1.3 ns ligt. We laten zien dat de fragmenten-snelheidsverdeling afgeleid van de (x, y, t) data, vergelijkbaar en onder sommige omstandigheden zelfs nauwkeuriger is dan de verdeling zoals verkregen door een mathematische inversie van de (x, y) data alleen. Dit detectieprincipe kan in alle situaties gebruikt worden waar inversiemethoden niet mogelijk zijn, b.v. wanneer de deeltjesverdeling geen symmetrie-as heeft.

Het onderzoek van NO_2^- gepresenteerd in **Hoofdstuk 3** is een uitdaging, uit experimenteel oogpunt, omdat het molecuul drie-atomig is. De analyse van de fotodissociatie van drie-atomige moleculen heeft een andere benadering nodig dan voor homonucleaire twee-atomige moleculen. We presenteren een experiment voor de fotodestructie van het NO_2^- anion op 266 nm. We kwantificeren de competitie tussen fotodetachment en fotodissociatie. We concluderen uit de fotofragment-hoekverdeling dat de excitatie een zogenaamde parallelle overgang is. In het geval van fotodissociatie worden alle NO en O^- fragmenten voor elke dissociatie gedetecteerd. De detectie van meerdere dissociative gebeurtenissen voor elke laserpuls wordt mogelijk gemaakt door het gebruik van zwaartepuntselectie. Het spectrum van de vrijgekomen kinetische energie is tamelijk breed en zonder karakteristieken, hoofdzakelijk doordat het moleculaire NO fragment de vrijgekomen energie over kinetisch en interne energie, i.e. rotaties en vibraties, kan verdelen.

De complexiteit van de moleculaire systemen wordt duidelijk door het feit dat zelfs na vele decennia van onderzoek, vele vragen nog steeds onbeantwoord zijn. Dit geldt ook voor het kleinste moleculaire systeem, het waterstofmolecuul H_2. **In het tweede gedeelte** van dit proefschrift presenteren we nieuwe experimenten aan H_2

and O_2^-. **Hoofdstuk 4** behandelt de fotospectroscopie van H_2, uitgaand van de metastabiele $c^3\Pi_u^-$ toestand die naar enkele triplet nd-Rydbergtoestanden ($v = 0-4$, $n > 12$) overgaat. Gebruikmakend van snelle-bundelspectroscopie kunnen zowel de autoionisatie als de predissociatiekanalen gekwantificeerd worden, zowel veld-vrij als onder invloed van kleine elektrostatische velden. De resultaten worden besproken in termen van mogelijke consequenties voor dissociatieve recombinatie waarbij laag energetische elektronen botsen met H_2^+ moleculaire ionen. Hoewel dit op eerste gezicht misschien verbazingwekkend is, bestaat er een sterke gelijkenis tussen laag energetische elektronbotsingen met moleculaire ionen die resulteren in dissociatie, een proces genaamd dissociatieve recombinatie, en de competitie tussen autoionisatie en predissociatie van hooggelegen Rydbergtoestanden in moleculen. Het gebruik van snelle-bundel fotofragmentatie-spectroscopie maakt het mogelijk om de oorspronkelijke rovibrationele niveaus van de $c^3\Pi_u^-$ toestand in het predissociatiesignaal te bepalen. Koppeling met de $i^3\Pi_g$ toestand wordt aangenomen als de verantwoordelijke voor de veld-vrije predissociatie van de $v = 0$ Rydbergtoestanden. De waarneming van een predissociatiekanaal van de $v = 1$ Rydbergtoestand alleen in aanwezigheid van een elektrisch veld komt door een niet-adiabatische interactie met de $h^3\Sigma_g^+$ toestand. Het externe elektrische veld maakt de interactie mogelijk via het proces van l-mixing. We hebben een verrassende variatie in de dissociatiesterktes van de verschillende Rydbergtoestanden waargenomen, waarvan de aard en de oorsprong nog onbekend zijn.

In tegenstelling tot neutrale moleculen die tot in groot detail onderzocht zijn, zowel theoretisch als experimenteel, hebben moleculaire anionen niet zoveel aandacht gekregen. Fotodetachment is de meest onderzochte reactie, maar er zijn weinig onderzoeken naar fotodissociatie van moleculaire ionen zoals O_2^- of NO_2^-. In de experimenten gepresenteerd in **Hoofdstuk 5** worden O_2^- moleculen blootgesteld aan ultraviolet fotoexcitatie. Fotodetachment en fotodissociatie zijn vervalkanalen voor de geëxciteerde O_2^- moleculen. De fotodissociatie fractie is $\sim 10\%$ en neemt enigszins toe tussen 285-266 nm. Hoge-resolutie fotofragmentatie-spectroscopie laat zien dat de O_2^- bundel alleen uit $v = 0$ ionen bestaat. De fotofragment-hoekverdeling heeft een anisotropieparameter $\beta = 1.9$, waaruit blijkt dat het proces van dissociatie een parallel karakter heeft, toegewezen aan de $A\ ^2\Pi_u \longleftarrow X\ ^2\Pi_g$ overgang. Een gedetailleerde analyse van de vrijgekomen kinetische energie van de fotofragmenten laat een structuur zien, die gerelateerd is aan de verdeling over de 6 fijn-structuur dissociatielimieten $O^-(^2P_{3/2,1/2}) + O(^3P_{2,1,0})$. De resultaten worden vergeleken met een analytisch diabatisch dissociatiemodel, waarin de lange-afstand lading-quadrupoolinteracties zijn meegenomen. De $A^2\Pi_u$ toestand wordt beschreven in een Born-Oppenheimer elektrostatische benadering en geprojecteerd op de verschillende fijn-structuurtoestanden op lange internucleaire afstanden, gebruikmakend van analytische uitdrukkingen afgeleid uit de lange-afstand ladings-quadrupool interacties tussen O^- en O fragmenten.

Samenvattend presenteren we een detectiesysteem, dat zowel te gebruiken is voor snelle-bundel-, als voor snelheid-afbeeldingsopstellingen, en dat drie-dimensionale detectie van multideeltjes aankan. Deze detector kan in combinatie met de snelle-

bundeltechniek de fijn-structuur oplossen. Nieuwe spectroscopische data alsmede nieuwe metingen (b.v. vertakkingsverhoudingen voor verschillende vervalkanalen, hoekverdelingen van fragmenten, vrijgekomen kinetische energieverdelingen, enz.) zijn verdregen voor simpele moleculen als H_2, O_2^- and NO_2^-.

Hartstikke bedankt !